Electrostriction in As_2Se_3-PMMA microtapers

Bhavaye Saxena

Thesis submitted to the
Faculty of Graduate and Postdoctoral Studies
in partial fulfillment of the requirements
for the Doctoral Degree in Physics

Ottawa-Carleton Intitute for Physics

Department of Physics
Faculty of Sciences
University of Ottawa

To Ludka

Abstract

Electrostriction is the tendency of materials to acquire a fluctuation in density in the presence of coherent electro-magnetic fields. It leads to a change in the refractive index of the material, which can be explained in the language of nonlinear optics as a consequence of third-order optical nonlinearities (known as Kerr nonlinearities). Such phenomenon is observed when intense beams, such as laser light, travel in a medium, e.g. an optical fiber, and the spontaneous scattering of the laser field from the thermally excited acoustic waves occurs. This effect, known as spontaneous Brillouin scattering, can become quite significant, giving rise to an interaction between the incident and backward reflected field (or the Stokes field), through the means of electrostriction. Such interaction can be classified under two categories of stimulated processes: (1) stimulated Brillouin scattering (SBS), in which two incident optical fields interact with longitudinal acoustic waves, and (2) guided acoustic wave Brillouin scattering (GAWBS), in which two incident optical fields interact with transverse acoustic waves. In case of SBS in optical fibers, the scattered light propagates backwards with a downshifted frequency of the order of GHz, while in case of GAWBS the scattered light propagates forward with multiple frequency shifts of hundred of MHz relative to the frequency of the pump laser.

Phase-matching conditions for a third-order nonlinear process, such as SBS, must be achieved in order for the interaction to build constructively. A pump optical field with central frequency ω_1 and wavenumber k_1 can produce a down-shifted Stokes optical field characterized by a central frequency ω_2 and wavenumber k_2 when scattering by an acoustic wave with frequency $\Omega = \omega_1 - \omega_2$ and wavenumber $K = k_1 - k_2$.

If acoustic waves are considered, Ω is much smaller than ω_1 and ω_2. However, the wavenumber for the acoustic wave can be classified into two separate cases. If the optical waves are counter-propagating, then the phase-matching conditions for SBS are achieved, with $k_1 \approx -k_2$, so that the wavenumber of the acoustic wave is $K \approx k_1 + k_2 \approx 2k_1$. However, if the two optical field are co-propagating, the phase-matching conditions describe GAWBS, with $k_1 \approx k_2$ and $K \approx 0$.

In this thesis, I demonstrate simultaneous generation of SBS and GAWBS from electrostriction of optical waves in a 60 cm As_2Se_3-Poly(methyl methacrylate) (or As_2Se_3-PMMA) microtaper waveguide. I show that the GAWBS in the microtaper couples with SBS through a complex energy transfer between weak Stokes and Anti-Stokes (AS) continuous waves in the presence of a high power pulsed pump wave. This results in an amplification of Stokes wave at 7.4 GHz, which is present in addition to a standard strong Stokes peak at 7.62 GHz and a secondary peak at 7.8 GHz that are contributed by SBS for a 2 μm As_2Se_3 core radius. The additional peak arises due to modulation of the optical fiber by GAWBS at 211 MHz generated by the pump. Such strong coupling of forward and backward Brillouin scattering due to large acoustic impedance between the core and cladding in such compact, highly nonlinear fibers plays a vital role in simultaneously sensing longitudinal and transverse strain within the core as well as its surroundings.

I also report high Brillouin frequency shift of 0.08 ± 0.02 MHz/Nmm^{-1} in a 60 cm As_2Se_3-PMMA hybrid microtaper with 2 μm As_2Se_3 core and 100 μm PMMA cladding diameters under transverse load. such shifts are in agreement with a numerical value of 0.06 ± 0.01 MHz/Nmm^{-1}, obtained through finite element analysis of SBS under the influence of contact stress from the loading fixture. Further numerical analysis show that uncertainties in the Brillouin frequency shift are result of birefringence that is 14 times stronger than what is found in standard silica fibers.

Lastly, I present the characterized Brillouin profile of a Dual-Core As_2Se_3-PMMA microtaper with 2μm As_2Se_3 core and 100 μm PMMA cladding diameters. I demonstrate a Brillouin peak difference of 14 MHz between an even or odd optical super-

mode, observed in a Brillouin Optical Time-Domain Analysis (BOTDA) measurement as well as with numerical simulations. This allows for definition of a novel transverse stress sensor that determines the magnitude as well as the orientation of a transverse load applied to the fiber. This system exhibits a linear relation between the net load applied to the fiber and the average Brillouin peak frequency shifts of the even and odd eigenmodes.

Acknowledgement

I would like to thank my supervisor, Professor Xiaoyi Bao for allowing me this opportunity to have my doctorate in her group. With her profound knowledge in physics, critical thinking, and her great sense of intuition, she has always been able to provide the best advice in fulfilling my goals regarding this research. Her perseverance and dedication towards this field of research is astounding, and will always be regarded as a source of inspiration. This thesis would be impossible without her constant support and guidance. I would also like to thank Professor Liang Chen, especially for his precious help and countless suggestions regarding the derivations for this thesis. His profound knowledge in physics and mathematics cannot be matched, and has always inspired me to challenge all obstacles that come in the way of my research.

I also thank Dr. Chams Baker for helping me understand the entire fabrication process for the Chalcogenide-PMMA tapers, and for providing valuable feedback on all the measurement techniques that were required to characterize these micro-tapers. I would also like to thank Dr. Song Gao, Dr. Liang Zhang and Eduard C. Dumitrescu for the tremendous assistance and guidance with my experiments and simulations.

I could not imagine what the lab would be like without all my colleagues: Prof. Mingjiang Zhang, Prof. Chunhua Wang, Dr. Yang Lu, Dr. Qian He, Dr. Dapeng Zhou, Mr. Dao Xiang, Ms. Meiqi Ren, Mr. Benoit Vanus, Mr. Zhichao Zhou and Mr. Robert Chutu Li. They have always been there for helpful discussions, and to motivate me at my worst times.

Last, but not the least, I shall sincerely thank my family and friends for all their support and encouragement. Their blessings shall never be forgotten.

Contents

Abstract iii

Acknowledgement vi

List of Figures xi

List of Tables xviii

1 Introduction 1

1.1 Stimulated Brillouin Scattering in Optical Fibers 1

1.1.1 Brillouin Scattering 1

1.1.2 Electrostriction 2

1.1.3 Stimulated Brillouin Scattering (SBS) 3

1.1.4 Guided Acoustic-Wave Brillouin Scattering (GAWBS) 5

1.2 Chalcogenide Fibers 7

1.2.1 Chalcogenide-PMMA Tapers 8

1.3 Brillouin Scattering Properties of Chalcogenide Fibers and Chalcogenide-PMMA Tapers 9

1.4 Transverse Load Sensing using Brillouin Scattering 11

1.5 Dual Core Fibers and Sensing 13

1.5.1 Sensing Applications 14

1.6 Motivation 15

1.7 Thesis Contributions 16

1.8 Thesis Outline 18

2 Model for Electrostriction **20**

2.1 Electromagnetic Field Analysis Using Vector Finite-Element Method 20

2.1.1 Variational Formulation 21

2.1.2 Domain Discretization 22

2.1.3 Basis Functions 24

2.1.4 The Ritz Formulation 25

2.2 Characteristic Equation for Step-Index Fiber Waveguides 26

2.3 Derivation of Electrostriction in

Cylindrical Waveguides 30

2.3.1 Elastodynamic Equation 30

2.3.2 Finite-Element Model for the Elastodynamic Equation 35

2.3.3 Determining Energy of Photon Wavepacket. 37

2.4 Parameters for Simulating the EM Waves and Electrostriction in custom microwires 37

2.5 Testing Finite-Element Method Simulations on SMF28 38

2.5.1 Verification of the Electromangetic Field 39

2.5.2 Results for Electrostriction Model in SMF28 40

3 Fabrication of As_2Se_3-PMMA Tapers **43**

3.1 Preparation of the Chalcogenide Fiber

and Polymer Tubes 43

3.1.1 As_2Se_3 Fiber 43

3.1.2 Polymer Tubes 44

3.2 Drawing PMMA Microtubes 44

3.3 Fusing of the PMMA onto the As_2Se_3 Fiber 46

3.4 Drawing of the Hybrid As_2Se_3-PMMA Preform 47

3.5 Polishing 48

3.6 Coupling 49

3.7 Microwire Fabrication 52

4 SBS in Single-Core As_2Se_3-PMMA Microtapers **54**

4.1 Electromangetic Field in Chalcogenide-PMMA microtapers 54

4.2 Results for SBS in Microtapers using Electrostriction Model 56

4.3 Brillouin Optical Time Domain Analysis 57

4.4 BOTDA Traces from the Pump-Stokes Configuration for Different Pump Pulse Widths 60

4.5 BOTDA Traces for Pump-Anti-Stokes Configuration 63

4.6 Experimental vs Numerical simulations for SBS in Chalcogenide-PMMA microtaper 66

5 GAWBS and SBS in As_2Se_3-PMMA Microtapers **68**

5.1 Measurements for GAWBS in Chalcogenide-PMMA microtapers . . . 69

5.2 Experimental vs numerical results for GAWBS in chalcogenide-PMMA microtapers 69

5.3 BOTDA Results for Pump-Stokes-Anti-Stokes Configuration 71

6 As_2Se_3-PMMA under Transverse Load **76**

6.1 Measurement of Transverse Stress due to Contact Stress. 77

6.2 Theory and Numerical Simulations for SBS in the Presence of Transverse Load 78

6.3 Results 81

7 Dual-Core As_2Se_3-PMMA Microtapers **86**

7.1 Fabrication and Coupling of Dual-Core Chalcogenide-PMMA Microtaper 87

7.1.1 Fusing for Dual-Core Fibers 87

7.1.2 Coupling of the SMF28 to the Chalcogenide Dual-Core Fiber . 88

7.2 Numerical Simulations for the Electromagnetic Field of a Dual Core Microtaper 89

7.3 Modelling of Electrostriction inside a Dual-Core Microtaper 90

7.4 Experimental Results for Electrostriction inside a Dual-Core Microtaper 93

7.5 Numerical Prediction for Dual-Core Chalcogenide Microtapers under the Presence of Transverse Stress 95

8 Conclusion **101**

Appendices **106**

A Python (FEniCS) Code. **106**

A.1 Mesh generation. 106

A.2 Solving Maxwell's equations on Mesh Waveguide. 108

A.3 Solving Elastodynamics equations. 111

A.4 Calculating Strain Distribution due to transverse load. 114

A.5 Assign Core and Cladding Parameters on each Subregion of Mesh. . . 116

9 References **120**

List of Figures

1.1 Schematic of the observed scattered light intensity. 2

1.2 An SBS generator. 4

1.3 An SBS amplifier. 4

1.4 Phase matching diagrams for a) Stimulated Brillouin Scattering (SBS) and b) Guided acoustic wave Brillouin Scattering (GAWBS) within an optical fiber. 6

1.5 Schematic of dual-core fiber with a step-index core-cladding configuration 13

1.6 Schematic of the power distribution in particular cores over fiber length. The longitudinal axis L is scaled to the beat length Λ to show periodicity. 14

2.1 Schematic of a single triangular element for the Finite Element Method 22

2.2 Sample of a mesh for the cross-sectional area of microtaper with a finite cladding. 23

2.3 Schematic of a step-index with an infinite cladding. 26

2.4 Spatial distribution of the (*left*) magnitude and the (*right*) z component of mode HE_{11} in standard SMF28. 39

2.5 (*left*) Numerical results for the backward scattered spectra for SMF28 as a function of detuning frequency. (*right*) Computed acoustic energy density at 10.85 GHz. 40

2.6 (*left*) Numerical results for the forward scattered spectra for SMF28 as a function of detuning frequency. The theoretical peaks for the first few $TR_{2,m}$ are indicated in blue, and the first few $RM_{0,m}$ are indicated in red. (*right*) Computed acoustic energy density at 0.082 GHz, which contains contributions from both the radially asymmetric $TR_{2,4}$ mode (resonant at 0.08165 GHz) and the symmetric mode $RM_{0,2}$ (resonant at 0.08204 GHz). 41

3.1 Schematic for drawing microtubes and microtapers. Translation stages 1 and 2 are moving at velocities v_d and v_f respectively, so that the draw ratio for the fiber sample $r_m/r_p = \sqrt{v_f/v_d + v_f}$ 45

3.2 Schematic for fusing the PMMA with the Chalcogenide fiber. 47

3.3 Schematic for polishing the hybrid fiber at arbitrary angles. 49

3.4 Cross-sectional view of the chalcogenide core (21.25 μm diameter) surrounded by PMMA cladding (1100 μm diameter) after polishing the surface. 49

3.5 Schematic for coupling a standard silica fiber with the hybrid fiber. . 50

3.6 Final configuration for an angle-coupled Single mode fiber (SMF) and Chalcogenide-PMMA hybrid fiber (angles not drawn to scale) 52

3.7 Schematic of a microtaper with a uniform waist and two similar transition regions 53

4.1 Spatial distribution of the (*left*) magnitude and the (*right*) z component of mode HE_{11} in Chalcogenide-PMMA microtaper. 55

4.2 (*left*) Numerical results of the energy spectra for a 2 micron Chalcogenide-PMMA microtaper. (*middle,right*) Energy distribution over the cross-section of the hybrid microtaper for a frequency detuning of 7.622 GHz and 7.76 GHz of the two optical fields 56

4.3 Visual representation of the BOTDA sensing mechanism. 57

4.4 BOTDA setup for hybrid fiber microtapers. EOM: Electro-Optic Modulator. HP-EDFA: High-Power Erbium-Doped-Fiber-Amplifier. FUT: Fiber Under Test. PD: Photo-Diode. OSC: OSCilloscope. 59

4.5 Sample trace for a BOTDA system. The contour represents the gain profile for the Stokes wave in dB. 60

4.6 BOTDA traces for the Stokes wave in a 60 cm hybrid microtaper with input pulsed pump with peak power of 9 dBm and pulse width of 10 ns (left), 17 ns (middle) and 20 ns (right). The contour represents the signal power $\frac{\mid A_0 + a_s(\omega, t) \mid^2}{\mid A_0 \mid^2}$ where A_0 is the continuous wave amplitude and a_s is the small varying resulting from Brillouin gain. Contour units are in dB scale. 61

4.7 Evolution of the Stokes gain profile for the hybrid microtaper as a function of peak power of a) 10 ns and b) 20 ns pulsed pump. Frequency domain traces are derived from a single time slice of the BOTDA traces where the Brillouin gain is maximum. Traces for each peak power were repeated 5 times. A_0 is the continuous wave amplitude and a_s is the small varying signal resulting from Brillouin gain. Contour units are in dB scale. 62

4.8 a) Schematic of the SBS occurring between the pump and the Stokes wave when the Stokes wave is detuned to 7.62 GHz and 7.8 GHz below pump frequency. Length of arrows represents frequency (not to scale). b) shows the transfer of power from the pump to the Stokes wave through the means of SBS for each case. Frequency is shown on horizontal axis, and length of arrows represents power. 63

4.9 Stokes gain represented as the ratio of the Stokes peak power P_{Stokes} with respect to input pump peak Power P_{pump} with pulse width of 20 ns. Traces are plotted in dB scale. 63

4.10 BOTDA traces for the Anti-Stokes wave in a hybrid microtaper with input pulsed pump with peak power of 10dBm and pulse width of 10 ns (left), 17 ns (center) and 20 ns (right). The contour represents the loss profile for the Stokes wave in dB. 64

4.11 Comparison of the spectra between the SBS process between the pump-Stokes configuration and the pump-Anti-Stokes configuration. In both cases, pump peak power was set to 13 dBm with a pulse width of 20 ns, and the Stokes, or, anti-Stokes waves were seeded with a steady power of -10 dBm 65

4.12 a) Schematic of the SBS occurring between the pump and the Stokes wave when the Anti-Stokes wave is detuned to 7.62 GHz and 7.8 GHz above pump frequency. Length of arrows represents frequency (not to scale). b) shows the transfer of power from the pump to the Stokes through the means of SBS for each case. Frequency is shown on horizontal axis, and length of arrows represents power. 66

4.13 (*left*) Overlay of the Linear Optical Power spectra from the BOTDA traces for 10 ns and 20 ns (red) pump pulse widths with the numerical results of the energy spectra for a 2 micron Chalcogenide-PMMA microtaper (black). 67

5.1 Schematic of setup for observing depolarized guided acoustic wave Brillouin scattering. PC, polarization controller; LP, linear polarizer; PD, photodetector; ESA, electrical spectrum analyzer. 69

5.2 a) Overlay between numerical acoustic kinetic energy spectra (black) and experimental optical power detected by the photodetector(red) for the GAWBS for the Chalcogenide-PMMA microtaper. b) Energy density for a transverse acoustic wave at a frequency of 211 MHz, which correponds to the peak with the highest resonance for the numerical results of the GAWBS spectra. 70

5.3 BOTDA traces for the Stokes wave in a hybrid microtaper with input pulsed pump with peak power of 10 dBm and pulse width of 10 ns (left), 17 ns (center) and 20 ns (right). The contour represents the gain profile for the Stokes wave in dB. 71

5.4 Evolution of the Stokes gain profile for the hybrid microtaper as a function of peak power of a 20 ns pulsed pump. Frequency domain traces are derived from a single time slice of the BOTDA traces where the Brillouin gain is maximum. Traces for each peak power were repeated 5 times. 72

5.5 Schematic for the nonlinear three-wave interaction between a high power pump and weak counterpropagating Stokes and Anti-Stokes. a),b) generation of sidebands detuned at $\sim \pm 200$ MHz from pump wave through GAWBS. c),d) Interaction of up-shifted GAWBS (+0.2 GHz) from the pump with Stokes(ν_s) wave detuned at 7.4 GHz through SBS with 7.62 GHz resonance (Ω_s). e),f) Interaction between the Anti-Stokes (ν_a) and the down-shifted GAWBS (-0.2 GHz) from the pump. 73

5.6 Stokes gain represented as the ratio of the Stokes peak power P_{Stokes} with respect to input pump peak Power P_{pump} with pulse width of 20 ns (bottom). Traces are plotted in dB scale. 74

6.1 a) Schematic for loading fixture to induce strain in Chalcogenide-PMMA microtapers (fiber under test - FUT) due to transverse load. b) Diagram of contact mechanics between glass slab and PMMA rod. F = load, b = contact half-width, $\sigma_c(x)$ = contact stress over the region $-b \leq x \leq b$. 77

6.2 Calculated strain distribution S_{yy} for: a) chalcogenide-PMMA microtaper with core and cladding radius of 1 μm and 100 μm respectively; b) SMF28 with core radius of core and cladding radius of 4.2 μm and 62.5 μm respectively 82

6.3 Calculated distribution of the dielectric tensor a) $\delta\epsilon_{xx}$ and a) $\delta\epsilon_{yy}$ for the chalcogenide-PMMA microtaper with core radius of 1 μm. 83

6.4 Comparison between a) numerical and b) experimental Brillouin frequency spectrum shift from 0 kg load (blue) to 4 kg load (red) at 1 kg increment. c) Numerical (red) and experimental (blue) values for Brillouin peak shift vs load. 84

7.1 Cross-sectional view of the chalcogenide dual-core (21.25 μm diameter each) surrounded by PMMA cladding (1100 μm diameter) after polishing the surface. 87

7.2 Schematic for coupling a standard silica fiber (SMF28) with the hybrid dual-core microtaper. 88

7.3 Dominant electric field amplitudes and the effective refractive indices of the four orthogonal states derived for a dual core Chalcogenide-PMMA microtaper with an individual core diameter of 2.00 μm and separation of 1.98 μm 89

7.4 Numerical results of the energy spectra for a 2 micron diameter dual-core Chalcogenide-PMMA microtaper. Large differences in n_{eff} between the supermodes result in a peak shift of 14 MHz in the Brillouin spectrum for the even mode (black) and the odd mode (red). 91

7.5 Energy distribution for the acoustic wave in the presence of an a) even and b) odd supermode. 92

7.6 BOTDA traces for the dual-core chalcogenide fiber aligned to excite electrostriction from an even (left) optical supermode and an odd (right) optical supermode. 93

7.7 Experimental results of the peak BOTDA spectrum for a 2 micron diameter dual-core Chalcogenide-PMMA microtaper. Voigt fitting over the experimental results for the even mode (red) and odd mode (blue) are conducted to demonstrate a shift of 19 $\pm$ 3 MHz between the two Brillouin peaks. 93

7.8 Distribution for a) S_{xx}, b) S_{yy}, c) S_{xy} for a transverse load of 2 kg on 66 mm sample in the x-axis; d) S_{xx}, e) S_{yy}, f) S_{xy} for a load in the y-axis; g) S_{xx}, h) S_{yy}, i) S_{xy} for a load at 45°. 96

7.9 Distribution for a) $\delta\epsilon_{xx}$, b) $\delta\epsilon_{yy}$, c) $\delta\epsilon_{xy}$ for a transverse load of 2 kg on a 66mm sample in the x-axis; d) $\delta\epsilon_{xx}$, e) $\delta\epsilon_{yy}$, f) $\delta\epsilon_{xy}$ for a load in the in the y-axis; g) $\delta\epsilon_{xx}$, h) $\delta\epsilon_{yy}$, i) $\delta\epsilon_{xy}$ for a load at 45°. 97

7.10 Evolution of the Brillouin peak shifts for even and odd modes for the dual-core microtaper in the presence of transverse load at a) x-axis and b) y-axis. c) Overlay of the numerically simulated Brillouin peak shift due to transverse load at 45° from the x-axis with the weighted average of the individual Brillouin shifts. 98

List of Tables

2.1 As_2Se_3, PMMA and SMF28 parameters used for electrostriction calculations [27, 28, 105, 106] 38

2.2 Comparison between predicted and calculated value of n_{eff} for SMF28 using known parameters for n_{core} and n_{clad} 40

4.1 Theoretical vs. numerical results for the effective refractive index within silica and Chalcogenide-PMMA tapers 55

6.1 Calculated mechanical and optical properties for As_2Se_3-PMMA microtapers [27,28] and SMF28 [106] inside the glass plate loading fixture with transverse load of 4 kg. Δn_{eff} represents the shift in refractive index due to the transverse load. 81

7.1 Calculated values for variables introduced in Eqs. 7.2 and 7.3 99

Chapter 1

Introduction

1.1 Stimulated Brillouin Scattering in Optical Fibers

1.1.1 Brillouin Scattering

When an electro-magnetic wave, or light, is launched into a material such as an optical fiber, the incident wave interacts with the molecules of the material, i.e. scattering phenomenon occurs. This results in a scattering spectrum. Depending on the intensity of the incident light, spontaneous or stimulated scattering is observed for low or high intensities of incident light respectively. Figure 1.1 shows a typical spectrum of spontaneous scattering from solid state matter. In most cases, Rayleigh scattering is the most common optical phenomenon, named after the British physicist Lord Rayleigh. It is an elastic scattering of light at scattering centers which are much smaller than the wavelength of the light. Under such circumstances the scattering power is proportional to the fourth power of the inverse wavelength [1, 2]. Forward and backward scattering are equally strong. In case of an inelastic scattering, the light with lower frequency than the incident light is called the Stokes branch, while the light with higher frequency than the incident light is called the Anti-Stokes branch. These frequency shifts occur when incident light scatters off the acoustic waves that are present in thermal equilibrium. Due to the Doppler effect, the frequency of the scattered light is downshifted from the incident light when it interacts with acoustic

wave traveling in the same direction as the incident field. Similarly, the frequency of the scattered light is up-shifted from the incident light when it interacts with acoustic wave traveling opposite to the incident field. **Because of this difference in frequencies, the incident and scattered waves beat together, causing variations of the density of the media, which in turn causes refractive index variations.** In optical fibers, the incident light scatters off the refractive index variations in the direction opposite to the direction of propagation of the incident light, thus giving rise to the Brillouin scattering phenomenon [1, 2].

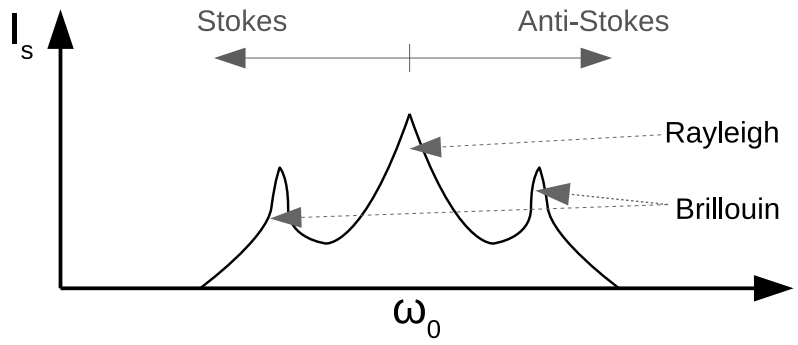

Figure 1.1: Schematic of the observed scattered light intensity.

1.1.2 Electrostriction

Electrostriction describes materials' reaction to the presence of coherent electromagnetic fields, manifested in density flucutation [2]. This leads to fluctuations of the refractive index, which, in the formalism of nonlinear optics, can be attributed to third-order optical nonlinearities (known as Kerr nonlinearities). The forces generated through electrostriction produce material contractions (or expansions) which are quadratic with respect to the electromagnetic field, and result primarily from the strain dependence of the dielectric constant. Electrostriction, distinct from piezoelectricity (accumulation of electric charge in response to applied mechanical stress), occurs independently of material symmetry, and increases with the fourth power of material refractive index. [3, 4].

More specifically, electrostriction is expressed as a material stress σ_{ij}^{es}, or equiva-

lently, as a Maxwell stress tensor $T_{ij}^{es} = -\sigma_{ij}^{es}$ that depends on the permittivity of the material ϵ_{ij}, the electromagnetic field E_i as follows [3, 4]:

$$\langle \sigma_{ij} \rangle = -\frac{1}{2}\epsilon_0 [\epsilon_{ik} p_{klmn} \epsilon_{lj}] \langle E_m E_n \rangle, \tag{1.1}$$

where p_{ijkl} is known as the photoelastic tensor (or elasto-optic tensor). In the case of amorphous solid (isotropic media), this simplifies to:

$$\langle \sigma_{ij} \rangle = -\frac{1}{2}\epsilon_0 n^4 p_{ijkl} \langle E_k E_l \rangle, \tag{1.2}$$

giving rise to the fourth power dependence of material refractive index n. $\langle E_k E_l \rangle$ represents the time-averaged field product over an optical cycle, as materials generally do not respond mechanically at a time scale of the optical frequency. Thus the stress also is expressed as a time-averaged value. From the expression in Eq. 1.2, the force exerted onto the medium through electrostriction, or electrostrictive forces, can be expressed as the divergence of the electrostrictive stress tensor distribution around the material. It is this divergent term that contributes to the density fluctuations inside the material, giving rise to what is known as stimulated Brillouin scattering [2, 4].

1.1.3 Stimulated Brillouin Scattering (SBS)

When intense beams, such as laser light, travel in an optical fiber, the laser field scatters from the thermally excited acoustic waves. This effect is known as spontaneous Brillouin scattering and it results in electrostrictive interaction between the incident and backward reflected field (or the Stokes field). Electrostriction creates a dynamic acoustic grating, which in turn causes variations in the refractive index of the material. This results in what is known as stimulated Brillouin scattering due to the variations in the medium. SBS is frequently encountered when narrow-band optical signals are amplified in a fiber amplifier. In fact, SBS effectively introduces a power limit, commonly referred to as the Brillouin threshold, for the propagation of narrow-band optical signals [5, 6].

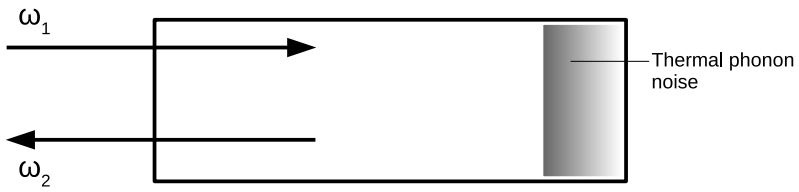

Figure 1.2: An SBS generator.

There exist two conceptually different configurations in which SBS can be studied [2]. Figure 1.2 shows the configuration of the SBS generator, in which only the laser beam is applied externally, while both the Stokes wave, and the acoustic wave are created initially from the noise within the region of interaction, but it also gains the contribution fro electrostriction between the incident and scattered optical fields. Figure 1.3 shows the configuration for an SBS amplifier, in which both the laser and Stokes fields are applied externally. In this configuration, the pump and Stokes fields are counter-propagating, and a strong interaction takes place when the frequency and the wavevector of the injected Stokes wave is equal to that created by the SBS generator (shwon in Fig. 1.2). In our case, the SBS amplifier configuration will be considered.

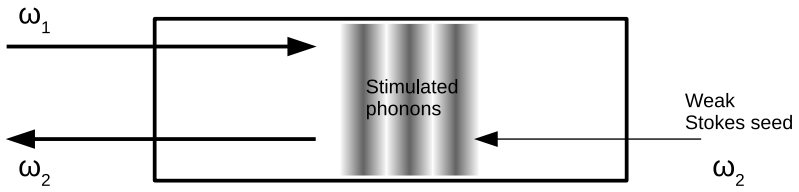

Figure 1.3: An SBS amplifier.

SBS in optical fibers can also be exploited for a wide variety of device and systems applications. For example, narrow Brillouin gain spectra in fibers make SBS ideal for wavelength conversion, frequency selectivity, carrier suppression, and amplification. The influence of temperature and strain on the peak gain value and Brillouin frequency shift have been recognized as ideal traits for distributed fiber sensors using Brillouin optical time domain analysis (BOTDA) [7], Brillouin optical

time domain reflectometry (BOTDR) and Brillouin optical correlation domain analysis (BOCDA) [8, 9]. Microwave photonic systems have been developed to utilize the narrow Brillouin gain bandwidth in order to selectively amplify a weak data carrying optical sideband without perturbing an unmodulated carrier [10]. Sufficient, narrow linewidth, low frequency jitter Brillouin fiber lasers have also been developed for applications such as atomic spectroscopy and laser interferometry at the highest levels of precision possible [11, 12]. Lastly, with the combination of the Kerr nonlinearity, SBS also plays a major role at the generation of slow light, hence becoming a strong candidate for controllable optical delay lines, optical buffers and true time delay methods [6].

1.1.4 Guided Acoustic-Wave Brillouin Scattering (GAWBS)

Guided acoustic wave Brillouin Scattering (GAWBS) [13], is another process involving Brillouin scattering in which incident light interacts with transverse acoustic waves. For SBS in optical fibers, the scattered light propagates backward with a downshifted frequency of the order of gigahertz, as the shift frequency $\nu_B = 2nV_a/\lambda$ depends primarily on the intrinsic property of the material, such as the refractive index n and acoustic velocity V_a [2]. On the other hand, in GAWBS, the scattered light propagates forward with multiple frequency shifts of hundreds of megahertz relative to the pump laser. GAWBS depends primarily on several transverse structural parameters of the optical fiber, such as the fiber outer diameter, core diameter, the transverse refractive index and acoustic impedance profile [14]. Because both SBS and GAWBS are third-order nonlinear parametric processes involving two optical fields and one acoustic field, the phase-matching conditions must be achieved in order for the interaction to build constructively, as shown in Fig. 1.4. A pump optical field with central frequency ω_1 and wavenumber k_1 can produce a down-shifted Stokes optical field characterized by a central frequency ω_2 and wavenumber k_2 when scattering by an acoustic wave with frequency $\Omega = \omega_1 - \omega_2$ and wavenumber $K = k_1 - k_2$. Since we are considering acoustic waves, Ω is much smaller than ω_1 and ω_2. The wavenumber for the acoustic wave can

though be classified in two distinct cases, as shown in Fig. 1.4. If the optical waves are counter-propagating, then the phase-matching conditions for SBS are achieved, with $k_1 \approx -k_2$, so that the wavenumber of the acoustic wave is $K \approx k_1 + k_2 \approx 2k_1$. However, if the two optical field are co-propagating, the phase-matching conditions describe GAWBS, with $k_1 \approx k_2$ and $K \approx 0$.

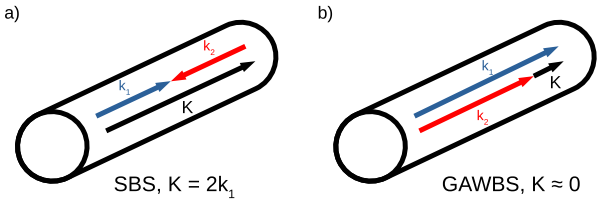

Figure 1.4: Phase matching diagrams for a) Stimulated Brillouin Scattering (SBS) and b) Guided acoustic wave Brillouin Scattering (GAWBS) within an optical fiber.

GAWBS can be categorized into two types based on the acoustic modes in fibers: (1) polarized GAWBS [13] caused by the radially symmetric modes that perturb the refractive index of the fiber cross-section, (2) depolarized GAWBS caused by the torsional-radial modes that perturb not only the refractive index but also the birefringence of the fiber. Such depolarized modes describe the refractive index dependence on both the polarization and propagation direction of light [13, 15–18], and therefore play a major role in sensing application which have been investigated extensively [15, 19–25]. For example, fiber sensors for the impedance sensing of an unknown liquid based on forward stimulated Brillouin scattering were shown [21]. The measurement of the acoustic impedance of external materials based on spectrum dependence of depolarized GAWBS modes was then proposed [15]. The analysis of the spectra of depolarized GAWBS modes allows also for characterisation of absolute diameter and non-uniformity of micrometer-scale fiber tapers [22]. Such systems enable us to exploit the transverse nature of acoustic vibrations for measurement of mechanical impedance or chemicals surrounding the optical fiber, which were previously conducted using fibers with non-standard geometries or reactive media [23].

1.2 Chalcogenide Fibers

Although silica fibers have been the ideal choice for most of the optical processing and sensing applications using SBS, much of the attention has now been diverted towards chalcogenide fibers: a new breed of fibers that possess much stronger nonlinearities that could potentially replace silica fibers in the 1550 nm range [26–33]. Chalcogenides are a group of inorganic materials which contain a combination of the chalcogen elements such as S, Se, or Te in conjunction with an electro-positive element, out of which As and Ge are the most common [34–37]. Although they are generally less robust than their silica or silicon based counterparts [29, 30], these glasses have been known to acquire a broad range of transparency in the infrared region, with low optical attenuation, large refractive indices, and can exhibit high nonlinear Kerr effect, enhanced Stimulated Raman [38] and Stimulated Brillouin effects [27–29]. Because of this, they have been used extensively in the field of fiber optics for several applications such as supercontinuum generation [26], ultrafast all-optical switches [34], mid-IR sources [33], strong Stimulated Brillouin Scattering [39] and slow and fast light in dielectric materials [40].

In particular, As_2Se_3 is the most widely discussed chalcogenide fiber material because of its high nonlinearity coefficients at 1550 nm [35, 41]. Despite its high refractive index of 2.81 [39], the single mode As_2Se_3 fiber operating at 1550 nm are well known to exhibit a Kerr nonlinearity index n_2 of 2.4 $\times 10^{-17}$ m^2 W^{-1} [30,31,42] and a Brillouin gain g_B of 6.08 $\times 10^{-9}$ m W^{-1} [27,39]. This makes it an excellent substitute for silica fiber in the same wavelength regime which only exhibits an n_2 of 2.5 $\times 10^{-20}$ m^2 W^{-1} and a Brillouin gain g_B of 2.71 $\times 10^{-11}$ m W^{-1} [27], which is desirable because higher gain coefficients eventually allow for fabrication of devices with shorter fiber length. In addition to this, the As_2Se_3 also has a low softening temperature of 180°C [42], allowing one to fabricate custom waveguides with tunable characteristics to either enhance or reduce the presence of several nonlinear phenomena as per the application. In my case, the characteristics of the As_2Se_3 fibers are used to create custom chalcogenide microtapers with a coating of Poly(methyl methacrylate) (PMMA).

This coating adds strength to the otherwise fragile microtapers and prevents optical interaction with the environment. In terms of outdoor applications, PMMA is the most sought after material when compared to other plastics such as polystyrene and polyethylene due to its flexibility with higher fracture point at 0.05ϵ strain [43, 44]. Moreover, PMMA has a high transmission spectrum ranging from visible region to 2800 nm, with a refractive index of 1.481 near 1550 nm [45], also making it optically compatible to the chalcogenide core when used as a cladding for a step-index optical fiber.

1.2.1 Chalcogenide-PMMA Tapers

As_2Se_3 tapers were originally fabricated due to their capacity to improve the waveguide nonlinearity parameter $\gamma = k_0 n_2 / A_{eff}$ by reducing the effective area A_{eff} of the chalcogenide fiber [30,31,46,47], as well as shift the zero-dispersion wavelength range close to 2 μm instead of 5 μm [46,47]. This enabled the generation of super-continuum in the mid-IR by creating sub-micron As_2Se_3 tapers using the heat brushing technique [31, 32, 46, 48], or through the novel coextrusion methodology that reduced the core diameter to 480 nm [49]. Although these microtapers can provide a waveguide nonlinearity of $\gamma = 68$ W^{-1} m^{-1}, which is one of the highest demonstrated in the mid-IR range [46], its practical use is questionable due its mechanical fragility, surface damage and contamination and sensitivity to the enviroment due to the fundamental mode protruding outside of the microwire [30].

Baker et al. successfully fabricated the first hybrid chalcogenide-PMMA taper consisting of a As_2Se_3 or As_2S_3 core and a PolyMethyl MethAcrylate (PMMA) cladding, which enhances the mechanical strength of the chalcogenide tapers and protects it from environmental contamination and degradation [30]. The As_2Se_3 core provided a nonlinearity of up to $\gamma = 133$ W^{-1} m^{-1} and the PMMA cladding provided mechanical strength of the device, reduced the sensitivity and contamination from the surroundings, as well as confined the optical field within the As_2Se_3 due to the large refractive index difference between the two materials. Fabrication of such a taper led to the

realization of a parametric oscillator [50], Fabry-Perot Raman laser [51], broadband four-wave mixing [52], inscription of fiber Bragg gratings utilizing photosensitivity of As_2Se_3 glass to optical signals at 1550 nm [53], supercontinuum generation spans from 960 nm to 2500 nm [54] and normal dispersion modulation instability in the mid-infrared (mid-IR) spectral region [55].

The main competing technologies include air-cladding As_2Se_3 microwires, other hybrid microwires having an As_2Se_3 core with a tellurite or silica cladding [56,57], and fibers with advanced geometrical cross-section such as suspended-core and photonic crystal fibers [58, 59]. Tellurite-coated tapers, similar to the PMMA coated tapers, can be fabricated using a heat-and-draw process as they both have similar softening temperatures [56]. However they are less porous than the PMMA, which could absorb chemicals for sensing applications [60–62]. Silica based cladding microtapers are known to be troublesome simply because the softening temperature of the two materials differ by almost 1000° C [42], and require silica hollow cores that are then filled with molten chalcogenides [57]. Lastly, suspended-core and photonic crystal fibers have the disadvantage of requiring dispersion engineering, which require a precise control of the air-hole diameter and the hole spacing [63, 64].

1.3 Brillouin Scattering Properties of Chalcogenide Fibers and Chalcogenide-PMMA Tapers

Although primarily known for their significantly high Kerr nonlinearities, chalcogenide glasses have also been shown to exhibit a large Brillouin gain coefficient near the 1550 nm transmission range. Ogusu et al. [65] estimated the Brillouin gain coefficient g_B in bulk As_2Se_3 glass to be 53.2 $\times 10^{-11}$ m/W by measuring the phonon lifetime which was 4.57 ns, and reported that g_B for As_2Se_3 was 25 times larger than that of bulk fused silica ($g_B = 2.24 \times 10^{-11}$ m/W). The gain coefficient was later characterized in a single mode As_2Se_3 fiber by Abedin et al. [39] for a 5 m long, 6 μm core diameter of the fiber with a V parameter of 2.2, and was determined to be 6.0×10^{-9} m/W

which is about 134 times that of fused silica fiber. The threshold for SBS in the 5 m long fiber was as small as 85 mW.

This eventually was followed by the demonstration of several As_2Se_3 Brillouin fiber lasers with low threshold and narrow linewidths built only using several meter long chalcogenide samples. Using the same single core fiber in [39], Abedin et al. were able to generate the first chalcogenide Brillouin fiber laser using a 4.9 m sample with a threshold power of 35 mW [66], followed by a single-frequency Brillouin laser using a 2 m Chalcogenide Fabry-Perot cavity with a 56 mW threshold [67]. The coupling loss between the lensed silica fiber and the chalcogenide core was estimated to be at 3.3 dB and the total round trip loss for the Stokes wave inside the Fabry-Pérot cavity was 5.6 dB. There were also implementations of Brillouin fiber lasers using a 2 micron 1.5 m long suspended core fiber with a 52 mW lasing threshold [68] and also a 3 m micro-structured fiber with a record low threshold of 6 mW [69]. Lastly, an implementation of a Brillouin laser has also been shown using a 7 cm chalcogenide rib-waveguide embedded on a photonic chip with a lasing threshold on 360 mW and slope efficiency of 30% [70]. This photonic chip waveguide was further used to demonstrate a tunable photonic notch filter [71], as well as demonstrate slow light [72].

Although the chalcogenide-PMMA tapers were initially targeted at enhancing the Kerr nonlinearity within the chalcogenide fiber [30], interaction of the chalcogenide core with the PMMA cladding additionally demonstrated quite interesting Brillouin scattering features [27, 28]. In favour of enhancing Kerr nonlinearity, Beugnot et al. [27] have demonstrated that the PMMA cladding surrounding microwire reduces stimulated Brillouin scattering by broadening the Brillouin linewidth and increases the power threshold. Compared to the 16 MHz linewidth measured by [39] for a pure chalcogenide fiber of 6 μm core radius, the PMMA cladding surrounding a chalcogenide microwire of 0.7 μm increased the linewidth to 110 MHz [27], primarily due to the intrinsic linewidth of 120 MHz contributed from the PMMA [73] and with insignificant broadening due to tapering non-uniformity or short tapered sections. Moreover, the Brillouin peak frequency shift increased with respect to the core di-

ameter, as the frequency shift is linearly proportional to the effective refractive index of the hybrid microtaper [27]. As the taper diameter increased, the frequency shift eventually converged to the original frequency shift of 7.95 GHz that is defined in a standard chalcogenide fiber [27, 39]. This means that the SBS frequency shift can be widely tuned and finely controlled over a few GHz frequency range by the diameter of the microwire. This large tunability is considered useful for applications such as microwave photonics [28].

The Brillouin scattering spectra of hybrid microtapers measured by Beugnot et al. [27] have also been compared with numerical simulations based on a more generalized approach for deriving the SBS of an arbitrary waveguide by directly solving the elasto-dynamic equations subject to an electrostriction stress distribution [27, 28, 74]. Although it was claimed to provide a good estimate of the theoretical Brillouin spectrum by measuring the elastic energy of the acoustic wave generated by the light, the comparisons between the theoretical results and the experimental results cannot be considered correct, simply because the experimental results relied on purely SBS generated by a single pump driven under the influence of the thermal noise in the fiber. These results were not obtained using two coherent frequency-detuned optical fields as was assumed by the theoretical modes. Because of this, there are some noticeable discrepancies between the resonant peaks in the simulation and the experimental results. A significant part of the thesis will therefore be comparing the solutions for the elastodynamic equations with the experimental results for a coherent two-wave SBS process.

1.4 Transverse Load Sensing using Brillouin Scattering

Transverse load sensors have sparked significant interest in the recent years due to their application in structure health monitoring and civil engineering [75–86]. Most sensors were built as point sensors that primarily used fiber Bragg gratings or Sagnac

fiber loops in order to enhance the sensitivity of the fiber at the point of interest. These gratings were usually inscribed on high-birefringence (Hi-Bi) materials in order to achieve large frequency separations in the fast and slow axis in the presence of stress [79–82]. Sagnac fiber loops using Hi-Bi fiber segments as the point source were also implemented for high sensitivity by measuring the intereference pattern of the transmitted field [83–85]. Moreover, custom fibers such as photonic crystal fibers [81, 83–85], and multi-core fibers [82] have also been designed the enhance the measurement sensitivity. However, neither of these systems with Bragg gratings or Sagnac loops can be realized as a distributed measurement system. It was only in 2010 that the first distributed transverse load sensor was proposed using optical frequency-domain reflectometry (OFDR) [86]. This technique was based on measuring the different Rayleigh scattering profiles along the fast and slow axis of a polarization maintained fiber. This was achieved by cross-correlating the Rayleigh scattering of each axis with its previous recorded "footprint", giving a spatial resolution of 2 cm with a sensitivity of 73 $\mu\epsilon/\text{Nmm}^{-1}$ [86].

However, due to the extremely small shift in intrinsic Brillouin spectrum for standard single mode silica fibers in the presence of transverse load (in the order of 0.005 MHz/N as calculated in this thesis) [75, 87], transverse load sensors cannot be realized with conventional Brillouin optical time-domain analysis (BOTDA) [75]. Such sensors have still not been proposed, even though these distributive sensor techniques have been developed for two decades and are widely used for temperature and longitudinal strain measurements [7]. Instead, sensing of distributed transverse load over long fibers is achieved using distributed Bragg gratings (DBG), which are spatially localized gratings created using SBS [88]. DBGs were primarily used as point source sensors [88, 89] and for distributed temperature sensor using polarization maintaining fibers [90] and photonic crystal fibers [91] due to their high sensitivity to the fluctuations in the birefringence of birefringent fiber [75, 88]. Distributed transverse load sensing using DBGs was eventually demonstrated in 2015 by [75] in highly birefringent silica-based elliptical core fibers, although the optimal transverse load sensor

design still remains an open problem. Therefore this thesis focuses on transverse load sensing applications and proposes a technique based on BOTDA for the first time.

1.5 Dual Core Fibers and Sensing

Dual core fibers are attractive fiber optic components for sensing and processing applications. Their structure usually involves embedding two cores of a higher refractive index within a cladding of a lower refractive index, essentially breaking infinite rotational symmetry that is achieved by single-core fibers. Depending on the application, the two cores can be separated widely apart, or can be merged to form a hybrid core structure depending on how much cross-talk is required between the two cores.

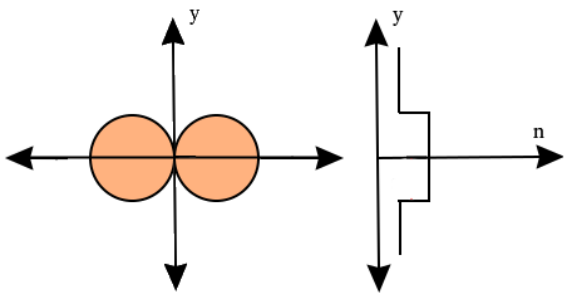

Figure 1.5: Schematic of dual-core fiber with a step-index core-cladding configuration

Crosstalk between the cores of a multicore fiber is analyzed using what is known as the supermode theory [92]. In this theory, the composite waveguide made of multiple cores is treated as a whole, hence allowing us to represent an actual field distribution in the fiber as a superposition of the orthogonal states of the light field. For the case of a dual-core fiber, Maxwell's equations result in two sets of symmetric (even) modes and antisymmetric (odd) modes for the x and y polarization orientations, respectively. Hence, we can represent any guided electric field as a superposition of these four orthogonal supermodes, where two of the four can represent any electric field for a single polarization. In this thesis, we denote the electric fields E_x^e, E_x^o, E_y^e and E_y^o as the even (e) or odd (o) mode for polarization x or y.

An optical field that is inserted through only one the cores is represented as a

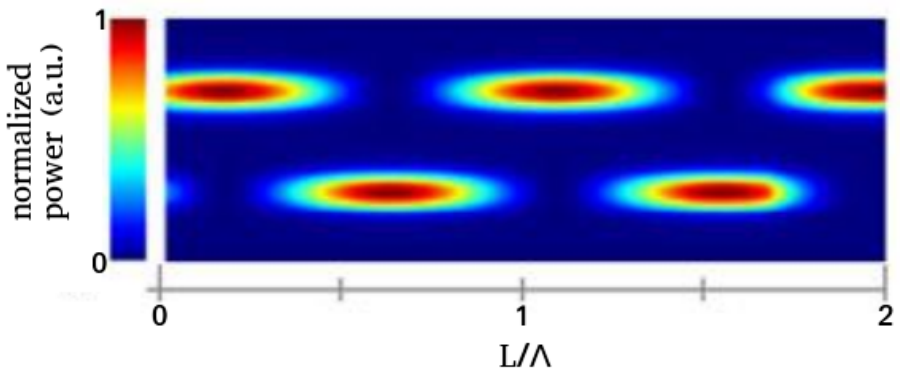

Figure 1.6: Schematic of the power distribution in particular cores over fiber length. The longitudinal axis L is scaled to the beat length Λ to show periodicity.

superposition of an even and odd mode. Although initially in phase, the relative difference in the effective refractive index between the even and odd modes for the dual-core fiber results in a mismatch of the phase velocities, inducing spatially varying intensity profiles along the z-axis as shown in Figure 1.6. The intensity profiles vary sinusoidally with a period of $\Lambda = \lambda / \mid n^e_{eff} - n^o_{eff} \mid$, and are off by a phase of $\pi/2$ in each arm, essentially representing an intensity profile that couples between the two cores.

1.5.1 Sensing Applications

At present, analysis of two-core or multicore fibers designed for distributed sensing using Brillouin scattering usually do not introduce heavy cross-talk between the two cores, but rather treat the cores separately. For example, several works done on two-core fibers [93, 94] allow for simultaneous measurements of strain and temperature by embedding two or more different core profiles such that each dominant Brillouin peak is off by an order of 10 MHz and fluctuations from each core can be detected individually and be characterized due to minimal overlap of acoustic and optical modes. As such, dual-core fibers can be treated as individual single-mode fibers that are embedded onto the same cladding, and do not need to be represented using supermode theory [92]. Similar effect is achieved by Mothe *et. al.* [92] who considered fiber designs with very large coupling lengths (in the order of few kilometers) using

dual-core micro-structure fibers with supermodes.

Recently however, several works by Gao et. al. [95–97] show that dual-core As_2Se_3-PMMA microtapers with large cross-talk between the cores have exceptional ability to measure longitudinal strain and temperature with high sensitivities of ~ 100 pm/$^\circ C$ and ~ 10 pm/$\mu\epsilon$. This is achieved by controlling the radius of the As_2Se_3 core such that the net effective refractive indices of the two supermodes are almost negligible, giving rise to high fluctuations in the transmission in the presence of strain or temperature. Temperature insensitivity in the range of $30^\circ C$ to $40^\circ C$ was also achieved by setting the As_2Se_3 core diameter to 0.61 μm. However, neither of these devices were evaluated using a standard BOTDA system for distributed measurments, therefore they acted as point sensors. Moreover, neither of the systems was tested under the presence of transverse load.

1.6 Motivation

My motivation to characterize the nonlinear processes in tapered As_2Se_3-PMMA single and dual-core fibers is to investigate sensing and optical signal processing applications in the near-IR and Mid-IR using a combination of high intrinsic material nonlinearity, flexibility in microwire designs and strain induced perturbations of optical properties. The hybrid nature of the microtaper enables a combination of SBS and GAWBS processes that can be enhanced for sensing applications or reduced [27] in order to design compact optical parametric oscillators for optical signal processing operations.

Simulations for these materials help to understand the physical processes observed in experiment and allow me to make better designs by predicting enhancement or reduction of these processes using various control factors. These can be, for example, the core and cladding diameters, or the number of chalcogenide cores embedded in the waveguide. This results in better interaction of the optical and acoustic waves which could lead to design of Brillouin lasers with tailored optical filters. It could also allow for fabrication of high nonlinear devices for optical signal processing at

mid-IR wavelengths at compact sizes, surpassing the capabilities that are achievable by standard silica fibers. Simulation of these nonlinear processes with the inclusion of dielectric changes due to mechanical stress open up more possibilities for important applications. Few of these include compact devices for highly sensitive point sensors in structural health monitoring, as well as ultrasound generators and detectors with polarization maintaining capabilities, which use the birefringence properties of these materials under stress.

1.7 Thesis Contributions

This thesis includes studies of SBS and GAWBS from electrostriction of optical waves As_2Se_3-PMMA microtaper waveguides. In order to optimize these fibers for sensing and signal processing applications a thorough experimental and theoretical analysis of the SBS profile is needed. Therefore, I develop the theoretical methods to study the physics that governs the Brillouin processes within them. I also investigate experimentally the SBS properties of As_2Se_3-PMMA microtaper waveguides subjected to increasing load, which together with the theoretical techniques allows me to build a in-depth understanding of the strain mechanisms in them. These studies give a realistic picture of the fibers' properties and show that they are good candidates for sensing applications.

First, I demonstrate simultaneous generation of SBS and GAWBS from electrostriction of optical waves in a 60 cm As_2Se_3-PMMA microtaper waveguide [30]. It was achieved by conducting Brillouin Optical Time-Domain Analysis (BOTDA) [8] on these microtapers by simultaneously pumping weak Stokes and Anti-Stokes (AS) continuous waves in the presence of a high power pulsed pump wave in counter-propagating directions. Contrary to the well understood mechanism of individual AS-pump and Stokes-pump configurations in the BOTDA, this three-wave interaction is explained here for the first time. It allows the system to conduct a complex energy transfer between the Stokes wave, AS waves and the transverse acoustic waves responsible for GAWBS generated by the pump. It manifests itself as a distinct Bril-

louin gain peak for the Stokes wave at 7.4 GHz, in addition to the conventional 7.6 GHz and 7.8 GHz. The distortion of the SBS spectrum can be explained as coupling of the longitudinal mode to transverse waves near the 200 MHz range, which arises due to differences in the acoustic impedance between the core and the cladding. This is the first report of such phenomenon in hybrid microtaper waveguides.

Second, I provide a thorough analysis of the high Brillouin frequency shifts in a 60 cm As_2Se_3-PMMA hybrid microtaper with 2 μm As_2Se_3 core and 100 μm PMMA cladding diameters under transverse load, which has not been studied before. The finite element analysis of stimulated Brillouin scattering (SBS) under the influence of contact stress from the loading fixture shows that strain induced at the elastic PMMA edge is still traceable towards the chalcogenide core. This chalcogenide core serves as further enhancement of the dielectric tensor fluctuations arising from this strain due to its high refractive index properties. As a result, the SBS profile gains traceable frequency shifts, which offers promising application prospects. There is an excellent agreement between the experimental values and theoretical predictions of the magnitude of these shifts. I also demonstrate high birefringence exhibited by these tapers in the presence of load, manifesting itself as a large difference in propagation constant for each polarization, which affects the uncertainty of the frequency shifts.

Last, I extended the understanding of the Brillouin profile for the single-core As_2Se_3-PMMA microtapers and its high birefringent properties under waveguide asymmetries by characterizing the Brillouin profile of a Dual-Core Chalcogenide-PMMA microtaper for the first time. The results of a BOTDA measurement supported with numerical simulations demonstrate a Brillouin peak difference of 14 MHz between an even or odd optical mode. Based on this, I demonstrate numerically a novel transverse stress sensor that determines the magnitude as well as the orientation of a transverse load applied to the fiber. Such a system is able to exhibit a linear relation between the net load applied to the fiber and the average Brillouin peak frequency shifts of the even and odd eigenmodes. Moreover, strong Brillouin shifts for the eigenmodes, especially due to the stress in the x-axis of the fiber, play a vital role

in designing novel sensor setups. It allow for retrieving complex characteristics within the fiber under transverse load using simple BOTDA measurements of the individual eigenmodes of the waveguide. This is the first report on such application prospects for Dual-Core Chalcogenide-PMMA microtapers.

1.8 Thesis Outline

Chapter 2 presents a detailed description of the numerical simulations that are necessary to describe the electrostriction in a optical fiber. This is achieved by first calculating the optical modes of the microwire, followed by the calculation of the displacement in the microwire due to electrostriction with the inclusion of both longitudinal and shear waves. The numerical model is then tested to represent SBS as well as GAWBS within SMF28 so that the results, and hence, the numerical code, is in agreement with the existing literature on SMF28.

Chapter 3 gives the detailed description of the fabricating process for these hybrid microtapers. This chapter describes how one should prepare the chalcogenide fiber and polymer tubes, fusing the polymer tubes over the chalcogenide fiber, draw the hybrid PMMA into a preform, polish and couple the ends of the preform with the SMF28 and UV epoxy curing, and finally taper the preform down to the desired diameter for testing.

Chapter 4 discusses the SBS occurring inside a single-core hybrid microtaper. A thorough experimental and theoretical analysis of the SBS profile is conducted in order to validate our experimentation technique with the numerical simulations before we expand on our model by including transverse stress. Experimental results for the Pump-Stokes and Pump-Antistokes configuration in the BOTDA were also conducted to build the basic understanding of these processes, prior to exploring the novel physical phenomena in the next chapter.

Chapter 5 demonstrates the simultaneous generation of SBS and GAWBS from electrostriction of optical waves in a 60 cm As_2Se_3-PMMA microtaper waveguide [30]. BOTDA [8] on these microtapers was conducted by simultaneously pumping weak

Stokes and Anti-Stokes continuous waves in the presence of a high power pulsed pump wave in counter-propagating directions. Detailed explanation of these process is provided and their relation to the BOTDA traces of the Pump-Stokes and Pump-Antistokes configuration (chapter 4) is demontrated.

Chapter 6 includes a thorough analysis of the high Brillouin frequency shifts in a 60 cm As_2Se_3-PMMA hybrid microtaper with 2 μm As_2Se_3 core and 100 μm PMMA cladding diameters under transverse load. The finite element study of SBS under the influence of contact stress from the loading fixture shows that the SBS profile gains traceable frequency shifts, and there is an excellent agreement between the experimental values and theorical predictions of the magnitude of these shifts.

Chapter 7 includes a detailed numerical and experimental study of the eigenmodes of a dual-core As_2Se_3-PMMA microtaper and its electrostrictive properties when subjected to a BOTDA setup. The chapter then discusses possible applications of transverse load sensing by demonstrating high Brillouin peak frequency shifts for the individual eigenmodes of the microtaper that vary linearly with respect to the transverse load applied to it.

Chapter 2

Model for Electrostriction in Optical Microwires

In this chapter, we present the methods used in analyzing the electrostriction in optical microwires. The aspects that are of interest in this analysis include the calculation of the microwire optical modes, and the simulation of the displacement in microwires due to electrostriction with the inclusion of both longitudinal and shear waves. Such a technique plays a strong role in predicting the spectra of the acoustic wave energy as a function of the detuned frequency between two optical modes that are either co-propagating or counter-propagating. Furthermore, such a technique allows us to retrieve an explicit energy density profile of the acoustic wave throughout the cross section of the profile, allowing us to get more insight in estimating the energy transfer between the two optical fields and the acoustic wave.

2.1 Electromagnetic Field Analysis Using Vector Finite-Element Method

As discussed by [98], full vector field analysis is required in complex fiber waveguides with composite structures and sub-wavelength dimensions due to inaccuracies in scalar field approximation such as the finite-difference method [99], the boundary-

integral method [100], and the finite-element method [101–103]. In our case, a tangential finite-element method, based on edge elements, has been used to eliminate spurious solutions that result from standard vector finite-element methods [103]. This method comprises of a combination of scalar basis function for the longitudinal z-component and vector basis functions that represent the tangential component of the field.

2.1.1 Variational Formulation

The boundary value problem for a waveguide is given by

$$\left[\nabla \times \left(\frac{1}{\mu_r}\nabla\times\right) - k_0^2\epsilon_r\right]\mathbf{E} = 0 \text{ in } \Omega \tag{2.1}$$

$$\hat{n}\times\mathbf{E} = 0 \text{ on } \Gamma_1 \tag{2.2}$$

where Ω represents the cross section of the waveguide whose boundary is composed of the electrical wall Γ_1, i.e. zero electromagnetic field around the boundary. The equivalent variational problem for this problem with a real dielectric constant ϵ_r and permeability μ_r is given by $\delta F(\mathbf{E}) = 0$, and $\hat{n}\times\mathbf{E} = 0$ on Γ_1 where [98, 103]

$$F(\mathbf{E}) = \frac{1}{2}\iint_\Omega \left[\frac{1}{\mu_r}(\nabla\times\mathbf{E})\cdot(\nabla\times\mathbf{E})^* - k_0^2\epsilon_r\mathbf{E}\cdot\mathbf{E}^*\right]\mathrm{d}\Omega \tag{2.3}$$

Assuming $\mathbf{E}(x,y,z) = \mathbf{E}(x,y)e^{-ik_z z}$, where k_z is the propagation constant, equation (2.3) can be written as

$$\begin{aligned} F(\mathbf{E}) = \frac{1}{2}\iint_\Omega &\left[\frac{1}{\mu_r}(\nabla_t\times\mathbf{E}_t)\cdot(\nabla_t\times\mathbf{E}_t)^* - k_0^2\epsilon_r\mathbf{E}\cdot\mathbf{E}^*\right]\mathrm{d}\Omega \\ &+\left[\frac{1}{\mu_r}(\nabla_t\times E_z + ik_z\mathbf{E}_t)\cdot(\nabla_t\times E_z + ik_z\mathbf{E}_t)^*\right]\mathrm{d}\Omega \end{aligned} \tag{2.4}$$

where $\nabla_t = \frac{\partial}{\partial x}\hat{\mathbf{i}} + \frac{\partial}{\partial y}\hat{\mathbf{j}}$ and $\mathbf{E}_t = E_x\hat{\mathbf{i}} + E_y\hat{\mathbf{j}}$. Using the substitution $\vec{\mathbf{e}_t} = k_z\mathbf{E}_t$ and $e_z = -iE_z$, and multiplying by k_z^2, the functional becomes

$$F(\mathbf{E}) = \frac{1}{2}\iint_\Omega \left[\frac{1}{\mu_r}(\nabla_t \times \mathbf{e}_t)\cdot(\nabla_t \times \mathbf{e}_t)^* - k_0^2\epsilon_r \mathbf{e_t}\cdot\mathbf{e_t}^*\right] \mathrm{d}\Omega \qquad (2.5)$$
$$+ k_z^2\left[\frac{1}{\mu_r}(\nabla_t \times e_z + \mathbf{e_t})\cdot(\nabla_t \times e_z + \mathbf{e_t}^*) - k_0^2\epsilon_r e_z e_z^*\right]\mathrm{d}\Omega$$

This functional can now be discretized to yield an eigenvalue system that can be solved for k_z^2 given a known k_0^2.

2.1.2 Domain Discretization

Discretization of the variational formulation along a waveguide, is achieved by designing a mesh of triangular element as shown in Fig. 2.1. The nodes n_i with $i \in 1, 2, 3$ on the elements are numbered in anti-clockwise orientation, and the edges e_{ti} with $i \in 1, 2, 3$ in each element are numbered as illustrated in 2.1. An open source mesh [104] allows one to generate a mesh for a microwire with a finite cladding (Fig. 2.2).

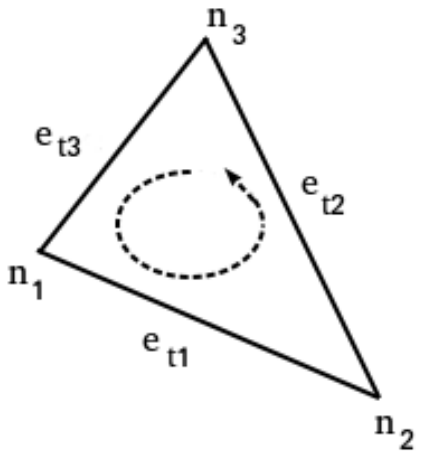

Figure 2.1: Schematic of a single triangular element for the Finite Element Method

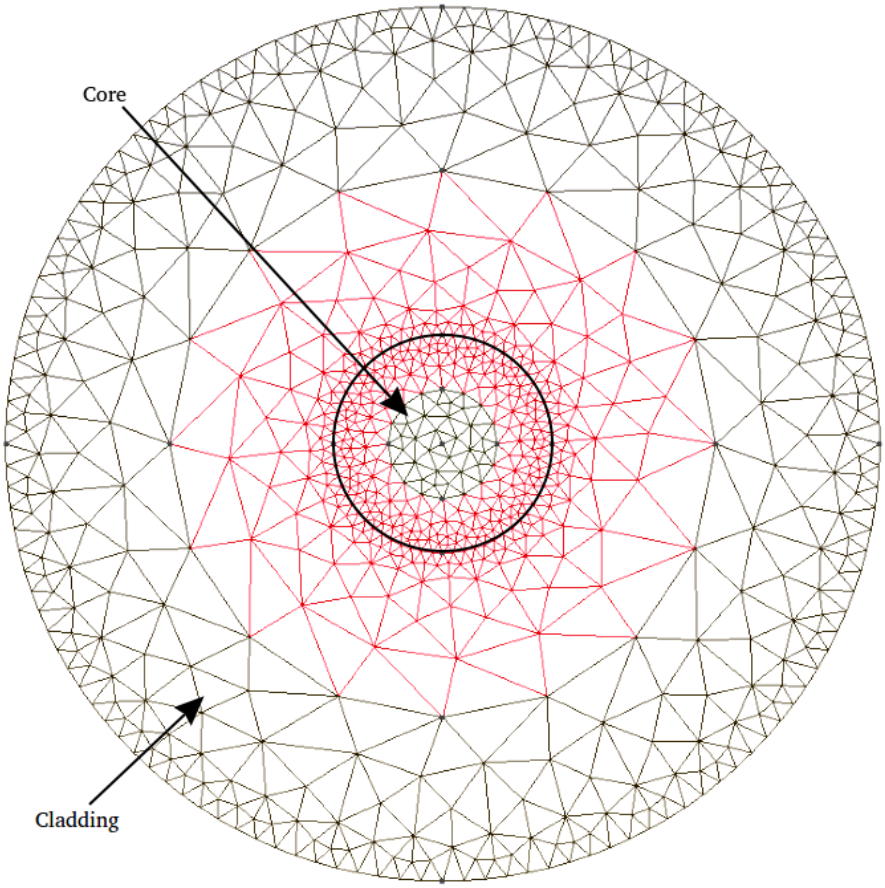

Figure 2.2: Sample of a mesh for the cross-sectional area of microtaper with a finite cladding.

Since approximations of the electric field are determined by first-order interpolation within each element, one requires increased density of the triangular elements in and around the core to guarantee adequate representation of the electric field distribution. The boundary of the mesh is assumed to be a perfect conductor such that the electric field at the outer boundary edges of the mesh is zero. Due to the large refractive index change between the chalcogenide core and the PMMA, the actual diameter of the PMMA cladding is sufficient at ensuring zero field at the boundary, as most of the field is ultra-confined near the core.

2.1.3 Basis Functions

The first order two-dimensional interpolation functions inside each triangular element of a node n_i, with $i \in 1, 2, 3$ is given by the relation [98, 103]

$$L_i = \frac{1}{2\Delta_e}(a_i + b_i x + c_i y) \tag{2.6}$$

where a_i, b_i and c_i are given

$$\begin{aligned} a_1 &= x_2 y_3 - y_2 x_3 \quad b_1 = y_2 - y_3 \quad c_1 = x_3 - x_2 \\ a_2 &= x_3 y_1 - y_2 x_1 \quad b_2 = y_3 - y_1 \quad c_2 = x_1 - x_3 \\ a_3 &= x_1 y_2 - y_1 x_2 \quad b_3 = y_1 - y_2 \quad c_3 = x_2 - x_1 \end{aligned} \tag{2.7}$$

where (x_i, y_i) is the location of each node n_i, and the area of the triangular element Δ_e is given by

$$\Delta_e = \frac{1}{2}\begin{vmatrix} 1 & x_1 & y_1 \\ 1 & x_2 & y_2 \\ 1 & x_3 & y_3 \end{vmatrix} = \frac{1}{2}(b_1 c_2 - b_2 c_1) \tag{2.8}$$

With these expressions, the scalar basis function L_i which represents the z-component of the electric field inside an element e for each node i is given by [98, 103]

$$e_z = \sum_{i=1}^{3} L_i^e e_{zi}^e = \{L^e\}^T \{e_z^e\} = \{e_z^e\}^T \{L^e\} \tag{2.9}$$

Similarly, vector basis functions $\vec{N}_k = l_k(L_i \nabla L_j - L_j \nabla L_i)$ represent the tangential component of the electric field that are defined inside an element e for each edge k connecting node i to node j. Here, l_k is the length of the edge e_{tk} and $\nabla L_i =$

$(1/2\Delta_e)(b_i\hat{\mathbf{i}} + c_i\hat{\mathbf{j}})$. These basis functions satisfy the following identities [98, 103]:

$$\begin{aligned} \vec{\nabla} \cdot \vec{N_k} &= 0, \\ \vec{\nabla} \times \vec{N_k} &= \frac{l_k}{\Delta_e}, \\ \vec{e_{tk}} \cdot \vec{N_k} &= 1 \end{aligned} \tag{2.10}$$

The tangential component of the electric field in the cross-section can then be expressed using vector basis functions N_i as follows

$$\vec{e_t} = \sum_{i=1}^{3} \vec{N_i^e} e_{ti}^e = \left\{\vec{N^e}\right\}^T \{e_t^e\} = \{e_t^e\}^T \left\{\vec{N^e}\right\} \tag{2.11}$$

2.1.4 The Ritz Formulation

Using $e_z = \{e_z^e\}^T \{L^e\}$ and $\vec{e_t} = \{e_z^e\}^T \left\{\vec{N^e}\right\}$, we discretize the functional to the following summation [98, 103]

$$F(\vec{e}) = \frac{1}{2} \sum_{e=1}^{M} \left(\{e_z^e\}^T [A_{tt}^e] \{e_z^e\}^* + k_z^2 \begin{Bmatrix} e_t^e \\ e_z^e \end{Bmatrix}^T \begin{bmatrix} B_{tt}^e & B_{tz}^e \\ B_{zt}^e & B_{zz}^e \end{bmatrix} \begin{Bmatrix} e_t^e \\ e_z^e \end{Bmatrix}^* \right) \tag{2.12}$$

where the elemental matrices are given by

$$[A_{tt}^e] = \iint_{\Omega_e} \left[\frac{1}{\mu_r^e} \left\{\vec{\nabla}_t \times \vec{N^e}\right\} \cdot \left\{\vec{\nabla}_t \times \vec{N^e}\right\}^T - k_0^2 \epsilon_r^e \left\{\vec{N^e}\right\} \left\{\vec{N^e}\right\}^T \right] \mathrm{d}\Omega \tag{2.13}$$

$$[B_{tt}^e] = \iint_{\Omega_e} \frac{1}{\mu_r^e} \left\{\vec{N^e}\right\} \cdot \left\{\vec{N^e}\right\}^T \mathrm{d}\Omega \tag{2.14}$$

$$[B_{tz}^e] = \iint_{\Omega_e} \frac{1}{\mu_r^e} \left\{\vec{N^e}\right\} \cdot \left\{\vec{\nabla}_t L^e\right\}^T \mathrm{d}\Omega \tag{2.15}$$

$$[B_{zt}^e] = \iint_{\Omega_e} \frac{1}{\mu_r^e} \left\{\vec{\nabla}_t L^e\right\} \cdot \left\{\vec{N^e}\right\}^T \mathrm{d}\Omega \tag{2.16}$$

$$[B_{zz}^e] = \iint_{\Omega_e} \left[\frac{1}{\mu_r^e} \left\{\vec{\nabla}_t L^e\right\} \cdot \left\{\vec{\nabla}_t L^e\right\}^T - k_0^2 \epsilon_r^e \{L^e\} \{L^e\}^T \right] \mathrm{d}\Omega \tag{2.17}$$

Here, Ω_e represents the area of the element e, with (ϵ_r^e, μ_r^e) being the relative permittivity and permeability of the element. By using the global notation, the functional

can then be written as

$$F(\vec{e}) = \frac{1}{2}\{e_z\}^T [A_{tt}] \{e_z\}^* + \frac{1}{2}k_z^2 \begin{Bmatrix} e_t \\ e_z \end{Bmatrix}^T \begin{bmatrix} B_{tt} & B_{tz} \\ B_{zt} & B_{zz} \end{bmatrix} \begin{Bmatrix} e_t \\ e_z \end{Bmatrix}^* \tag{2.18}$$

Finally, applying the Ritz procedure [98, 103], one obtains the generalized eigenvalue problem

$$\begin{bmatrix} A_{tt} & 0 \\ 0 & 0 \end{bmatrix} \begin{Bmatrix} e_t \\ e_z \end{Bmatrix} = -k_z^2 \begin{bmatrix} B_{tt} & B_{tz} \\ B_{zt} & B_{zz} \end{bmatrix} \begin{Bmatrix} e_t \\ e_z \end{Bmatrix} \tag{2.19}$$

This can be solved directly using the Krylov-Schur algorithm, which is ideal when when one is only looking for a finite number of eigenvectors.

2.2 Characteristic Equation for Step-Index Fiber Waveguides

In this section, we present an analysis of step-index cylindrical fiber waveguides used for modelling microwires with a refractive index profile as shown in Fig. 2.3. From this analysis, we obtain the effective propagation constant of the modes that are propagating in the microwire.

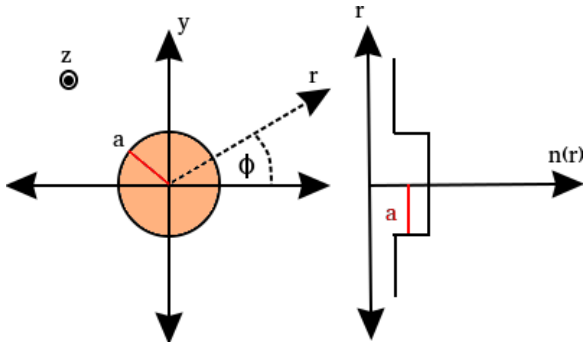

Figure 2.3: Schematic of a step-index with an infinite cladding.

The propagation of an optical field is governed by the Maxwell equations, which

take the form

$$\vec{\nabla} \times \vec{E} = \frac{-\partial \vec{B}}{\partial t} \tag{2.20}$$

$$\vec{\nabla} \times \vec{H} = \vec{J} + \frac{-\partial \vec{D}}{\partial t} \tag{2.21}$$

$$\vec{\nabla} \cdot \vec{D} = \rho \tag{2.22}$$

$$\vec{\nabla} \times \vec{B} = 0 \tag{2.23}$$

where $\vec{E}$ and $\vec{H}$ are the electric and magnetic field vectors, respectively, and $\vec{D}$ and $\vec{B}$ are the corresponding electric and magnetic flux densities. The current density vector $\vec{J}$ and the charge density ρ represent the sources for the electromagnetic field. In the absence of free charges, $\vec{J} = 0$ and $\rho = 0$. The flux densities $\vec{D}$ and $\vec{B}$ are given by

$$\vec{D} = \epsilon_0 \vec{E} + \vec{P} \tag{2.24}$$

$$\vec{B} = \mu_0 \vec{H} + \vec{M} \tag{2.25}$$

with $\vec{P}$ and $\vec{M}$ being the induced electric and magnetic fields respectively. In the case of dielectrics, $\vec{M} = 0$. Applying the curl to equation (2.20), and using (2.21), we get the following expression

$$\vec{\nabla} \times \vec{\nabla} \times \vec{E} = \mu_0 \frac{-\partial}{\partial t}(\vec{\nabla} \times \vec{H}) = -\mu_0 \frac{\partial^2 \vec{D}}{\partial t^2} \tag{2.26}$$

Applying the vector identity $\vec{\nabla} \times \vec{\nabla} \times \vec{E} = \nabla(\vec{\nabla} \cdot \vec{E}) - \nabla^2 \vec{E}$, and since $\nabla(\vec{\nabla} \cdot \vec{E}) = 0$ for a homogeneous medium where the refractive index is the same everywhere, equation (2.26) becomes

$$\nabla^2 \vec{E} = \mu_0 \epsilon_0 \frac{\partial^2 \vec{E}}{\partial t^2} + \mu_0 \frac{\partial^2 \vec{P}}{\partial t^2} \tag{2.27}$$

When written in the frequency domain, the equation takes form of the Helmholtz

equation:

$$\nabla^2 \vec{E}(\vec{r},\omega) = -\frac{\omega^2}{c^2}\epsilon(\omega)\vec{E}(\vec{r},\omega) \tag{2.28}$$

where $c^2 = 1/\mu_0\epsilon_0$ and $\epsilon(\omega) = 1 + \chi^1(\omega)$. $\chi^1(\omega)$ is the Fourier transform of the linear susceptibility, allowing us to relate the linear polarization $\vec{P}(\vec{r},\omega)$ and the electric field $\vec{E}(\vec{r},\omega)$ as $\vec{P}(\vec{r},\omega) = \chi^1(\omega)\vec{E}(\vec{r},\omega)$.

In order to solve the Helmholtz equation for the step-index optical fiber, it is convenient to rewrite the equation in cylindrical coordinates ρ, ϕ and z [1]

$$\frac{\partial^2\vec{E}}{\partial\rho^2} + \frac{1}{\rho}\frac{\partial\vec{E}}{\partial\rho} + \frac{1}{\rho^2}\frac{\partial^2\vec{E}}{\partial\phi^2} + \frac{\partial^2\vec{E}}{\partial z^2} + \frac{n^2\omega^2}{c^2}\vec{E} = 0 \tag{2.29}$$

We can express a similar equation for the magnetic field $\vec{H}(\vec{r},\omega)$. Since $\vec{E}$ and $\vec{H}$ also satisfy Maxwell's equations (2.20), (2.21), only two components out of six are independent. It is adequate to choose H_z and E_z as the two independent components and derive the remaining components $E_\rho, E_\phi, H_\rho, H_\phi$ in terms of H_z and E_z. The wave equation for E_z can be solved easily by using the method of separation of variables, resulting in the following general solution:

$$\vec{E}(\vec{r},\omega) = A(\omega)F(\rho)e^{im\phi}e^{i\beta z} \tag{2.30}$$

where β is the propagation constant, m is an integer, and $F(\rho)$ is a radial function that satisfies the following condition:

$$\frac{\mathrm{d}^2F}{\mathrm{d}^2\rho^2} + \frac{1}{\rho}\frac{\mathrm{d}^2F}{\mathrm{d}^2\rho} + \left(n^2k_0^2 - \beta^2 - \frac{m^2}{\rho^2}\right)F = 0 \tag{2.31}$$

where $k_0^2 = \omega^2/c^2$. The refractive index $n = n_1$ for $\rho \leq a$ for a fiber core radius a, and $n = n_c$ otherwise. This differential equation is satisfied by the well-known Bessel

functions. Hence, the general guided solution is [1, 98]

$$F(\rho) = \begin{cases} J_m(p\rho), & \rho \leq a \\ K_m(q\rho), & \rho > a \end{cases} \tag{2.32}$$

where $p = \sqrt{n_1^2 k_0^2 - \beta^2}$ and $q = \sqrt{\beta^2 - n_c^2 k_0^2}$. Since both E_z and H_z satisfy the same wave equations, we can represent both the electric and magnetic fields as follows:

$$E_z = \begin{cases} AJ_m(p\rho)e^{im\phi}e^{i\beta z}, & \rho \leq a \\ CK_m(q\rho)e^{im\phi}e^{i\beta z}, & \rho > a \end{cases} \quad H_z = \begin{cases} BJ_m(p\rho)e^{im\phi}e^{i\beta z}, & \rho \leq a \\ DK_m(q\rho)e^{im\phi}e^{i\beta z}, & \rho > a \end{cases} \tag{2.33}$$

The boundary condition that the tangential components of $\vec{E}$ and $\vec{H}$ be continuous across the core-cladding interface requires that all six components be the same at $\rho = a$ from the inside and outside. This leads to a characteristic equation whose solutions determine the unknown propagation vector β for the fiber modes. The procedure is well defined in [1], and leads to the following characteristic equation:

$$\left[\frac{J_m'(pa)}{pJ_m(pa)} + \frac{K_m'(qa)}{qK_m(qa)}\right]\left[\frac{J_m'(pa)}{pJ_m(pa)} + \frac{n_c^2}{n_1^2}\frac{K_m'(qa)}{qK_m(qa)}\right] = \left(\frac{m\beta k_0(n_1^2 - n_c^2)}{an_1p^2q^2}\right)^2 \tag{2.34}$$

There are several general solutions for β for a given m, and they are written as β_{mn}. Each β_{mn} eigenvalue corresponds to two specific modes supported by the fiber, designated as the HE_{mn} and EH_{mn} modes. When $m = 0$, the eigenmodes are analogous to the transverse-electric (TE) and transverse-magnetic (TM) modes that consist of a zero axial contribution of the fields. However, this condition is only possible due to the analytical condition when $\nabla(\vec{\nabla} \cdot \vec{E}) = 0$ [1]. If these conditions are not imposed, as it is the case in our finite-element methods, the fundamental mode of the fiber is a hybrid, i.e., all six components of electromagnetic field are non-zero. Single mode fibers only support the HE_{11} mode., known as the fundamental mode of the fiber [1].

Hence, we will be using the propagation constant derived using the Vector Finite-Element method and compare it with the propagation constant β_{11} derived from the characteristic equation in order to validate our computational method, as well as characterize the Brillouin gain profile that arises from the electrostriction within the microwires.

2.3 Derivation of Electrostriction in Cylindrical Waveguides

In this section, we investigate the direct generation of acoustic phonons from electrostriction in optical fibers, based purely on the knowledge of the fiber geometry and material properties, and of the particular incident guided optical waves. Specifically, we will be using finite-element calculations to solve elastodynamic equations for a fiber with an arbitrary cross-sectional profile in the presence of an optical force. Lastly, we derive the computed phonon energy as a function of the detuned optical frequency in order to explain both the backward and the forward electrostriction and provide an estimation for the efficiency of the process.

2.3.1 Elastodynamic Equation

The elastodynamic equation describing the electrostriction of an acoustic phonon wavepacket in the presence of two optical fields is written as follows [28, 74]:

$$\rho\frac{\partial^2 u_i}{\partial t^2} - \left[c_{ijkl}u_{k,l} + \eta_{ijkl}\frac{\partial u_{k,l}}{\partial t}\right]_{,j} = \left[\epsilon_0\chi_{klij}E_k E_l^*\right]_{,j} \tag{2.35}$$

with

$$\chi_{klij} = \quad \epsilon_{im}\epsilon_{jn}p_{klmn} \tag{2.36}$$

where u_i is the displacement field, E_i is the incident optical field contributing to the electrostriction in the acoustic waveguide, ρ is the material density, $\epsilon_{ij} = n^2\delta_{ij}$

is the relative dielectric tensor, and c_{ijkl} , η_{ijkl} and p_{klmn} are the rank-4 elastic, viscosity, photoelastic tensors respectively (Note: $A_{ij,j} = \sum_j \partial A_{ij}/\partial x_j$) . Note that the transverse variations of the two incident optical waves are fully taken into account when defining the electrostriction stress tensor $T_{ij}^{es} = \epsilon_0 \chi_{klij} E_k E_l^*$. The electrostrictive force is defined as the divergence of the electrostriction stress tensor, $T_{ij,j}^{es}$.

Assumptions for the Optical and Acoustic Fields in SBS and GAWBS

Brillouin scattering processes are third-order nonlinear parametric processes involving two optical fields and one acoustic field. Hence, phase-matching conditions must be achieved in order for the interaction to build constructively. In our case, a pump optical field with central frequency ω_1 and wavenumber k_1 can produce a down-shifted Stokes optical field characterized by a central frequency ω_2 and wavenumber k_2 when scattering by an acoustic wave of frequency $\omega = \omega_1 - \omega_2$ and wavenumber $k = k_1 - k_2$. The incident optical field is a superposition of two monochromatic waves with frequencies ω_1 and ω_2 and wavevectors k_1 and k_2:

$$\vec{E}(r, z; t) = \vec{E}^1(r, z) e^{i(\omega_1 t - k_1 z)} + \vec{E}^2(r, z) e^{i(\omega_2 t - k_2 z)} \tag{2.37}$$

Since we are considering acoustic waves, ω is much smaller than ω_1 and ω_2. However, the wavenumber for the acoustic wave can be classified into two separate cases. If the optical waves are counter-propagating, then the phase-matching conditions for SBS are achieved, with $k_1 \approx -k_2$, so that the wavenumber of the acoustic wave is $k \approx k_1 + k_2 \approx 2k_1$. However, if the two optical fields are co-propagating, the phase-matching conditions describe a GAWBS, with $k_1 \approx -k_2$ and $k \approx 0$. Since there is only one source term at frequency detuning $\omega = \omega_1 - \omega_2$ and wavenumber $k = k_1 - k_2$, the following ansatz is assumed for the acoustic wave:

$$\vec{u}(r, z; t) = \vec{\overline{u}}(r) e^{i(\omega t - K z)} \tag{2.38}$$

where the displacement field $\overline{u}_i(r)$ represents the transverse profile of the acoustic wave. We solve for this unknown field by setting k and scanning over the detuned frequency ω. Since the displacement fields are supposed to be a continuous field defined on a arbitrary configuration of various materials with exact boundary conditions, a finite element model is a natural choice.

Dielectric Tensor Assumption

We assume the refractive index to be a constant: $\epsilon_{ij} = n^2\delta_{ij}$, which simplifies equation (2.36) to:

$$\chi_{klij} = n^4 p_{klij} \tag{2.39}$$

Assumptions for the Elastic and Viscosity Tensors

The elastic tensor c_{ijkl} is a rank-4 tensor that relates all the components of the stress tensor linearly to the strain tensor, and is used to generalize the linear Hooke's Law [4, 104]

$$\sigma_{ij} = c_{ijkl}\epsilon_{kl} \tag{2.40}$$

where σ_{ij} and ϵ_{kl} are the rank-2 stress and strain tensors respectively. Although c_{ijkl} is allowed to have 81 independent constants, several of these constants will be the same due to the symmetry of the rank-2 tensors $\sigma_{ij} = \sigma_{ji}$ and $\epsilon_{ij} = \epsilon_{ji}$, reducing c_{ijkl} down to only 36 components. By exploiting these symmetries, we can write down the

stress-strain relations for a linear elastic material as follows

$$\begin{bmatrix} \sigma_{11} \\ \sigma_{22} \\ \sigma_{33} \\ \sigma_{23} \\ \sigma_{31} \\ \sigma_{12} \end{bmatrix} = \begin{bmatrix} c_{1111} & c_{1122} & c_{1133} & c_{1123} & c_{1131} & c_{1112} \\ c_{2211} & c_{2222} & c_{2233} & c_{2223} & c_{2231} & c_{2212} \\ c_{3311} & c_{3322} & c_{3333} & c_{3323} & c_{3331} & c_{3312} \\ c_{2311} & c_{2322} & c_{2333} & c_{2323} & c_{2331} & c_{2312} \\ c_{3111} & c_{3122} & c_{3133} & c_{3123} & c_{3131} & c_{3112} \\ c_{1211} & c_{1222} & c_{1233} & c_{1223} & c_{1231} & c_{1212} \end{bmatrix} \begin{bmatrix} \epsilon_{11} \\ \epsilon_{22} \\ \epsilon_{33} \\ 2\epsilon_{23} \\ 2\epsilon_{31} \\ 2\epsilon_{12} \end{bmatrix} \tag{2.41}$$

Since the tensor notation is impractical to use for an equation that is now defined with a matrix, we introduce what is known as the Voigt notation (or contracted notation) for the stress-strain equation

$$\begin{bmatrix} \sigma_1 \\ \sigma_2 \\ \sigma_3 \\ \sigma_4 \\ \sigma_5 \\ \sigma_6 \end{bmatrix} = \begin{bmatrix} c_{11} & c_{12} & c_{13} & c_{14} & c_{15} & c_{16} \\ c_{21} & c_{22} & c_{23} & c_{24} & c_{25} & c_{26} \\ c_{31} & c_{32} & c_{33} & c_{34} & c_{35} & c_{36} \\ c_{41} & c_{42} & c_{43} & c_{44} & c_{45} & c_{46} \\ c_{51} & c_{52} & c_{53} & c_{54} & c_{55} & c_{56} \\ c_{61} & c_{62} & c_{63} & c_{64} & c_{65} & c_{66} \end{bmatrix} \begin{bmatrix} \epsilon_1 \\ \epsilon_2 \\ \epsilon_3 \\ \epsilon_4 \\ \epsilon_5 \\ \epsilon_6 \end{bmatrix} \tag{2.42}$$

where the pair of indices have been combined as follows: $()_{11} \rightarrow ()_1, ()_{22} \rightarrow ()_2, ()_{33} \rightarrow ()_3, ()_{23} \rightarrow ()_4, ()_{31} \rightarrow ()_5, ()_{12} \rightarrow ()_6$; and the new shear strains are the sum of the symmetric components: $\epsilon_4 = \epsilon_{23} + \epsilon_{32} = 2\epsilon_{23}$.

These 36 components c_{ij} can again be reduced down to a much smaller number of parameters as we take into account the symmetries of the internal structure of the material. The more the symmetries, the simpler the structure of the elastic tensor. For our case, we assume our materials to consist of a cubic linear elastic tensor, which

reduces the stress-strain relations to only 3 components as follows:

$$c_{ij} = \begin{bmatrix} c_{11} & c_{12} & c_{12} & 0 & 0 & 0 \\ c_{12} & c_{11} & c_{12} & 0 & 0 & 0 \\ c_{12} & c_{12} & c_{11} & 0 & 0 & 0 \\ 0 & 0 & 0 & c_{44} & 0 & 0 \\ 0 & 0 & 0 & 0 & c_{44} & 0 \\ 0 & 0 & 0 & 0 & 0 & c_{44} \end{bmatrix} \tag{2.43}$$

In order to simulate the Brillouin interaction, elastic losses need to be incorporated into the elastodynamic equation by considering a a complex elastic tensor $c_{ij} + i\omega\eta_{ij}$ where η_{ij} is the viscosity tensor. In our case, we assume $\eta_{ij} = c_{ij}/Qf$ where Qf is the product of the quality factor Q and frequency f. This Qf product is assumed to be a constant for a given material. Since the quality factors are hardly available in the literature for most materials, the Qf product is the only parameter that is adjusted in our model.

Assumptions for the Photo-elastic Tensor

Brillouin Scattering in large core silica and chalcogenide waveguides has been broadly documented and demonstrated experimentally in past literature [6]. With the photoelastic tensor written p_{IJ} in contracted notation (I and J being integers with values between 1 and 6) the literature generally attributes SBS to the large p_{12} value, that is favourable for longitudinal waves [2, 6]. Although the electric field is very nearly transverse in large core diameters, this is not necessarily true for smaller core waveguide. However, we can still assert that the transverse components dominate. As a result, only the values for $I, J = 1, 2$ and 6 have to be regarded among tensor components p_{IJ}. For our case, p_{IJ} also has the same symmetries as c_{IJ} and η_{IJ}, thus only having three independent constants [74].

2.3.2 Finite-Element Model for the Elastodynamic Equation

Here, we describe how a finite element model can be derived from the elastodynamic equation subject to an electrostrictive force. We first obtain the fundamental optical mode from the Tangential Vector Finite Element Formulation for electromagnetic waveguide as described in section [28, 74]. Equation 2.35 is expanded to:

$$-\rho\omega^2\overline{u}_i e^{-iKz} - \left[\left(c_{ijkl} + i\omega\eta_{ijkl}\right)\left(\overline{u}_k e^{-iKz}\right)_{,l}\right]_{,j} = \left[\epsilon_0 n^4 p_{klij} E_k^1 \left(E_l^2\right)^* e^{-iKz}\right]_{,j} \quad (2.44)$$

We will now construct this into a variational problem by left-multiplying a virtual displacement $\left(\overline{v}_i e^{-iKz}\right)^*$ and integrating over the cross-section of the waveguide.

$$\begin{aligned} -\omega^2 \iint_\sigma \mathrm{d}\sigma\, \rho\overline{v}_i^*\overline{u}_i \quad &- \iint_\sigma \mathrm{d}\sigma\, \overline{v}_i^* e^{iKz}\left[\left(c_{ijkl} + i\omega\eta_{ijkl}\right)\left(\overline{u}_k e^{-iKz}\right)_{,l}\right]_{,j} \\ &= \epsilon_0 n^4 \iint_\sigma \mathrm{d}\sigma\, \overline{v}_i^* e^{iKz}\left[p_{klij} E_k^1 \left(E_l^2\right)^* e^{-iKz}\right]_{,j} \end{aligned} \quad (2.45)$$

We will now apply product rule, followed by Green's Theorem:

$$\iint_\sigma \mathrm{d}\sigma\, a_i \left[b_{ij}\right]_{,j} = \iint_\sigma \mathrm{d}\sigma\, \left[a_i b_{ij}\right]_{,j} - \iint_\sigma \mathrm{d}\sigma\, \left[a_i\right]_{,j} b_{ij} = \oint_{\delta\sigma} \mathrm{d}\delta\sigma\, a_i b_{ij} n_j - \iint_\sigma \mathrm{d}\sigma\, \left[a_i\right]_{,j} b_{ij} \quad (2.46)$$

which gives us:

$$\begin{aligned} -\omega^2 \iint_\sigma \mathrm{d}\sigma\, \rho\overline{v}_i^*\overline{u}_i \quad &+ \iint_\sigma \mathrm{d}\sigma\, \left[\overline{v}_i^* e^{iKz}\right]_{,j}\left(c_{ijkl} + i\omega\eta_{ijkl}\right)\left(\overline{u}_k e^{-iKz}\right)_{,l} \\ &+ \epsilon_0 n^4 \iint_\sigma \mathrm{d}\sigma\, \left[\overline{v}_i^* e^{iKz}\right]_{,j} p_{klij} E_k^1 \left(E_l^2\right)^* e^{-iKz} \\ &= \oint_{\delta\sigma} \mathrm{d}\delta\sigma\, \overline{v}_i^* e^{iKz}\left(c_{ijkl} + i\omega\eta_{ijkl}\right)\left(\overline{u}_k e^{-iKz}\right)_{,l} n_j \\ &+ \epsilon_0 n^4 \oint_{\delta\sigma} \mathrm{d}\delta\sigma\, \overline{v}_i^* e^{iKz} p_{klij} E_k^1 \left(E_l^2\right)^* e^{-iKz} n_j \end{aligned} \quad (2.47)$$

The boundary integral is along $\delta\sigma$ and $\vec{n}$ is the outward normal. The above equations can be simplified using the following definitions:

- Stress Tensor $T_{ij}e^{-iKz} = \left(c_{ijkl} + i\omega\eta_{ijkl}\right)\left(\overline{u}_k e^{-iKz}\right)_{,l}$

- Electrostrictive Tensor $T_{ij}^{es}e^{-iKz} = -\epsilon_0 n^4 p_{klij} E_k^1 \left(E_l^2\right)^* e^{-iKz}$

We can also now apply the natural boundary condition $T_{ij} - T_{ij}^{es} = 0$ along the closed loop $\delta\sigma$, meaning that the total stress vanishes on the boundary of the waveguide. Hence, this gives us:

$$-\omega^2 \int_\sigma \mathrm{d}\sigma\, \rho \overline{v}_i^* \overline{u}_i + \int_\sigma \left[\overline{v}_i^* e^{iKz}\right]_{,j} \left(c_{ijkl} + i\omega\eta_{ijkl}\right) \left(\overline{u}_k e^{-iKz}\right)_{,l} + \int \mathrm{d}\sigma\, \left[\overline{v}_i^* e^{iKz}\right]_{,j} T_{ij}^{es} e^{-iKz} = \oint_{\delta\sigma} \mathrm{d}\delta\sigma\, \overline{v}_i^* e^{iKz} \cancelto{0}{\left(T_{ij} - T_{ij}^{es}\right)} e^{-iKz} n_j = 0 \tag{2.48}$$

Further calculation can be conducted to remove the $e^{\pm iKz}$ terms by explicitly separating the partial derivatives with respect to z. This finally gives us:

$$\begin{aligned} -\omega^2 \int_\sigma \mathrm{d}\sigma\, \rho \overline{v}_i^* \overline{u}_i + \int_\sigma \mathrm{d}\sigma\, \overline{v}_{i,j}^* \left(c_{ijkl} + i\omega\eta_{ijkl}\right) \overline{u}_{k,l} \\ + iK \int_\sigma \mathrm{d}\sigma\, \left[\overline{v}_i^* \left(c_{i3kl} + i\omega\eta_{i3kl}\right) \overline{u}_{k,l} - \overline{v}_{i,j}^* \left(c_{ijk3} + i\omega\eta_{ijk3}\right) \overline{u}_k\right] \\ + K^2 \int_\sigma \mathrm{d}\sigma\, \overline{v}_i^* \left(c_{i3k3} + i\omega\eta_{i3k3}\right) \overline{u}_k = \int_\sigma \mathrm{d}\sigma\, \overline{v}_{i,j}^* T_{ij}^{es} + iK \int_\sigma \mathrm{d}\sigma\, \overline{v}_i^* T_{i3}^{es} \end{aligned} \tag{2.49}$$

Converting the integral into a linear equation is achieved by writing U and T^{es} as the vectors of the nodal values of $\overline{u}_i$ and T_{ij}^{es} and applying the Galerkin FEM procedure on the discretized domain [74]:

$$\left(C + iKC_1 + K^2 C_2 - \omega^2 M\right) U = \left(X_0 + iKX_1\right) T_{es} \tag{2.50}$$

where each of the matrices comes from the linearization of the integrals in equation (2.3.2).

2.3.3 Determining Energy of Photon Wavepacket.

Upon obtaining the displacement fields, we find it useful to calculate the total energy of the phonon wavepacket. First, we find the kinetic energy of the acoustic wave, as defined by

$$E_k = \frac{1}{4}\iint_\sigma \mathrm{d}r\ \rho\omega^2 u_i(r)^* u_i(r) \tag{2.51}$$

Next, the elastic or potential energy is

$$E_p = \frac{1}{4}\iint_\sigma \mathrm{d}r\ u_{i,j}(r)^* c_{ijkl} u_{k,l}(r) \tag{2.52}$$

If the solution were a normal mode, then the elastic energy would be equal to the kinetic energy. As the internal energy is the sum of the kinetic and elastic energies, we estimate the acoustic wave energy as [28, 74]

$$E = E_k + E_p \approx 2E_k \tag{2.53}$$

We thus have access to both the Brillouin spectrum and spatial distribution of the three displacement components. Both the forward and backward interaction configurations can be considered, as well as any value of the k-vector. In addition to this, the electrostriction force and the generated acoustic wave are obtained right where the interaction takes place. Hence, the model is capable of calculating the Brillouin gain characteristic for any structure with any arbitrary refractive index and material composition.

2.4 Parameters for Simulating the EM Waves and Electrostriction in custom microwires

Simulation for deriving electromagnetic fields, as well as the electrostriction between two optical fields using Finite-Element Methods was carried out using the FEniCS en-

vironment on Python [104]. The parameters used for the partial differential equations in equation 2.35 are as follows:

Parameter	**PMMA**	**As_2Se_3**	**SMF28 core**	**SMF28 cladding**
n	1.481	2.674	1.4492	1.4444
$\rho\,(\mathrm{kg}/m^3)$	1187	4640	2254	2203
p_{11}	0.30	0.314	0.12	0.12
p_{12}	0.297	0.266	0.27	0.27
p_{44}	0	0.024	-0.073	-0.073
c_{11}(GPa)	3.03	23.5	76	78
c_{12}(GPa)	5.46	9.5	16.15	16.5
c_{44}(GPa)	0	6.99	29.9	30
Qf product (GHz)	70	2000	5000	5000

Table 2.1: As_2Se_3, PMMA and SMF28 parameters used for electrostriction calculations [27, 28, 105, 106]

For the simulations, we will be using the standard silica fiber (SMF28) as a benchmark to verify the results for both the electromagnetic field and the acoustic phonon energy with the literature that is currently available for this fiber.

2.5 Testing Finite-Element Method Simulations on SMF28

This section focuses on the results obtained from the Finite-Element Method for both the optical field for a cylindrical step-index waveguide, as well as the acoustic energy derived from the elastodynamic equation that is driven by two counter-propagating or co-propagation frequency detuned optical fields. Although our primary goal is to determine the profile of the optical and acoustic waves for our hybrid microtapers, we have also conducted similar simulation for the standard silica optical fiber (SMF28) to provide the reader with a benchmark for how accurate the results are with comparison

to what is known in the literature.

2.5.1 Verification of the Electromangetic Field

Figures 2.4 and 4.1 show the spatial distribution of the fundamental mode HE_{11} for the SMF28 and the hybrid microtaper that have been derived using the finite element model mentioned in section 2.1.

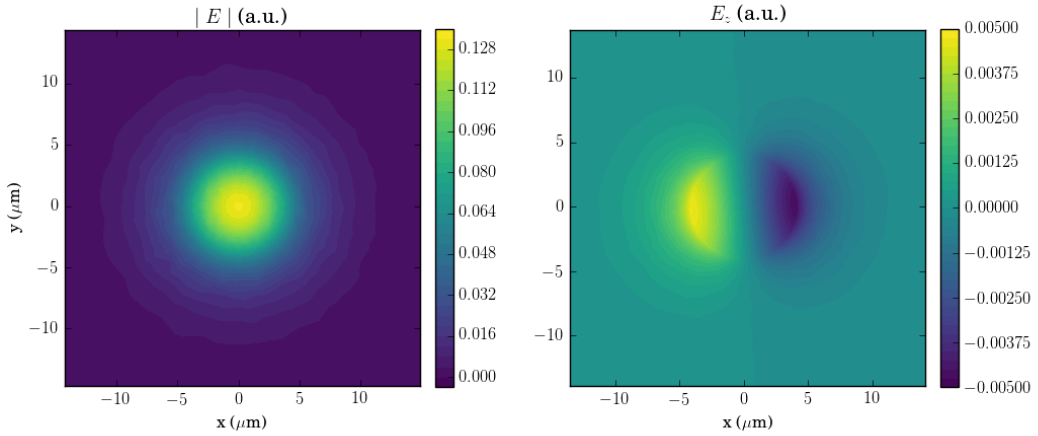

Figure 2.4: Spatial distribution of the (*left*) magnitude and the (*right*) z component of mode HE_{11} in standard SMF28.

As expected for the SMF28, the derived HE_{11} mode is weakly guided, and a large portion of the field penetrates through the 4.2 μm core into the cladding. Also, the field is predominantly transverse in nature, as the magnitude of the E_z component is almost 2 orders of magnitude smaller when compared to the tangential components E_x and E_y, making its contribution almost negligible.

Another way to confirm the accuracy of the simulation is to compare the calculated effective refractive index $n_{eff} = \beta/k$ of the fundamental mode with the exact value derived using equation (2.2). The results are shown in Table 2.2.

Fiber	$\mathbf{n}_{core}$	$\mathbf{n}_{clad}$	$\mathbf{n}_{eff}^{(exact)}$	$\mathbf{n}_{eff}^{(FEM)}$	**error** $= \frac{\mid n_{eff}^{(exact)} - n_{eff}^{(FEM)} \mid}{n_{core} - n_{clad}}$
SMF28	1.4492	1.4440	1.4461	1.4462	0.019

Table 2.2: Comparison between predicted and calculated value of n_{eff} for SMF28 using known parameters for n_{core} and n_{clad}

2.5.2 Results for Electrostriction Model in SMF28

Here, we have calculated the forward ($k = 0$) and the backward ($k = 2k_1$) electrostriction spectra for the single mode-fiber SMF28 as shown in figures 2.5.(a) and 2.6.(a) respectively. These spectra have been obtained by evaluating the kinetic energy of the acoustic beam (i.e. $\omega^2 \int_S \rho \mid u_i \mid^2$ as a function of the detuning frequency between the two optical fields of the fundamental mode.

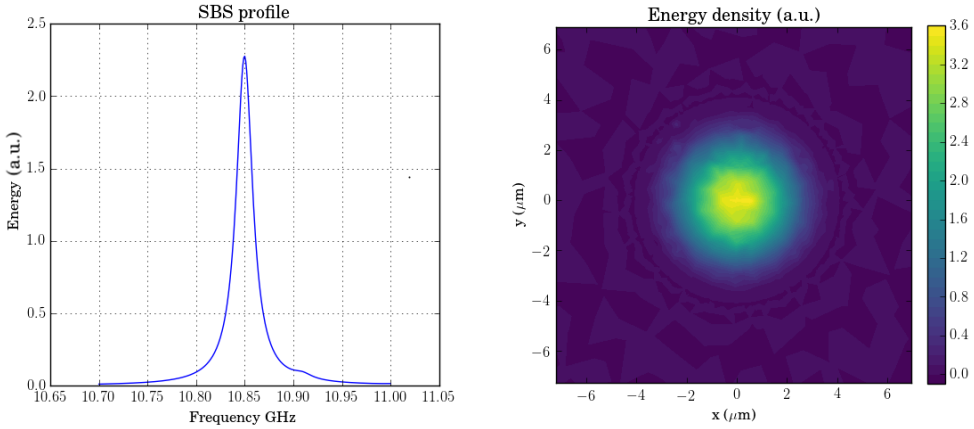

Figure 2.5: (*left*) Numerical results for the backward scattered spectra for SMF28 as a function of detuning frequency. (*right*) Computed acoustic energy density at 10.85 GHz.

In the backward case, the results are in good agreement with the standard SBS spectrum that are obtained in SMF28, with a single dominant Lorentzian peak centered around 10.85 GHz which is close to what is obtained using the relation $\Omega_B = 2\pi n_e f f v_a/\lambda$ [1, 2] (where v_a is the speed of sound in silica) and a known linewidth of around 20 MHz [2, 3]. The acoustic energy density at this resonance is

shown in figure 2.5.(b). The acoustic beam is mostly confined to the core of both fibers. The displacement is dominantly longitudinal, although transverse displacements do not vanish.

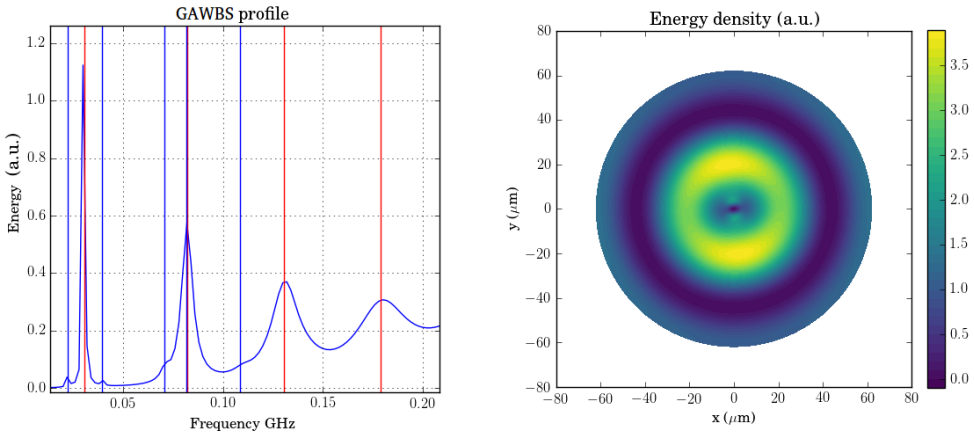

Figure 2.6: (*left*) Numerical results for the forward scattered spectra for SMF28 as a function of detuning frequency. The theoretical peaks for the first few $TR_{2,m}$ are indicated in blue, and the first few $RM_{0,m}$ are indicated in red. (*right*) Computed acoustic energy density at 0.082 GHz, which contains contributions from both the radially asymmetric $TR_{2,4}$ mode (resonant at 0.08165 GHz) and the symmetric mode $RM_{0,2}$ (resonant at 0.08204 GHz).

In the forward case, the simulation gives rise to several resonant peaks which correspond to the Radial Acoustic Modes $R_{0,m}$ and the Torsional-Radial Modes $TR_{2,m}$. The cut-off frequencies for the $R_{0,m}$ modes are determined by [13]

$$f_{0,m} = \eta_m V_d/(2\pi a) \tag{2.54}$$

where V_d is the longitudinal acoustic velocity, a is the radius of the fiber cladding, and η_m is the m^{th} order solution to the equation

$$(1-\alpha^2)J_0(\eta) - \alpha^2 J_2(\eta) = 0 \tag{2.55}$$

where $\alpha = V_s/V_d$ with V_s being the acoustic shear velocity, and J_m being the m^{th}

order Bessel functions. On the other hand, the small side peaks arise due to the $TR_{2,m}$ modes. These modes not only perturb the refractive index, but also take part in the birefringence of the fibers. The cut-off frequencies for these modes are determined by [13]

$$f_{0,m} = \eta_m V s/(2\pi a) \tag{2.56}$$

where in this case, η_m is the m^{th} order solution to the equation

$$\begin{vmatrix} \left(3 - \frac{\eta^2}{2}\right) J_2(\alpha\eta) & \left(6 - \frac{\eta^2}{2}\right) J_2(\eta) - 3\eta J_3(\eta) \\ J_2(\alpha\eta) - \alpha\eta J_3(\alpha\eta) & \left(2 - \frac{\eta^2}{2}\right) J_2(\eta) + 3\eta J_3(\eta) \end{vmatrix} = 0 \tag{2.57}$$

For SMF28, with $V_s = 3740$ m/s, $V_d = 5996$ m/s and $a = 62.5$ μm, the first 5 $R_{0,m}$ frequencies are 30.51 MHz, 82.04 MHz, 130.72 MHz, 179.00 MHz and 227.15 MHz, and the first 3 $TR_{2,m}$ frequencies are 22.32 MHz, 39.46 MHz and 70.72 MHz, which are in very good agreement with the peaks that were calculated in figure 2.6.(a). These results of simulations for the SMF28 are in good agreement with the theoretical and experimental values that have been derived from literature, which allows us to study the electrostrictive properties for the Hybrid Chalcogenide-PMMA microtapers and compare them with the experimental results.

Chapter 3

Fabrication of As_2Se_3-PMMA Tapers

This chapter describes the fabrication of hybrid chalcogenide-polymer microwire composed of an As_2Se_3 core and a PMMA cladding as proposed in [30] using the heat brush approach [29]. Here, I will demonstrate the steps necessary to first prepare the As_2Se_3 fiber and PMMA tubes, followed by the preparation of PMMA microtubes, fusing of the two materials, and drawing of the fiber to its desired diameter. I will finally describe the polishing and coupling of the sample.

3.1 Preparation of the Chalcogenide Fiber and Polymer Tubes

3.1.1 As_2Se_3 Fiber

I first begin with a commercial Coractive IR-SE-100 As_2Se_3 fiber, which consists of typical refractive index of 2.7. For preparation, 7 cm samples of the Coractive fiber are cut and placed in an oven of temperature 150°C for 2 hours inside a metal tube. This is done in order to partially straighten the fiber sample from the coil. Next, the heated sample is immersed in an acetone solution for at least a day in order to loosen and dissolve the polymer coating on the fiber provided by the manufacturer. If not

completely dissolved, one can use a custom fiber stripper to aid with the removal of the polymer coating.

3.1.2 Polymer Tubes

The PMMA tubes provided from the industry have a inner diameter of 5 mm, and an outer diameter of 9.5 mm. These tubes inherently possess internal stresses during fabrication, which remain as dormant forces. In addition to these stresses, PMMA has a tendency of absorbing water from its surrounding due to its porous nature. Upon reheating such a tube to its softened state, the tube will suffer from severe deformations due to the combination the dormant forces, as well as the formation of bubbles that arise from the evaporation of the water.

In order to prevent such deformations, the polymer tube is first dried by keeping it for several days in an oven at a temperature of 80°C before being heat softened at 190°C. Following this drying process, the tube is annealed by suspending the tube vertically inside an oven heated at 150°C with a dead weight pulling the fiber from the bottom. This process ensures that the polymer is free of all the internal stresses that were frozen during manufacturing, and is now able to freeze at its relaxed state.

3.2 Drawing PMMA Microtubes

Before we can begin fusing the As_2Se_3 fiber with the PMMA, an intermediate step of creating PMMA microtubes is required in order to create a support mechanism to hold the As_2Se_3 fibers in place during the fusing process. In this process, the PMMA preform is slowly inserted at constant velocity into a electrical resistive crucible that heats the preform to a softening point at 210°C, while the microwire is drawn at a higher velocity from the other side of the furnace. This causes the soft part to elongate and a microtube with a scaled down cross-section pattern is formed. The schematics used for drawing the microtube is shown in Figure 3.1. The setup consists of two motorized translation stages and a resistive heater attached to the crucible.

The temperature of the crucible is controlled with a temperature controller with the thermocouple set in direct contact with the crucible.

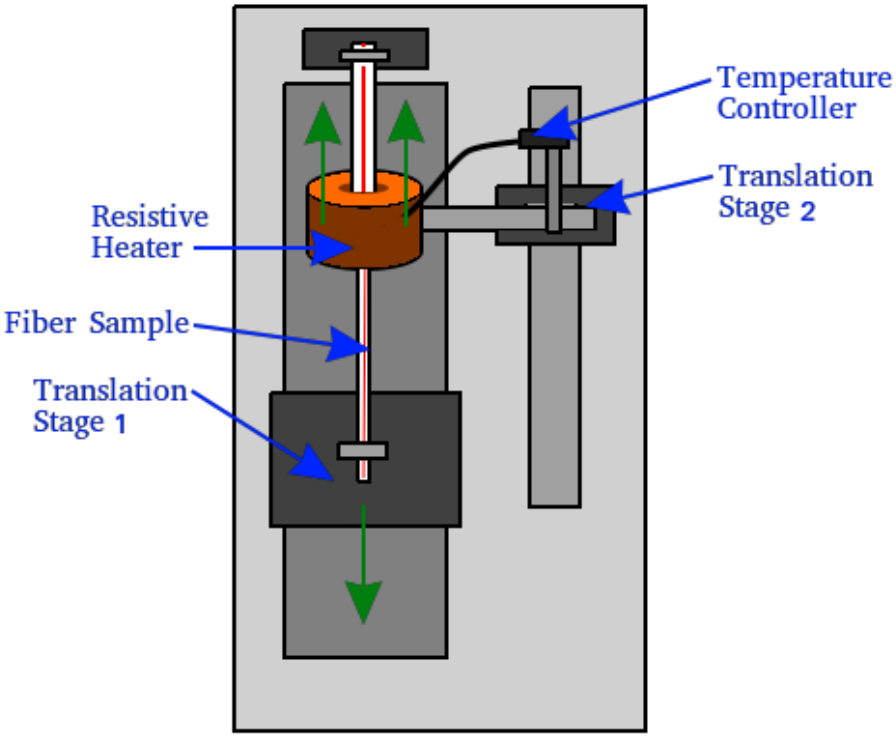

Figure 3.1: Schematic for drawing microtubes and microtapers. Translation stages 1 and 2 are moving at velocities v_d and v_f respectively, so that the draw ratio for the fiber sample $r_m/r_p = \sqrt{v_f/v_d + v_f}$

The ratio of the microtube diameter and the initial tube diameter is given by

$$r_m/r_p = \sqrt{\frac{v_f}{v_d + v_f}} \tag{3.1}$$

where r_m and r_p are the radii of the PMMA microtube and the preform respectively, v_f is the velocity of the preform fed into the crucible, and v_d is the velocity at which the microtube is drawn out. For our case, we desired the ratio r_m/r_p to be 0.3, as this would create a microtube small enough to fit the PMMA preform as needed for the fusing process. The drawing velocity v_d was taken to be 182 μm/s and v_f was adjusted to 18 μm/s. These slow velocities were necessary to ensure that the

PMMA was always in the softened state before drawing, and also to make sure that the crucible was never in direct contact with the PMMA itself.

3.3 Fusing of the PMMA onto the As_2Se_3 Fiber

Fusing of the As_2Se_3 preform, the PMMA preform, and the PMMA microtube is done using a rod-in-tube method. As shown in Figure 3.2, the As_2Se_3 fiber is first inserted into the PMMA microtube, which is then inserted into the PMMA preform. The assembly is mounted horizontally on a lathe that is in rotation at a rate of 3 rotation/min. This PMMA assembly is softened using an electric resistive heater at a temperature of 210 °C, which is moving back and forth along the PMMA tube at a velocity of 1 μm/s. With the aid of gravity and surface tension, over time, the PMMA preform begins to collapse onto the PMMA microtube, and then the microtube begins to collapse onto the As_2Se_3 fiber. The fusing process is done using such slow velocities to ensure that the PMMA is softened thoroughly during the collapse and that no air bubbles are trapped during the process. Complete fusion between the two materials is achieved in 10 hours.

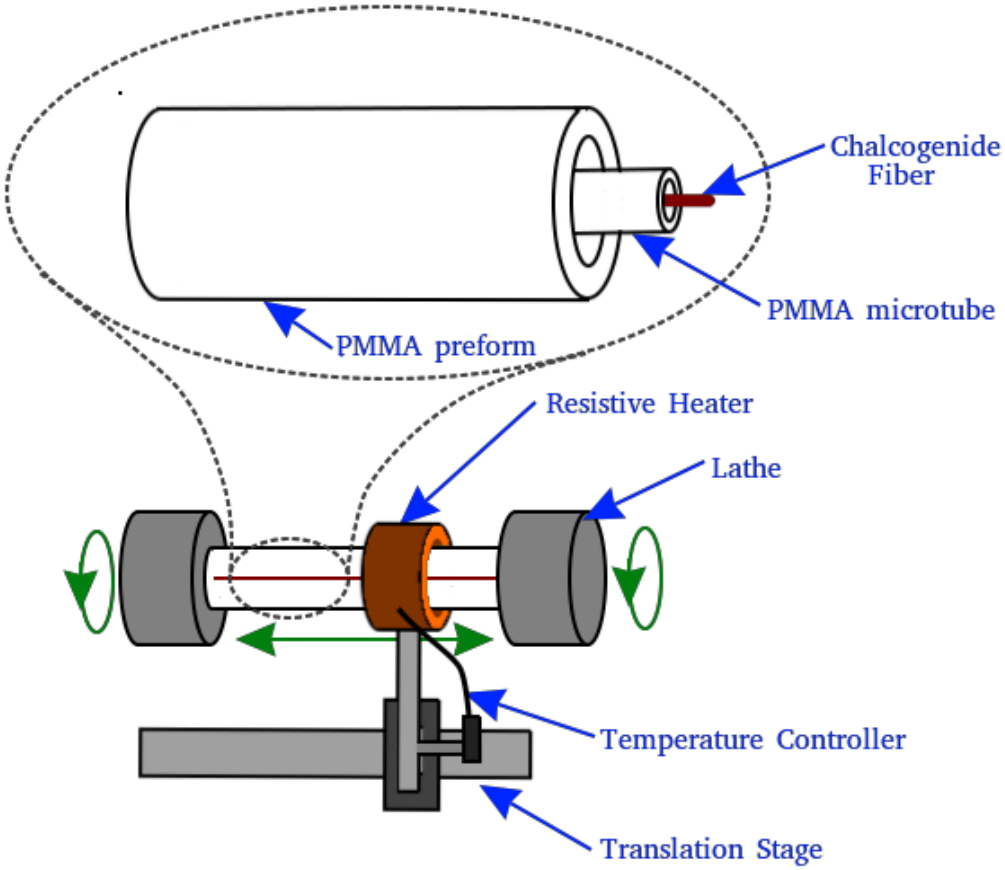

Figure 3.2: Schematic for fusing the PMMA with the Chalcogenide fiber.

3.4 Drawing of the Hybrid As_2Se_3-PMMA Preform

The As_2Se_3-PMMA preform is drawn using the same procedure as discussed in section 3.2. However, in order to maximize the coupling efficiency between the fundamental mode of the standard single-mode silica fiber, we require the core diameter of the fused As_2Se_3 to be around 12 μm, and the cladding diameter to be around 21.25 μm. This can be achieved by scaling down the diameter of the preform by a factor of 0.125. This significantly small ratio of $r_m/r_p = 0.125$ can be obtained by a two stage tapering process to ensure that the hybrid preform is thoroughly softened before the drawing is conducted. We first draw the preform to a ratio of 0.3, using the same

velocities as mentioned in section 3.2. We then draw this sample again to a ratio of 0.42, which is achieved by setting $v_d = 164.72$ μm/s and $v_f = 35.28$ μm/s. At this point, the PMMA has a diameter of 1.2 mm, and is strong enough to allow handling, polishing and coupling with silica fibers without damage.

3.5 Polishing

The polishing apparatus, as shown in Fig. 3.3, consists of a rotating polishing stage with a groove to hold a disk surface, and a fiber holder to hold the fiber perpendicular or at a certain angle to the polishing disc surface. The fiber holder is placed on a translation stage that is provided to allow the fiber tip to approach the rotating disk below. Polishing paper of various particle sizes are glued to a disk surface, allowing one to polish the same fiber tip several times with different polishing papers to achieve superfine polishing fiber tips that are adaquate for optical coupling between two different waveguides. The polishing process is performed for six stages in which polishing paper with particle sizes of 30 μm, 9 μm, 3 μm, 1 μm, 0.5 μm and 0.1 μm are used. A digital camera is placed in line with the disk surface and the fiber to monitor the entire process. Figure 3.4 shows the final polished end of the hybrid fiber with the fused As_2Se_3 core surrounded by the PMMA cladding.

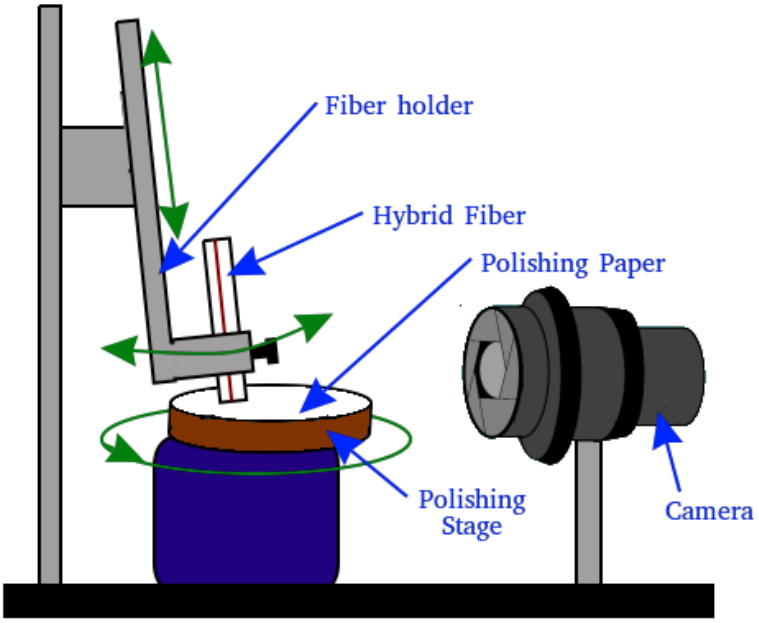

Figure 3.3: Schematic for polishing the hybrid fiber at arbitrary angles.

Figure 3.4: Cross-sectional view of the chalcogenide core (21.25 μm diameter) surrounded by PMMA cladding (1100 μm diameter) after polishing the surface.

3.6 Coupling

In order to ensure that there are no Fresnel reflections between the silica single-mode fiber and the Chalcogenide-PMMA, we took the approach of using a custom angle-cleaved coupling procedure. The elimination of the Fresnel reflection assures that no

Fabry-Perot cavities are created, and light is only allowed to pass once through the medium. This becomes important in the presence of nonlinear gain mechanisms, such as SBS, as any sort of back-reflection can possibly lead to lasing.

The angled coupling between a standard silica SMF and our hybrid Chalcogenide-PMMA microwires was achieved in a three-stage process. The apparatus to couple consists mainly of two alignment stages, an IR camera, a microscope, and a UV lamp, as shown in Figure 3.5. The signal from the IR camera is connected to a screen to monitor the alignment, and is simultaneously transmitted onto a data-acquisition card to plot the cross-section and measure the peak power of the beam profile passing through the fiber.

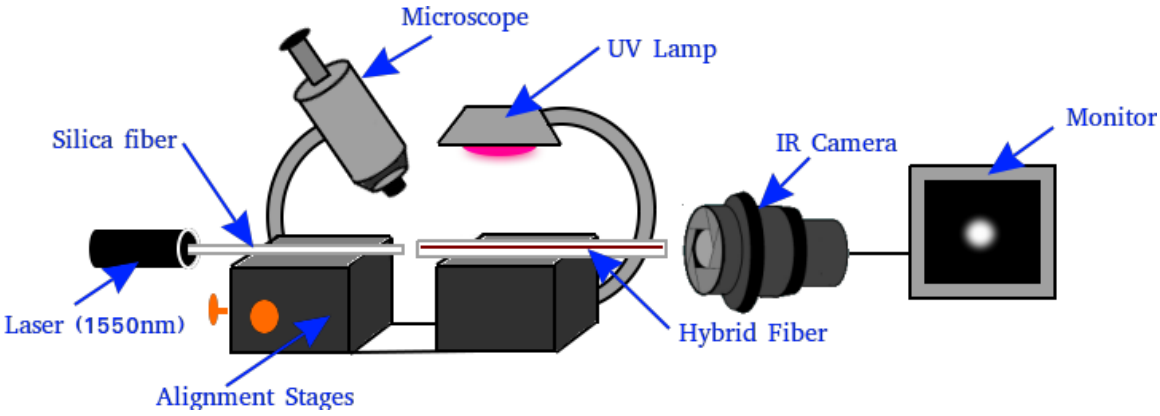

Figure 3.5: Schematic for coupling a standard silica fiber with the hybrid fiber.

In the first stage, the SMF and the hybrid fiber are flat polished (i.e. the polished surface is perpendicular to the axis of propagation), and are aligned using the alignment stage in order to launch light at $\lambda = 1550$ nm from an SMF into the core of the hybrid fiber. The output end of the fiber is observed using an infrared camera, and further fine-tuning of the alignment stage is performed to maximize the power measured at the power meter. Finally, UV-cured epoxy is then used to permanently fix the input end of the hybrid fiber to the launching SMF. During the curing process, the hybrid fiber must be covered to avoid the UV exposure because the UV destroys the PMMA polymeric structure, making it unfeasible to taper to smaller diameters. At this point, we have achieved the optimal coupling into and out of the hybrid fiber

using just the flat polished surface, and is used as a reference to further optimize the coupling using angle-polished surfaces.

The second stage of coupling is quite similar to first stage, except this time, the SMF is angle-polished at 10°, while the hybrid fiber is angle-polished at 5°. These angles were derived simply using the Snell's law of refraction for light passing from glass to chalcogenide. This technique works as a really good approximation to ensure that the transmission between the glass and chalcogenide interface is closely aligned to the fundamental mode of the cylindrical waveguide, while the angle of the reflected light is much larger than the critical angle for either waveguide, preventing it from total internal reflection. Alignment for this angled-polished fiber was conducted on a second alignment stage with a custom design that allowed one of the fibers to be tilted away from the principal axis of the alignment stage. Also, this time, since the first end of the hybrid fiber was already coupled to the SMF, we determined the optimal alignment by simply measuring the optical power that was accumulated into the SMF using a power meter.

The third stage of coupling required us to break the first flat-coupled SMF-Chalcogenide port, and couple the same ends again using the angled-coupling mechanism as done in the second stage. With the most optimal configuration, such a coupling process allows one to achieve a single-pass transmission loss of only 2 dB, while simultaneously providing a back-reflection loss of at least 40 dB, making it an ideal configuration for coupling two fibers for a single-pass transmission.

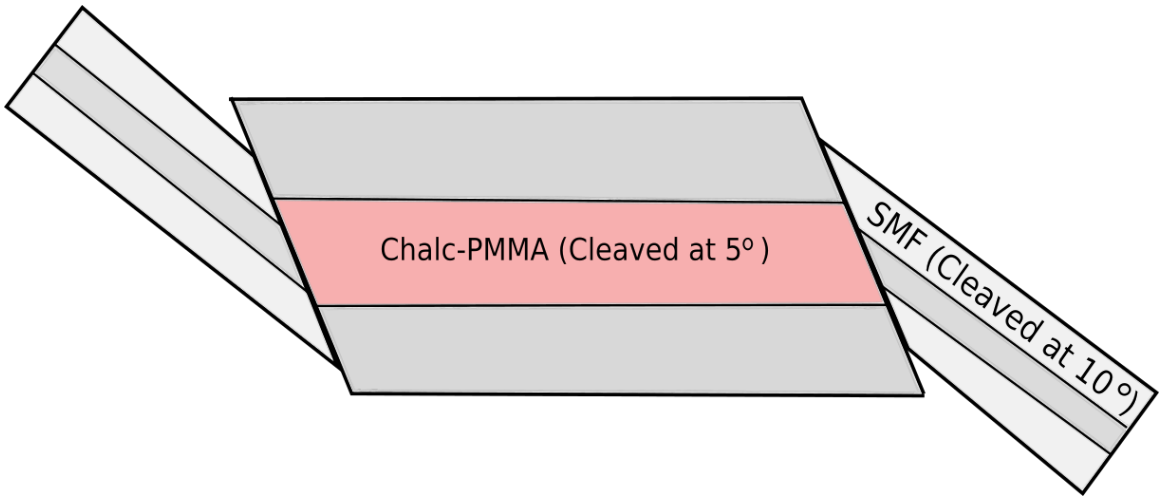

Figure 3.6: Final configuration for an angle-coupled Single mode fiber (SMF) and Chalcogenide-PMMA hybrid fiber (angles not drawn to scale)

3.7 Microwire Fabrication

Once the hybrid fiber is coupled with the SMF from both ends, we move forward with the fabrication of a hybrid microtaper. Figure 3.7 is a schematic for a hybrid microtaper. It comprises a waist where most of the nonlinear effects occur, and a transition region between the hybrid fiber and the microwire section. The tapering apparatus to achieve these microtapers is exactly the same as described during the fabrication of the preform in sections 3.2 and 3.4. However, unlike before, the drawing technique requires a very precise control for each motorised stage in order to ensure that the taper fabrication is done under adiabatic conditions. A fiber taper is considered adiabatic when the system transition region eliminates loss in power of the fundamental mode propagating in the microtaper.

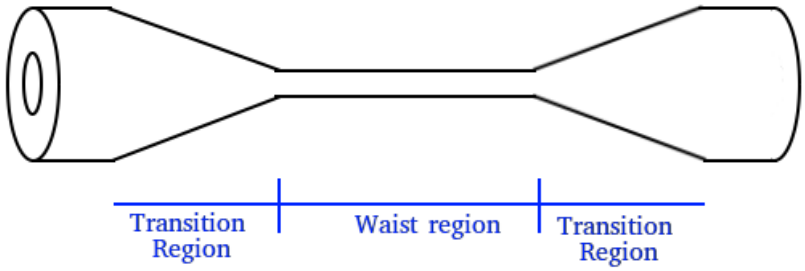

Figure 3.7: Schematic of a microtaper with a uniform waist and two similar transition regions

As discussed in [98], loss in power of the fundamental mode in microtapers can arise due to two main reasons: 1) Breaking down of the total internal reflection criteria between the core and the cladding, 2) Transfer of power between the fundamental mode HE_{11} to the higher order modes with the same symmetry, mainly HE_{12}. In step-index fibers, both criteria are automatically eliminated if the following criterion is satisfied along the direction of propagation z:

$$|\frac{\mathrm{d}\phi_{clad}}{\mathrm{d}z}| = \frac{\phi_{clad}}{2\pi}(\beta_{11} - \beta_{12}) \tag{3.2}$$

where ϕ_{clad} is the diameter of the cladding, and β_{11} and β_{12} are the propagation constant for the HE_{11} and HE_{12} modes respectively.

The precise control of the cladding diameter was achieved through tapering the fiber over multiple sweeps of the heater. Given a specific microtaper profile, a MATLAB code generated the set of files containing information describing each tapering sweep as described in [30, 98]. This file was then loaded onto a LabVIEW interface, which used the set of parameters from the file to control the motorized translation stages and fabricate the microtaper with the prescribed profile. For our case, the microtaper consists of a 60 cm long microtaper region, and an adiabatic transition region of 10cm on either side of the microtaper.

Chapter 4

SBS in Single-Core As_2Se_3-PMMA Microtapers

In this chapter, I compare the numerical as well as the experimental results for SBS within a single-core As_2Se_3-PMMA microtaper. I first discuss the numerical results for the electromagnetic field, and its impact on the Brillouin spectrum when used as a source of electrostriction in the elastodynamics model mentioned in section 2.3.1. Then, I focus on measuring SBS for the microtaper with two coherent optical waves through Brillouin optical time-domain analysis (BOTDA) using a range of optical pump pulse widths. Finally, I demonstrate the agreement between the numerical, and the experimental results for SBS for such microtapers in both the Pump-Stokes configuration, as well as the pump-Anti-Stokes configuration for the BOTDA setup.

4.1 Electromangetic Field in Chalcogenide-PMMA microtapers

Contrary to the weakly-guided mode in SMF28, the large refractive index difference between the PMMA cladding and the chalcogenide core in the hybrid microtaper forces the optical field to be ultra-confined within the 1 μm chalcogenide core. Also, the E_z component for such waveguides is non-negligible as compared to the tangential

components E_x and E_y. This would have resulted in discontinuities and inaccuracies had the solution been derived using either the weakly-guided approximations or the scalar-field approximation. The variation in the results compared to the weakly-guided SMF28 suggests that the vectorial approach to the Finite Element simulations is definitely the ideal choice for deriving Maxwell's equations for any arbitrary waveguide.

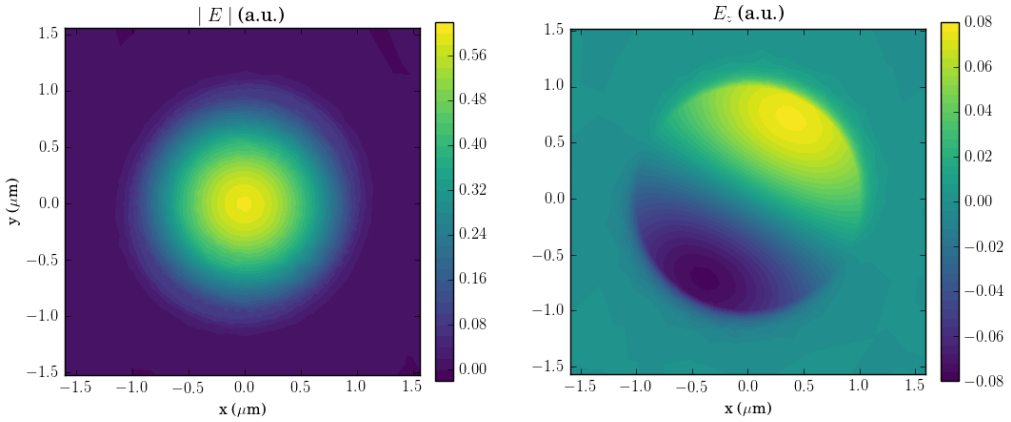

Figure 4.1: Spatial distribution of the (*left*) magnitude and the (*right*) z component of mode HE_{11} in Chalcogenide-PMMA microtaper.

In order to confirm the accuracy of the simulation we compare the calculated effective refractive index $n_{eff} = \beta/k$ of the fundamental mode with the exact value derived using Eq. (2.2). The result are shown in Table 4.1.

Fiber	$\mathbf{n}_{core}$	$\mathbf{n}_{clad}$	$\mathbf{n}_{eff}^{(exact)}$	$\mathbf{n}_{eff}^{(FEM)}$	**error** $= \dfrac{\mid n_{eff}^{(exact)} - n_{eff}^{(FEM)} \mid}{n_{core} - n_{clad}}$
SMF28	1.4492	1.4440	1.4461	1.4462	0.019
As_2Se_3-PMMA	1.481	2.674	2.6554	2.6155	0.033

Table 4.1: Theoretical vs. numerical results for the effective refractive index within silica and Chalcogenide-PMMA tapers

We can see that the values of n_{eff}^{FEM} that were calculated numerically are in close agreement with the theoretical values n_{eff}^{exact} derived using the characteristic equation

with only $\approx 3\%$ error w.r.t. the range n_{eff} can take between n_{core} and n_{clad}.

4.2 Results for SBS in Microtapers using Electrostriction Model

Here, I show the calculation of the backward ($k = 2k_1$) electrostriction spectra for the chalcogenide microtaper as shown in Fig. 4.2. These spectra have been obtained by evaluating the kinetic energy of the acoustic beam (i.e. $\omega^2 \int_S \rho \mid u_i \mid^2$) as a function of the detuning frequency between the two optical fields.

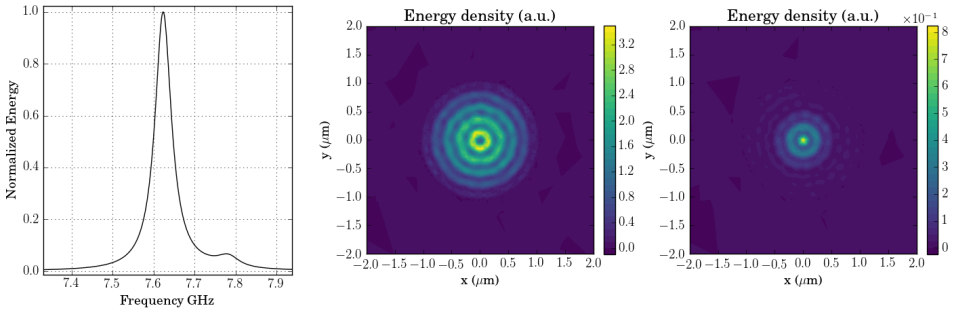

Figure 4.2: (*left*) Numerical results of the energy spectra for a 2 micron Chalcogenide-PMMA microtaper. (*middle,right*) Energy distribution over the cross-section of the hybrid microtaper for a frequency detuning of 7.622 GHz and 7.76 GHz of the two optical fields

Unlike for the case in SMF28, such a fiber gives rise to multiple acoustic modes. Using the acoustic and optical parameters for both the chalcogenide core and the PMMA cladding given in [28, 105], the resulting spectra show two dominant peaks at 7.622 GHz and 7.76 GHz.. The main peak is at 7.622 GHz detuning frequency with a FWHM of 38 MHz. This bandwidth indicates that most of the acoustics are confined in the chalcogenide core, which has a bandwidth with a FWHM of 13.2 MHz, and not suppressed by the PMMA cladding, which has a bandwidth 120 MHz [27]. This is confirmed by the acoustic energy distribution for both acoustic modes shown in Fig. 4.2, as most of the acoustics are contained within the chalcogenide core, and aren't

protruding into the PMMA cladding. This happens by a combination of the acoustic impedance mismatch between core and cladding ($Z = \sqrt{E(1-\nu)\rho/(1+\nu)(1+2\nu)}$) and the optical force. The rippling behaviour in the acoustics energy density is a consequence of the interference between the transverse and the longitudinal acoustic modes that are both generated in this microtaper, unlike the purely longitudinal mode that is dominant in SMF28. The generation for both longitudinal and transverse acoustic modes are again a consequence of the acoustic impedance and the ultra-confinement of the electric field inside the core (leading to non-zero axial contributions of the electric field).

4.3 Brillouin Optical Time Domain Analysis

BOTDA is a distributed optical fiber sensing mechanism that exploits the SBS process formed by two counter-propagating waves in order to determine the change in the refractive index of the fiber due to strain or temperature fluctuations along the fiber [7–9]. This two-wave mechanism is quite unique when compared to most passive distributed sensing mechanisms, such as Optical Time-Domain Reflectometry (OTDR) and Brillouin Optical Time-Domain Reflectometry (BOTDR) that only shine light through one side of the fiber, as the two-wave interaction allows the generation of a stimulated scattering for sensing purposes, while the other one-wave processes rely on the spontaneous scattering that are produced intrinsically from the fiber.

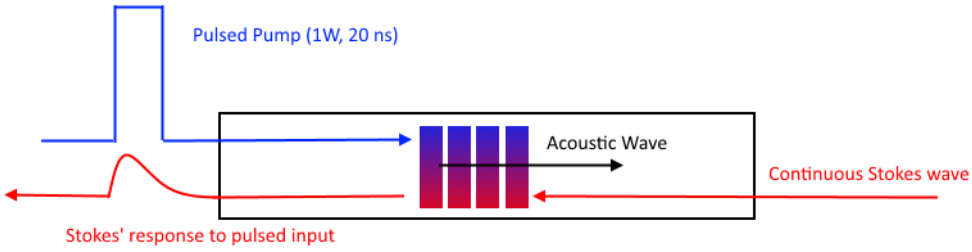

Figure 4.3: Visual representation of the BOTDA sensing mechanism.

A pump pulse light and a continuous wave probe, injected at the two ends of the fiber, are required to generate SBS, as shown in Fig. 4.3. When two counter-propagating waves that are separated by the Brillouin frequency are launched at the two ends of the fiber, they interact with each other, resulting in the transfer of energy from the pump wave to the down-shifted Stokes wave through the interaction with localized phonons. This leads to an amplification of the Stokes wave, which is measured as an impulse response to the incoming pulsed pump wave.

Although known practically for optical fiber sensing, in my case, however, BOTDA was implemented to make sure that high pump peak powers were achieved without the deterioration of the microtaper through Two-Photon Absorption (TPA) near the 1550 nm range [57, 107], as well as to prevent damage at the chalcogenide-silica coupling interface due to residual cured epoxy used for coupling, as described in section 3.6. These deteriations are clearly noticed when the system is introduced to high power continuous wave pump waves, thus restricting us to work with an pulsed pump.

However, pulse widths are still kept longer than the entire length of the fiber, as we require a quasi-continuous wave SBS behavior between the pump and the Stokes, and are not interested in the transient effects for either of the optical fields. By conducting BOTDA with a quasi-continuous pulse, we will be able to retrieve a continuous-wave SBS gain profile of the chalcogenide microtaper that is partially convolved by the broad bandwidth of the pulse. This result can then be compared with the numerical gain spectrum that assumes a continuous wave by artificially convolving the spectrum with the broadened spectrum of the pulse, giving us an adequate description of the electrostrictive properties of the chalcogenide microwire. Hence, by tuning the pulse width and the pump peak power, we can find a balance between the lowest pump linewidth and the power damage threshold to adaquetly represent a quasi-continuous wave SBS process in the microtaper.

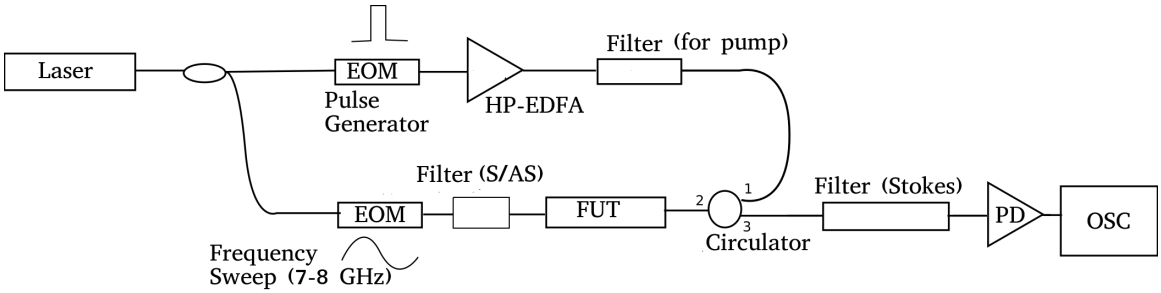

Figure 4.4: BOTDA setup for hybrid fiber microtapers. EOM: Electro-Optic Modulator. HP-EDFA: High-Power Erbium-Doped-Fiber-Amplifier. FUT: Fiber Under Test. PD: Photo-Diode. OSC: OSCilloscope.

The apparatus for measuring the BOTDA spectrum for our hybrid fiber microtapers is shown in the Fig. 4.4. In this setup, the pump signal is kept at the same frequency, while the Stokes is tuned between 7 GHz to 8 GHz away from the pump frequency. A sample trace of the amplified Stokes wave as a function of time and detuning frequency is shown in Fig. 4.5. The contour represents the time-varying gain profile for the detuned Stokes wave as an input pump pulse with period of 10 ns passes through the 60 cm hybrid microtaper (which corresponds to $\sim$7 ns time delay). The gain profile is clearly longer than the length of the fiber. This is because the gain first ramps up as the pulse enters the fiber. Then, when the pulse fully covers the entire fiber length, quasi-CW interaction between the pulse and the fiber take place, thus providing the optimal gain that can be derived from the microtaper. Lastly, as the pulse exits the fiber, a delayed impulse response follows as the phonons slowly get depleted inside the microtaper.

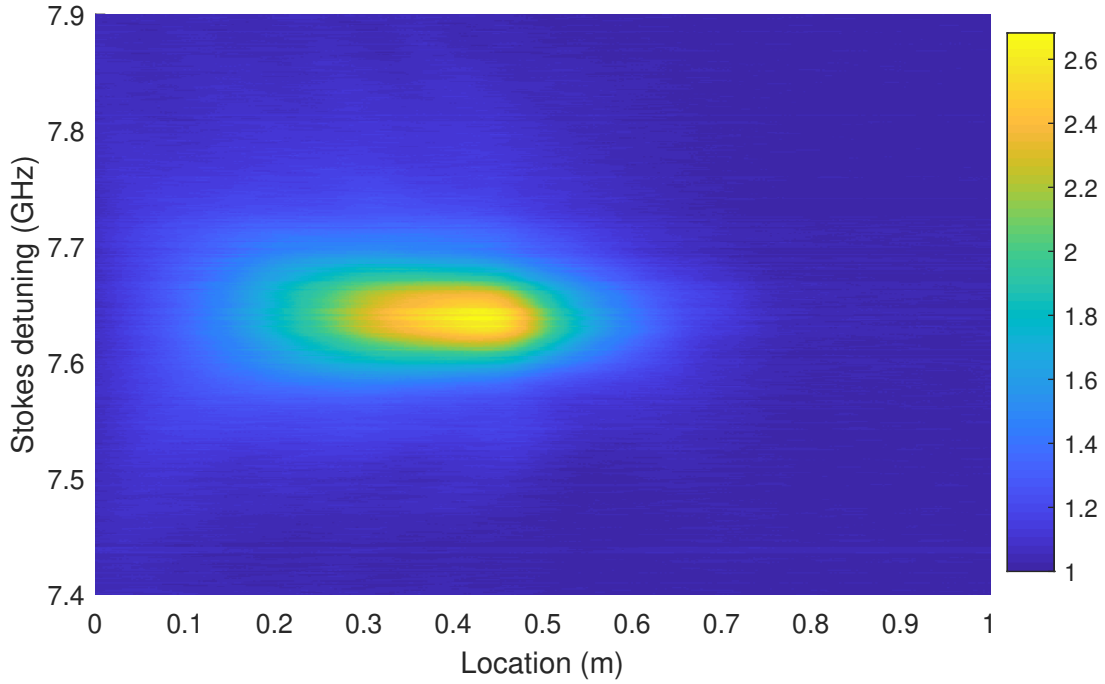

Figure 4.5: Sample trace for a BOTDA system. The contour represents the gain profile for the Stokes wave in dB.

4.4 BOTDA Traces from the Pump-Stokes Configuration for Different Pump Pulse Widths

BOTDA traces for the Stokes wave in a Pump-Stokes configuration with three different pump pulse widths of 10 ns, 17 ns and 20 ns are shown in Fig. 4.6. Two features about the BOTDA traces become apparent as the pulse width is increased. Firstly, the bandwidth of the Brillouin Spectrum gets narrower. This mainly occurs due to narrowing of the pulsed pump bandwidth, hence reducing the convoluted representation of the true SBS profile for the hybrid microtaper. Secondly, as the pulse is kept longer inside the medium, larger number of phonons are produced until the entire fiber approaches saturation, allowing us to acquire maximum Brillouin gain from the fiber. Both these effects result in a narrower and sharper Brillouin gain profile as the pump pulse width is increased. Lower Brillouin gain for the 20 ns pulse, however, is

an artifact arising from the two-photon absorption of the 1550 nm pump laser that deteriorates the performance of the fiber after being exposed with high powers for too long, even though the narrower Brillouin gain bandwidth suggests a stronger Brillouin amplification.

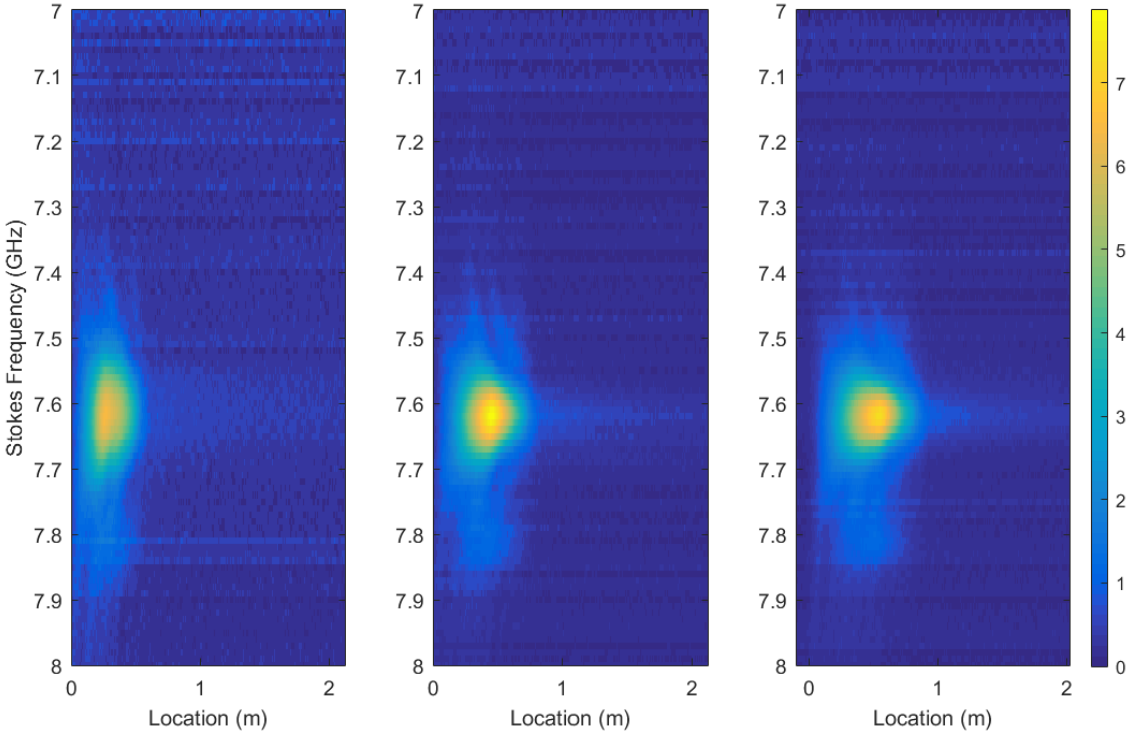

Figure 4.6: BOTDA traces for the Stokes wave in a 60 cm hybrid microtaper with input pulsed pump with peak power of 9 dBm and pulse width of 10 ns (left), 17 ns (middle) and 20 ns (right). The contour represents the signal power $\frac{|\ A_0 + a_s(\omega, t)\ |^2}{|\ A_0\ |^2}$ where A_0 is the continuous wave amplitude and a_s is the small varying resulting from Brillouin gain. Contour units are in dB scale.

Figure 4.7 shows the evolution of the Stokes spectrum as a function of the pump peak power with two different pulse widths. In either case, we see two peaks, one at 7.62 GHz, and the other at 7.8 GHz, that arise from the interaction of the pump with the Stokes wave through SBS. In comparison to what is seen in Fig. 4.6, the doubling of the pulse width effectively narrows down the Stokes spectrum, and enhances the Stokes signal by a factor of $\sim$2 dB, suggesting that as the pump pulse width is extended, the sample is induced to a quasi-CW SBS process. A schematic for both

the processes is shown in Fig. 4.8. When the Stokes is detuned by either the 7.62 GHz or the 7.8 GHz, there is an effective power transfer from the pump to the individual Stokes wave through the means of SBS that arises from the electrostriction, thus giving rise to acoustic waves that resonate with a frequency of 7.62 GHz or 7.8 GHz respectively. In case of such an SBS process, the acoustic waves formed are travelling in the direction of the pump wave, and the back-scattered field becomes a seed for the amplification of the Stokes wave.

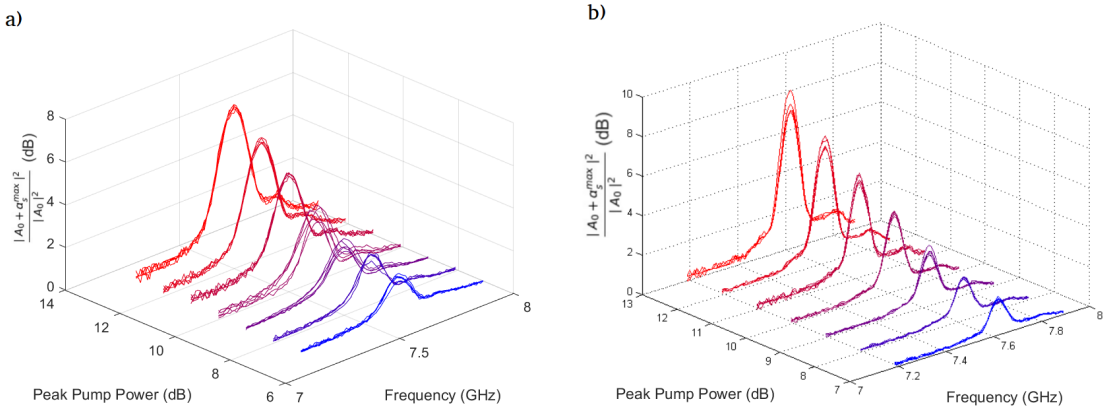

Figure 4.7: Evolution of the Stokes gain profile for the hybrid microtaper as a function of peak power of a) 10 ns and b) 20 ns pulsed pump. Frequency domain traces are derived from a single time slice of the BOTDA traces where the Brillouin gain is maximum. Traces for each peak power were repeated 5 times. A_0 is the continuous wave amplitude and a_s is the small varying signal resulting from Brillouin gain. Contour units are in dB scale.

Figure 4.9 shows the Stokes gain (dB) as a function of the input pump peak power (dBm). A clear competition for SBS gain between the 7.62 GHz peak and 7.8 GHz peak is observed as the pump power is increased. Since the SBS process at 7.62 GHz is the dominating process inside the SBS fiber, the Stokes gain stays relatively constant with respect the pump power, as most of the power from the pump is transferred to this Brillouin peak. On the other hand, the SBS process for 7.8 GHz Brillouin peak is relatively weak, and is effectively saturated since most of the power gets transferred to the 7.62 GHz peak. This is why we see a decline in the 7.8 GHz Stokes gain, as

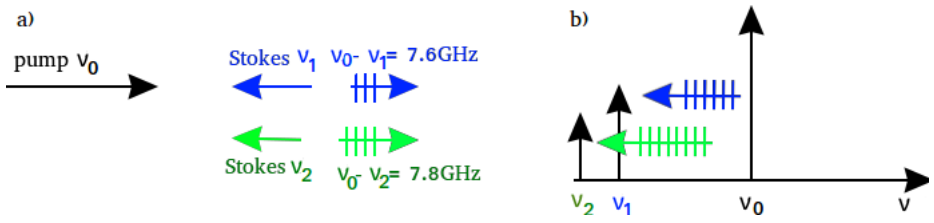

Figure 4.8: a) Schematic of the SBS occurring between the pump and the Stokes wave when the Stokes wave is detuned to 7.62 GHz and 7.8 GHz below pump frequency. Length of arrows represents frequency (not to scale). b) shows the transfer of power from the pump to the Stokes wave through the means of SBS for each case. Frequency is shown on horizontal axis, and length of arrows represents power.

the pump cannot transfer enough energy to the secondary peak.

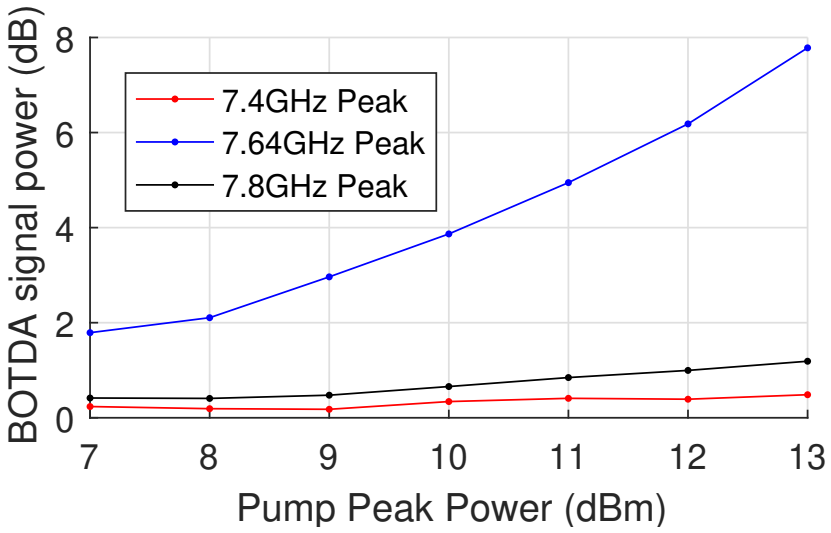

Figure 4.9: Stokes gain represented as the ratio of the Stokes peak power P_{Stokes} with respect to input pump peak Power P_{pump} with pulse width of 20 ns. Traces are plotted in dB scale.

4.5 BOTDA Traces for Pump-Anti-Stokes Configuration

In order to ensure no asymmetric SBS processes in the Pump-Anti-Stokes configuration are occurring with respect to the Pump-Stokes configuration, a BOTDA trace for the loss in the Anti-Stokes in the presence of a pulse pump has been shown in Fig. 4.10. For a high pump peak power of 10dBm, we see a dominant dip in the

Anti-Stokes signal at a frequency detuning of 7.62 GHz. This shows that the pump interacts with the Anti-Stokes through the dominant longitudinal wave that is present during SBS. There are also traces of a secondary dip at the same 7.8 GHz as detected in the Pump-Stokes configuration.

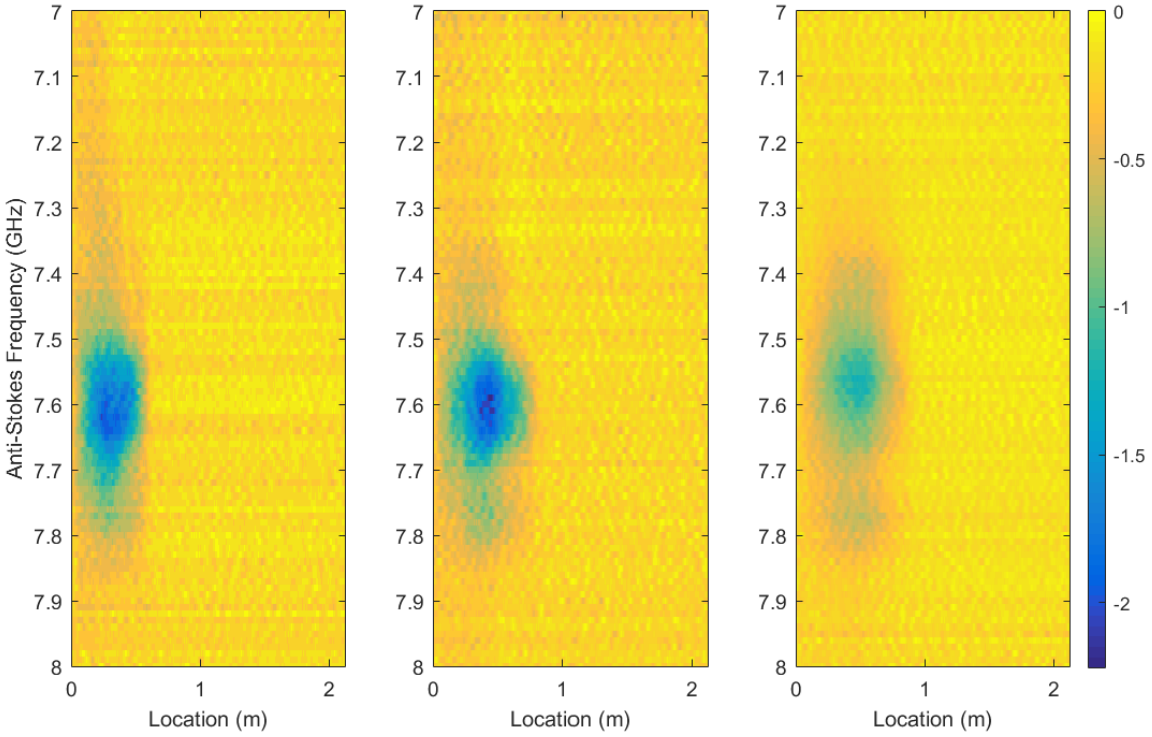

Figure 4.10: BOTDA traces for the Anti-Stokes wave in a hybrid microtaper with input pulsed pump with peak power of 10dBm and pulse width of 10 ns (left), 17 ns (center) and 20 ns (right). The contour represents the loss profile for the Stokes wave in dB.

Figure 4.11 shows the Brillouin spectrum of the Stokes wave in the Pump-Stokes configuration and the Anti-Stokes wave in the Pump-Anti-Stokes Process. In the Pump-Anti-Stokes configuration, we see that the power is transferred from the Anti-Stokes into the pump through the means of a longitudinal acoustic mode, resulting in a net loss in intensity of the Anti-Stokes, and hence a negative value in the dB scale. Also, since the Stokes and the Anti-Stokes are seeded into the sample at a power of -10 dBm each, and the pump wave has a peak power greater than 7 dBm, the energy transfer between the pump and the Stokes is much more efficient than the power transfer between the Anti-Stokes and the pump, as more acoustic waves are generated by the pump than by the Anti-Stokes wave. This is why the net loss in the

Anti-Stokes is not able to match the net amplification in the Stokes wave.

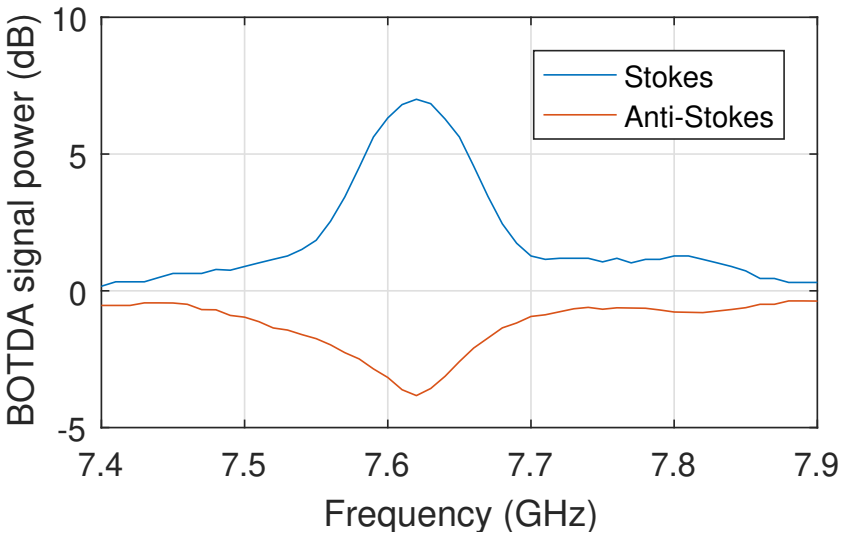

Figure 4.11: Comparison of the spectra between the SBS process between the pump-Stokes configuration and the pump-Anti-Stokes configuration. In both cases, pump peak power was set to 13 dBm with a pulse width of 20 ns, and the Stokes, or, anti-Stokes waves were seeded with a steady power of -10 dBm

Despite the different magnitudes of the gain and loss in the Pump-Stokes and Pump-Anti-Stokes configuration respectively, both the Anti-Stokes and Stokes signals are only excited by the pump wave when the detuning for either waves is set to 7.62 GHz and 7.8 GHz with respect to the pump frequency. This definitely confirms that in fact the pump is interacting with both the Stokes and the Anti-Stokes only through an SBS process with longitudinal acoustic waves that resonate at 7.62 GHz or at 7.8 GHz, and no secondary Brillouin process is being excited in either case.

A schematic for SBS between the pump and the Anti-Stokes is shown in Fig. 4.12. When the Anti-Stokes is detuned by either 7.62 GHz or the 7.8 GHz, there is an effective power transfer from the individual Anti-Stokes wave to the pump through the means of SBS that arises from the electrostriction, hence giving rise to acoustic waves that resonate with a frequency of 7.62 GHz or 7.8 GHz respectively. In the case of such an SBS process, the acoustic waves formed are travelling in the direction of the Anti-Stokes wave, and the back-scattered field is seeded into the pump, which is usually negligible in this case due to the already high peak power.

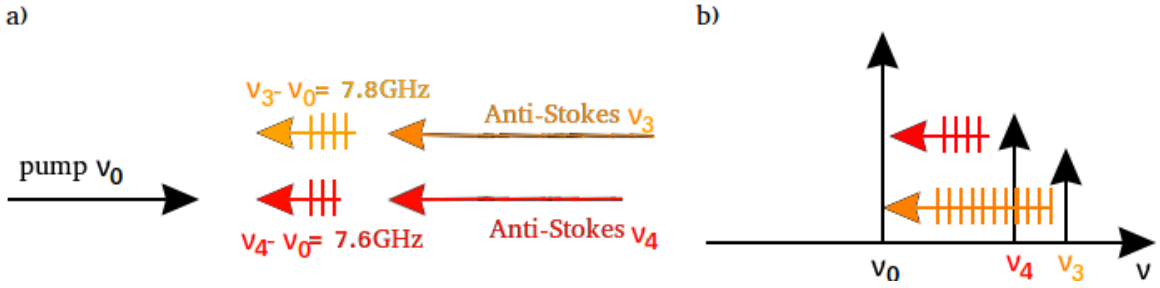

Figure 4.12: a) Schematic of the SBS occurring between the pump and the Stokes wave when the Anti-Stokes wave is detuned to 7.62 GHz and 7.8 GHz above pump frequency. Length of arrows represents frequency (not to scale). b) shows the transfer of power from the pump to the Stokes through the means of SBS for each case. Frequency is shown on horizontal axis, and length of arrows represents power.

4.6 Experimental vs Numerical simulations for SBS in Chalcogenide-PMMA microtaper

In Fig. 4.13, we overlay the Brillouin profile from the BOTDA traces over the simulation results that are derived using the Finite-Element Method for the hybrid microtaper using continuous-wave pump and Stokes fields. Frequency domain traces are derived from a single time slice of the BOTDA traces where the Brillouin peak is maximum.

As seen in the figure, the trend of the measured Brillouin spectra is in agreement to the numerical results, as the main Brillouin peak at 7.62 GHz coincides with the dominant peak in the simulations. The model also demonstrates a secondary peak at around 7.76 GHz, which is in agreement with experimental results at around 7.8 GHz. Uncertainty in the core diameter, which is about 10% results in an uncertainty of 0.05 GHz for our experimental results. This concludes there is no discrepancy between the finite-element method and the experimental results. Also, the broadening of the experimental traces with respect to the numerically derived spectra are the consequence of broadening of the Brillouin gain from a pulsed pump input. This broadening is noticeably reduced as the pulse width is elongated. Ideally, if the optically field is continuous wave, the spectrum should resemble with what is derived numerically, with the theoretical bandwidth of 38 MHz.

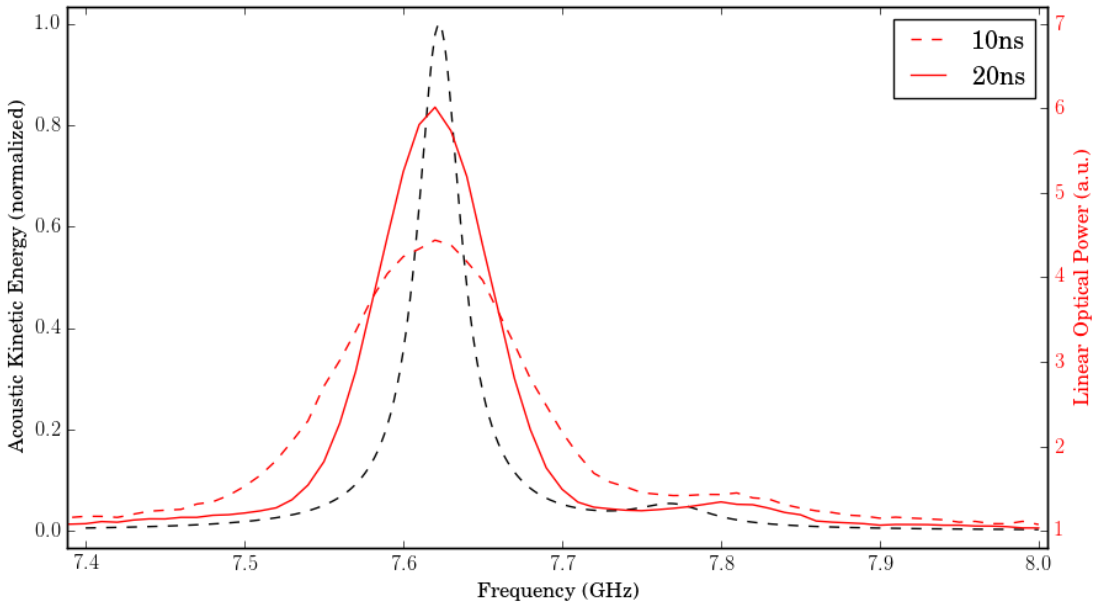

Figure 4.13: (*left*) Overlay of the Linear Optical Power spectra from the BOTDA traces for 10 ns and 20 ns (red) pump pulse widths with the numerical results of the energy spectra for a 2 micron Chalcogenide-PMMA microtaper (black).

Chapter 5

Simultaneous Generation of GAWBS and SBS in Single-Core As_2Se_3-PMMA Microtapers

In this chapter, I demonstrate simultaneous generation of SBS and GAWBS from electrostriction of optical waves in a 60 cm As_2Se_3-PMMA microtaper waveguide. The GAWBS in the microtaper couples with SBS through a complex energy transfer between weak Stokes and Anti-Stokes (AS) continuous waves in the presence of a high power pulsed pump wave, which results in an amplification of the Stokes wave at 7.4 GHz. The additional peak originates due to modulation of the optical fiber by GAWBS at 211 MHz generated by the pump, which interplays with Stokes peaks at 7.62 GHz and 7.8 GHz formed by SBS for a 2 μm As_2Se_3 core radius (as shown in chapter 4). Generation of the GAWBS is also demonstrated experimentally which shows excitation of a high spectral density of transverse waves near the 200 MHz range that are responsible for the distortion of the SBS spectrum.

5.1 Measurements for GAWBS in Chalcogenide-PMMA microtapers

Figure 5.1 shows the experimental setup for observing depolarized guided acoustic wave Brillouin scattering as conducted in [13]. The light source is a fiber laser operating at 1550 nm with an input power of 15 dBm. The beat signal of the GAWBS light and the pump light emitted out of the fiber is detected by a photodetector placed after an analyzer. The polarization of the input and output light is adjusted by the two polarization controllers and a polarizer so as to maximize the resonance peak monitored on a spectrum analyzer. In this case, the fiber under test was a 60 cm-long As_2Se_3-PMMA taper with a core diameter of 2 μm and a cladding of 100 μm.

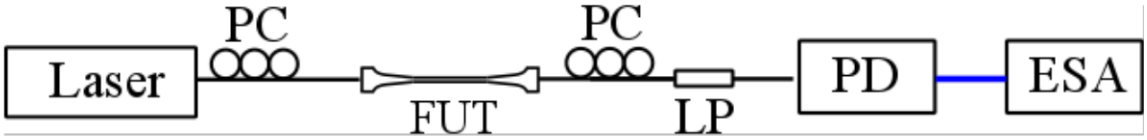

Figure 5.1: Schematic of setup for observing depolarized guided acoustic wave Brillouin scattering. PC, polarization controller; LP, linear polarizer; PD, photodetector; ESA, electrical spectrum analyzer.

5.2 Experimental vs numerical results for GAWBS in chalcogenide-PMMA microtapers

An overlay of the experimental results for the GAWBS spectrum with the numerical simulations for the acoustic energy for two co-propagating waves ($k \approx 0$) is shown in Fig. 5.2. Clearly, there is a dominant peak at around 210 MHz. This suggests that a strong pump laser is able to excite both the longitudinal and transverse acoustic field within the 60 cm microtaper.

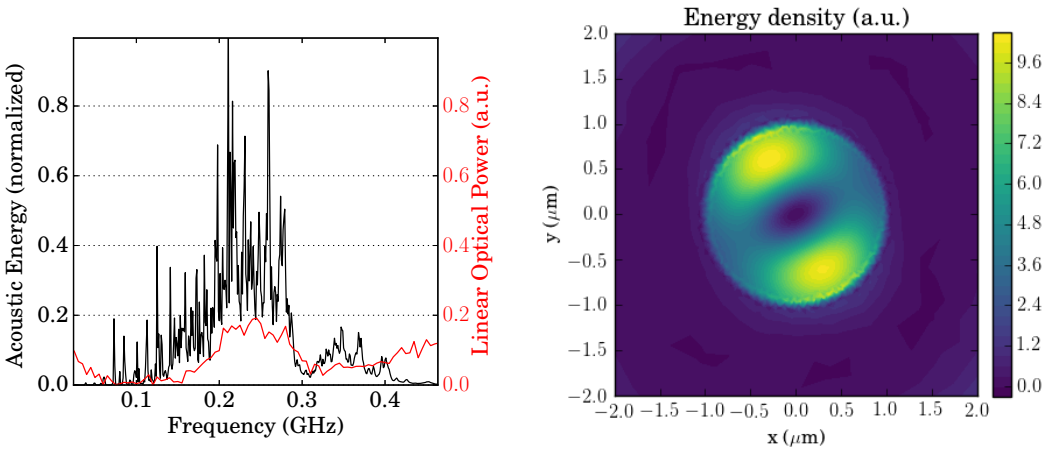

(a) (b)

Figure 5.2: a) Overlay between numerical acoustic kinetic energy spectra (black) and experimental optical power detected by the photodetector(red) for the GAWBS for the Chalcogenide-PMMA microtaper. b) Energy density for a transverse acoustic wave at a frequency of 211 MHz, which correponds to the peak with the highest resonance for the numerical results of the GAWBS spectra.

In case of GAWBS, we notice the energy spectra gradually decreasing with increasing frequency within the same range as derived experimentally, although the resonant peaks do not seem to be accurately predicted. These discrepancies can be explained by the uncertainty in the diameter of a significantly large PMMA cladding, as well as the constant competition between several discrete acoustic modes (as shown by the simulation) that are competing for the same energy from the pump source, all leading to a direct influence on the transverse acoustic resonances. Nevertheless, both the experimental results and the numerical simulations have been able to demonstrate an electrostriction spectrum that is occurring in the frequency range that will aid in the amplification of the Stokes wave for a three-wave BOTDA experiment.

The acoustic energy distribution for the peak at 211 MHz indicates a torsional-radial mode that is radially asymmetric. Because of the mismatch in the acoustic impedance between the core and the cladding, and the high confinement of the electric field, the acoustics are still dominant within the chalcogenide core. However, unlike the case for SBS, there is a non-zero component of the displacement vector that is

now present in the PMMA.

5.3 BOTDA Results for Pump-Stokes-Anti-Stokes Configuration

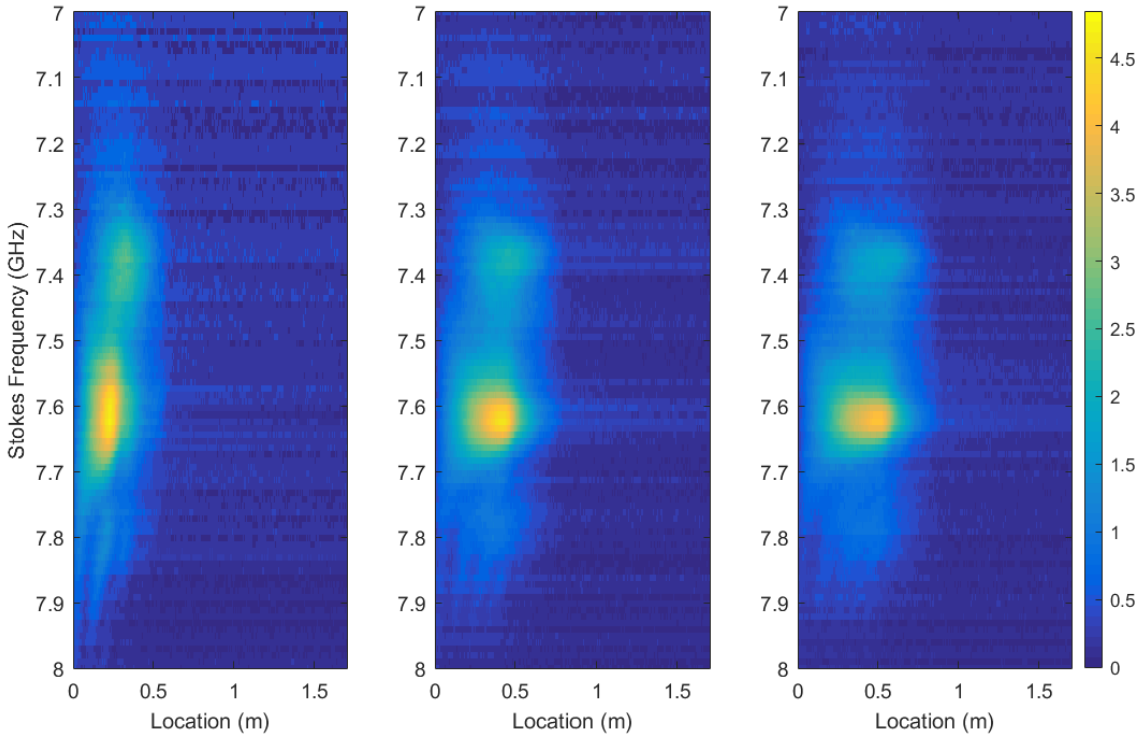

Figure 5.3: BOTDA traces for the Stokes wave in a hybrid microtaper with input pulsed pump with peak power of 10 dBm and pulse width of 10 ns (left), 17 ns (center) and 20 ns (right). The contour represents the gain profile for the Stokes wave in dB.

BOTDA traces for the Stokes wave in a Pump-Stokes-Anti-Stokes configuration with three different pump pulse widths of 10 ns, 17 ns and 20 ns are shown in Fig. 5.3. As mentioned in section 4.6, the Pump-Stokes configuration demonstrates Brillouin resonant peaks at 7.62 GHz and 7.8 GHz that were contributed only by the interaction of the pump and Stokes waves through longitudinal acoustic modes in an SBS process. These features are still present when the Stokes and Anti-Stokes are both interacting

with the pump wave. However, in addition to this process, there is a noticeable amplification of the Stokes wave when the Stokes and the Anti-Stokes wave are detuned at 7.4GHz below and above the pump frequency respectively. Such a process cannot be possible due to SBS that only resonates at 7.62 GHz and 7.8 GHz.

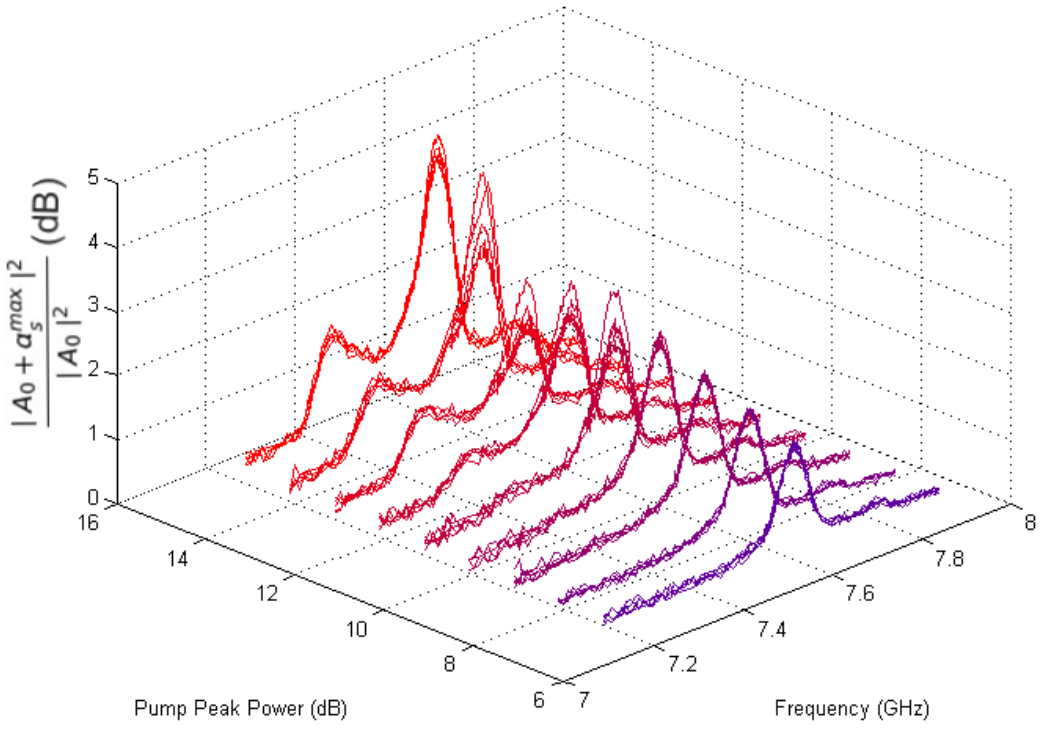

Figure 5.4: Evolution of the Stokes gain profile for the hybrid microtaper as a function of peak power of a 20 ns pulsed pump. Frequency domain traces are derived from a single time slice of the BOTDA traces where the Brillouin gain is maximum. Traces for each peak power were repeated 5 times.

The amplification at a detuning of 7.4 GHz arises because of a complex interaction of the Anti-Stokes, Stokes and pump waves with the longitudinal acoustic mode at 7.62 GHz through SBS, as well as the transverse acoustic waves at 210 MHz through GAWBS. The schematics for such a process are shown in Fig. 5.5. In comparison to the Anti-Stokes and the Stokes waves that are continuous with input power of -10 dBm each, the pump is the most dominant optical field that attains a peak power

ranging from 7 to 15 dBm. Hence, it is the only field responsible for the generation of the transverse GAWBS that resonates in the range of 210 MHz (as demonstrated in section 5.1). As the pulse travels the fiber, it generates these transverse waves along the entire medium, resulting in an overall modulation of the pump, producing side-bands that are 210 MHz apart from the nominal frequency (fig. 5.5 a) and b)).

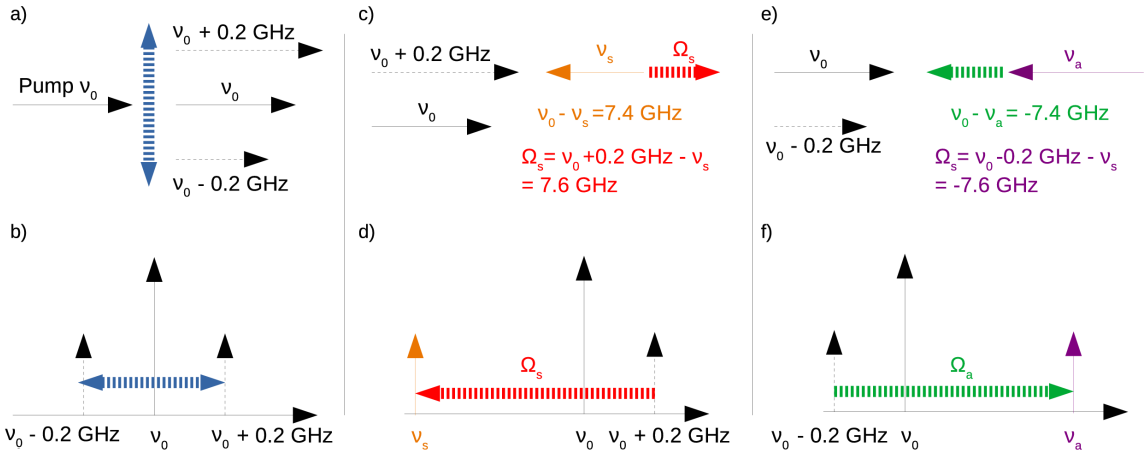

Figure 5.5: Schematic for the nonlinear three-wave interaction between a high power pump and weak counterpropagating Stokes and Anti-Stokes. a),b) generation of side-bands detuned at $\sim \pm 200$ MHz from pump wave through GAWBS. c),d) Interaction of up-shifted GAWBS (+0.2 GHz) from the pump with Stokes(ν_s) wave detuned at 7.4 GHz through SBS with 7.62 GHz resonance (Ω_s). e),f) Interaction between the Anti-Stokes (ν_a) and the down-shifted GAWBS (-0.2 GHz) from the pump.

The interaction of the GAWBS process with the detuned Stokes and Anti-Stokes is as follows: 1) the Anti-Stokes that is detuned 7.4 GHz above the pump frequency first interacts with the down-shifted GAWBS initiated by the pump through SBS, and this interaction further stimulates the GAWBS process and the SBS process in the direction of the Anti-Stokes wave (Fig. 5.5 e) and f)); 2) The up-shifted GAWBS from the pump is now enhanced by the Anti-Stokes wave and therefore it is able to interact with the Stokes wave that is detuned 7.4 GHz below the pump frequency through the means of SBS. This finally results in an amplification of the Stokes wave (Fig. 5.5 c) and d)).

Support for this theory can be demonstrated with the evolution of the Brillouin frequency spectrum as a function of the pump peak power in Fig. 5.4. Threshold for

the resonant peak at 7.4 GHz is clearly observed as the pump peak power exceeds 10 dBm. Also, simultaneously, there is a slight decrease in the net gain of the SBS process at 7.62 GHz, suggesting that at this point, both the longitudinal and transverse waves are competing for the finite amount of energy provided by the pump. Only when the pump power is exceeded beyond the threshold of 13 dBm can both the SBS and the GAWBS processes be further amplified, as shown by the re-emergence of the SBS gain beyond the pump threshold of 13 dBm.

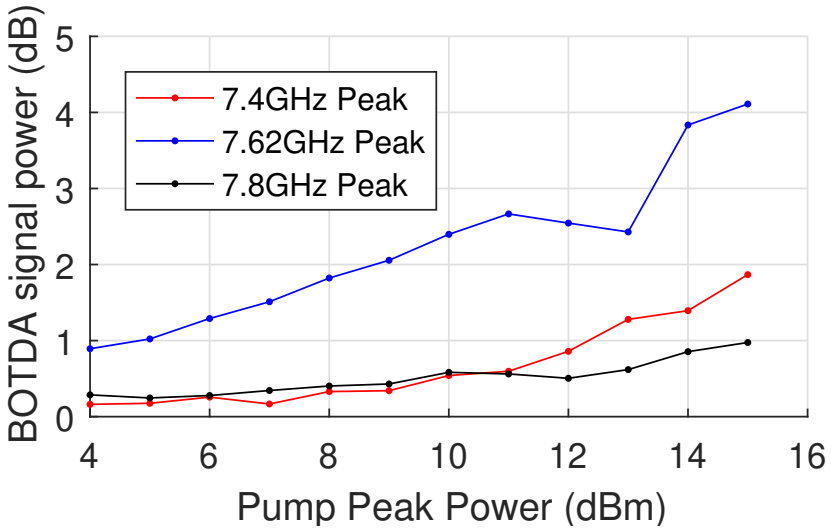

Figure 5.6: Stokes gain represented as the ratio of the Stokes peak power P_{Stokes} with respect to input pump peak Power P_{pump} with pulse width of 20 ns (bottom). Traces are plotted in dB scale.

Evidence for a threshold for the GAWBS-SBS process at a Stokes and Anti-Stokes detuning of 7.4 GHz can be clearly shown in Fig. 5.6. We see that below 11dBm, the three-wave Brillouin process and the standard SBS process are competing, as neither can be completely stimulated by the same pump power. A threshold for GAWBS in the three-wave process is visible at pump power of 11 dBm, with a reduction in the Stokes gain at 7.62 GHz, and an ascent in the Stokes gain at 7.4 GHz.

One also notices back in Fig. 5.3 that the secondary peaks at 7.4 GHz only occur ~5 ns after the pumped pulse begins to interact with the hybrid microtaper. Such a delay suggests that the amplification of the 7.4 GHz peak can only follow once the fiber attains sufficient SBS gain at 7.62 GHz, hence supporting the claim that this

process indeed requires the interaction of multiple acoustic waves to occur. Thus, we can say with certainty supported by exprimental and numerical evidence that the forming of novel secondary peaks is a consequence of the complex three-wave interaction that has been depicted in Fig. 5.5.

Chapter 6

High Birefringent Brillouin Frequency Shifts in Single Mode As_2Se_3-PMMA Hybrid Microtaper under Transverse Load

In this chapter, we demonstrate high Brillouin frequency shifts in a 60 cm As_2Se_3-PMMA hybrid microtaper with 2 μm As_2Se_3 core and 50 μm PMMA cladding diameters under transverse load. Through finite element analysis of SBS under the influence of contact stress from the loading fixture, I demonstrate that strain induced from the edge reaches towards the centre due to the elastic nature of the PMMA. The chalcogenide core enhances the dielectric tensor fluctuations arising from this strain due to its high refractive index properties, resulting in measurable shifts in the Brillouin frequency using a standard BOTDA for the first time. Numerical predictions of 0.1 ± 0.02 MHz/N mm^{-1} are in accord with the measured value. Differences in the dielectric tensor along the fast and slow axis further demonstrate the high birefringence exhibited by these tapers in the presence of load.

6.1 Measurement of Transverse Stress due to Contact Stress.

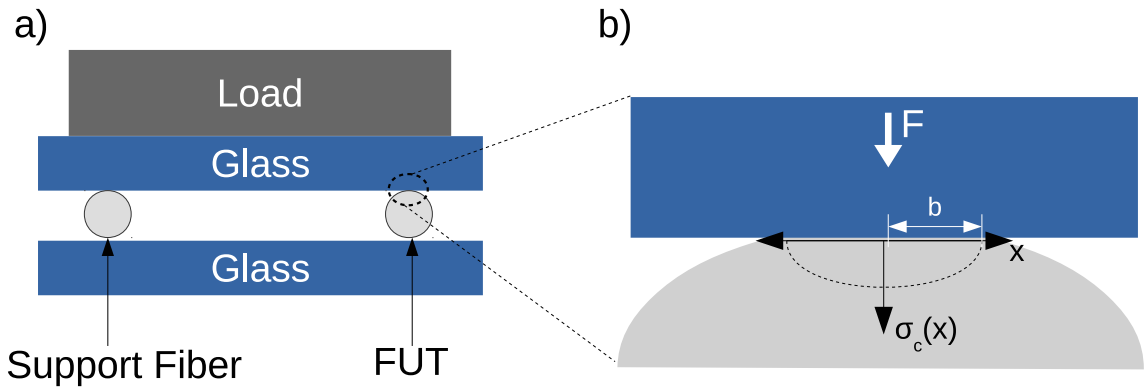

Figure 6.1: a) Schematic for loading fixture to induce strain in Chalcogenide-PMMA microtapers (fiber under test - FUT) due to transverse load. b) Diagram of contact mechanics between glass slab and PMMA rod. F = load, b = contact half-width, $\sigma_c(x)$ = contact stress over the region $-b \leq x \leq b$.

Measurement of Brillouin peak shifts due to contact stress from a transverse load were conducted as shown in Fig. 6.1a) by placing the taper into a loading fixture adapted from [76,77] . This fixture is designed to only apply plane strain ($\epsilon_z = 0, \partial\epsilon_{x/y}/\partial z = 0$) onto the fiber under test (FUT). The test fiber and an identical support fiber are loaded between two flat glass plates, allowing for a contact length of 60.0 mm. Load in the form of steel plates is applied incrementally to the top plate, ensuring that there is no microbending on the glass plates. Measurements of the Stokes response swept over the Brillouin frequency range of 7 - 8 GHz were obtained for each of the loading conditions (between 0-4 kg at 1 kg increment) using the BOTDA setup. Polarization controllers (not included in Fig. 4.3) on both the pump arm (after EDFA) and the Stokes arm (before FUT) were rotated at each loading to make sure there was maximal transmission of the Stokes response at the photodetector (PD).

6.2 Theory and Numerical Simulations for SBS in the Presence of Transverse Load

In order to numerically calculate the SBS spectrum in the hybrid microtaper in the presence of transverse strain from two glass slabs that are in contact with the PMMA, we first calculate the deformation u_i of a cross section profile of the microtaper using the linear elastic equation [4, 108]

$$-\sigma_{ij,j} = f_i = 0 \tag{6.1a}$$

$$\sigma_{ij} = c_{ijkl} S_{kl} \tag{6.1b}$$

$$S_{kl} = \frac{1}{2}\left(u_{k,l} + u_{l,k}\right), \tag{6.1c}$$

where the stress tensor σ_{ij} is expressed as a tensor product of the elastic and strain tensor c_{ijkl} and S_{kl} respectively, $\sigma_{ij,j}$ is the divergence of σ_{ij} written in Einstein summation convention ($\sigma_{ij,j} = \partial \sum_j \sigma_{ij}/\partial x_j$) and f_i is known as the force per unit volume that is distributed throughout the entire cross-section of the waveguide. However, since the forces are only applied on the boundary, and since the impact of gravity is negligible in this case, we assume $f_i = 0$ over the entire surface. By applying an inner product of the elastic equation with a test function v_i and integrating over the fiber cross-section A, we obtain the variational formulation of Eq. (6.1)

$$-\int_A \sigma_{ij,j} v_i \, \mathrm{d}S = 0. \tag{6.2}$$

Due to second order derivatives present in Eq. (6.1a)), we apply an integration by parts

$$-\int_A \sigma_{ij,j} v_i \, \mathrm{d}S = \int_A \sigma_{ij} v_{i,j} \, \mathrm{d}S - \int_{\partial A} (\sigma_{ij} n_j) v_i \, \mathrm{d}S, \tag{6.3}$$

where n_j is the outward unit normal at the boundary and $\sigma_{ij} n_j$ is the derived stress

vector, known as the *traction*, at the boundary of the waveguide, and is treated as a boundary condition for the finite element analysis. We know by the experiment that the traction is only applied in the regions ∂A_T which are the regions where the glass slab is in contact with the fiber rod.

$$\int_A \sigma_{ij} v_{i,j} \mathrm{d}S = \int_{\partial A_T} T_i v_i \mathrm{d}S, \tag{6.4}$$

while the integral around the remaining part of the boundary is treated as Dirichlet condition. In our case, $\vec{\mathbf{T}} = \pm\sigma_c(r)\hat{\mathbf{j}}$ is the traction resulting from the contact stress distribution $\sigma_c(r)$ that is applied at the boundary along a contact half-width b at the region of interaction (Fig. 6.1b). The contact stress due to the load from the glass slab in contact with two PMMA rods with radius R and length L is expressed as:

$$\sigma_c(x) = \frac{F}{\pi b L}\left(1 - \frac{x^2}{b^2}\right) \; -b \le x \le b \tag{6.5}$$

$$b = \left[\frac{2FR}{\pi L}\left(\frac{1-\nu_1^2}{E_1} + \frac{1-\nu_2^2}{E_2}\right)\right]^{1/2}, \tag{6.6}$$

where E_1 =70 GPa, E_2 =6.08 GPa, $\nu_1 = 0.212$ and $\nu_2 = 0.327$ are the elastic moduli and the Poisson ratios for glass slab and fiber rod respectively. Because of the compressive nature of the traction applied to the fiber rod, $\vec{\mathbf{T}} = -\sigma_c(r)\hat{\mathbf{j}}$ for the region in contact with the top of the fiber rod, and $\vec{\mathbf{T}} = \sigma_c(r)\hat{\mathbf{j}}$ for the region in contact with the bottom.

The variational form described above for σ_{ij} in Eq. (6.4) essentially leads to solving for the displacement vector field u_i, which is the true unknown. This can be explicitly expressed as follows:

$$\int_A \frac{1}{2} c_{ijkl}\left(u_{k,l} + u_{l,k}\right) v_{i,j} \mathrm{d}S = \int_{\partial A_T^+} T_i v_i \mathrm{d}S. \tag{6.7}$$

Once u_i is solved using finite element methods, it enables us to determine the distributed change in the dielectric tensor ϵ_{ij} along the cross-section of the waveguide [4]:

$$\epsilon_{ij} = \epsilon_{ij}^0 + \delta\epsilon_{ij} \tag{6.8a}$$

$$\epsilon_{ij}^0 = n^2\delta_{ij} \tag{6.8b}$$

$$\delta\epsilon_{ij} = -\epsilon_{ik}^0 p_{klmn}\epsilon_{lj}^0 S_{mn} = -n^4 p_{ijmn}S_{mn}, \tag{6.8c}$$

where p_{ijkl} is the photoelastic tensor and n is the refractive index of the material. From this, we derive the perturbed electric field E_i and the propagation constant k_z for an anisotropic dielectric tensor ϵ_{ij} using the variational formulation of Maxwell's equations as represented in vector finite elements (Section 2.1) [103]:

$$\vec{\nabla} \times \left(\frac{1}{\mu}\vec{\nabla} \times \mathbf{E}\right) - k_0^2\epsilon_{ij}E_j = 0. \tag{6.9}$$

With the derived electric field, propagation constant and the anisotropic dielectric tensor, we finally derive the effect of the contact stress on the stimulated Brillouin scattering of the hybrid microtaper in the presence of two counter-propagating optical fields $E_i^{(1)}$ and $E_j^{(2)}$ $(i, j = x, y, z)$ detuned by frequency Ω by using an elastodynamic equation as presented in Section 2.3.1 [27, 74, 106],

$$-\rho\Omega^2 u_i - \left[c_{ijkl}u_{k,l} + i\Omega\eta_{ijkl}u_{k,l}\right]_{,j} = \left[\epsilon_0\epsilon_{im}\epsilon_{jn}p_{klmn}E_k^{(1)}E_l^{(2)*}\right]_{,j}. \tag{6.10}$$

Upon obtaining the displacement field for a given Ω, we calculate the SBS spectrum by calculating the kinetic energy of the displacement field $u_i(\mathbf{r}, t)$, as defined by [27, 74, 106]:

$$E_k(\Omega) = \frac{1}{4}\int_A \mathrm{d}S\ \rho\Omega^2 u_i(r)^* u_i(r), \tag{6.11}$$

using the parameters as provided in Section 2.3.1 [27, 28, 106].

6.3 Results

Table 6.1: Calculated mechanical and optical properties for As_2Se_3-PMMA microtapers [27, 28] and SMF28 [106] inside the glass plate loading fixture with transverse load of 4 kg. Δn_{eff} represents the shift in refractive index due to the transverse load.

	SMF28 core(clad)	$As_2Se_3(PMMA)$
Density ρ (kg/m^3)	2254(2203)	4640(1187)
Elast. mod. E (GPa)	70.43(72.55)	33.62(6.08)
Poisson Ratio ν	0.178(0.170)	0.202(0.327)
Contact Stress σ_c^0 (MPa)	307.22	125.97
Half-width b (μm)	0.83	2.02
Refract. ind. n	1.4492(1.4440)	2.674(1.481)
n_{eff} (w/o load)	1.446314	2.6155
Δn_{eff}^y (with load)	1.10×10^{-5}	8.5×10^{-4}
Δn_{eff}^x (with load)	-3.38×10^{-6}	2.6×10^{-4}
$\Delta\nu_B^y$ (MHz) from Δn_{eff}^y	0.083	2.61
$\Delta\nu_B^x$ (MHz) from Δn_{eff}^x	-0.025	0.87

Finite element calculations for the strain and dielectric tensor S_{yy} and $\delta\epsilon_{yy}$ in response to transverse load of 4 kg are shown in Figs. 6.2 and 6.3. Mechanical and optical deviations due to load for the microtaper are summarized in Table 6.1. From Table 6.1, we realize that significantly low elastic moduli (i.e. more elasticity) for the PMMA allows for a relatively low contact stress applied on a much larger contact half-width in comparison to SMF28. This elastic nature of the soft PMMA cladding allows for more expansion of the strain throughout the microtaper as shown in Fig. 6.2a), eventually providing a significant contribution of the strain within the chalcogenide core. On the other hand, the strain distribution for the SMF28 under the same conditions is relatively weak, as the stiff nature of the material prevents the strain to expand towards the core, hence reducing the strain around the core by almost a factor of 10.

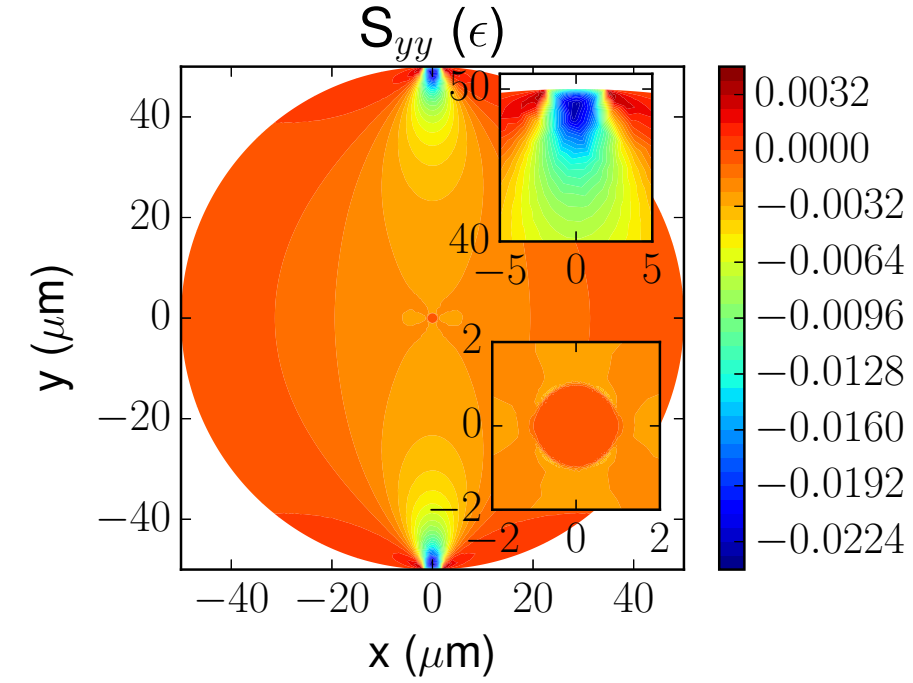

(a)

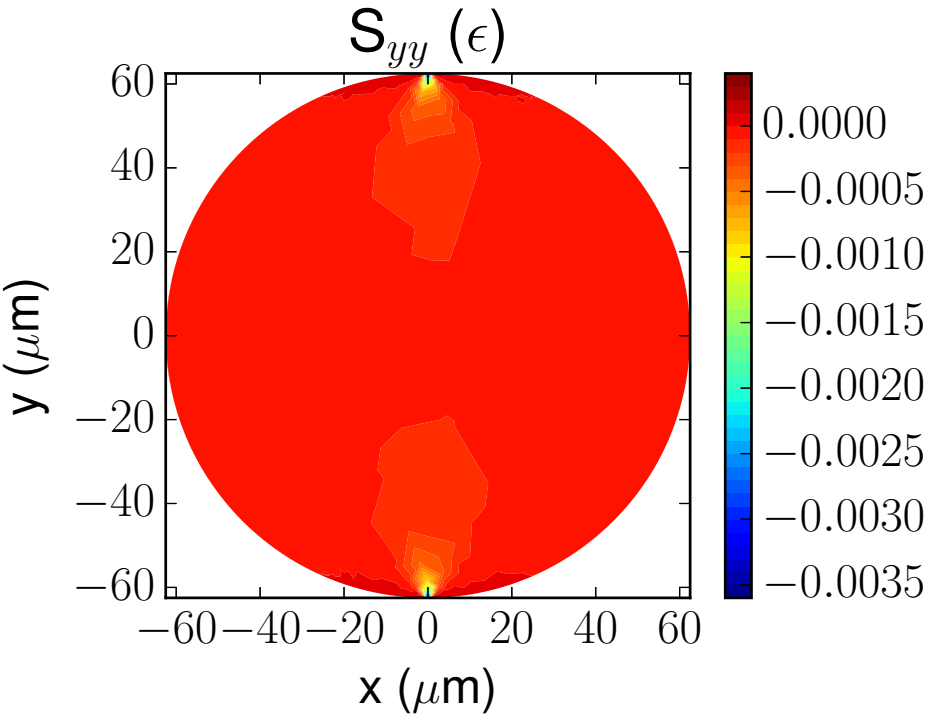

(b)

Figure 6.2: Calculated strain distribution S_{yy} for: a) chalcogenide-PMMA microtaper with core and cladding radius of 1 μm and 100 μm respectively; b) SMF28 with core radius of core and cladding radius of 4.2 μm and 62.5 μm respectively

Figures 6.3a)-b) show the change in the dielectric tensors $\delta\epsilon_{xx}$ and $\delta\epsilon_{yy}$ which are evaluated using Eq. (6.8a)-c)) using the strain distribution derived in Fig. 6.2a). Eq. (6.8c)) shows an n^4 dependence on the dielectric tensor for a given strain. This means that the effect of any strain in the chalcogenide core is immediately amplified by a factor of $2.674^4 \sim 51.12$ leading to a significantly higher value for $\delta\epsilon_{yy}$ in the chalcogenide core. In comparison, since the factors p_{ijkl} for both silica and chalcogenide are relatively the same [28, 106], the effect of strain in SMF28 can only be amplified by a factor of $1.4492^4 \sim 4.41$. This eventually leads to a tenfold increase in Δn^y_{eff} between the chalcogenide-PMMA taper and SMF28 in the presence of a 4 kg load as shown in Table 6.1.

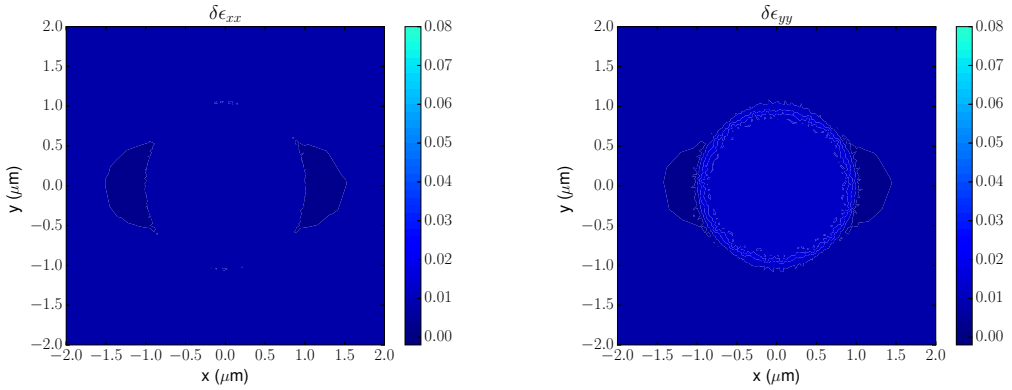

(a) (b)

Figure 6.3: Calculated distribution of the dielectric tensor a) $\delta\epsilon_{xx}$ and a) $\delta\epsilon_{yy}$ for the chalcogenide-PMMA microtaper with core radius of 1 μm.

Another aspect worth noting is the large birefringence for the chalcogenide-PMMA microtaper in the presence of transverse load. As shown in Table 6.1, even though Δn^x_{eff} is found to be in the same order of magnitude as Δn^y_{eff}, the difference between the two is 5.9 $\times 10^{-4}$, which results in a difference of 1.6 MHz between the Brillouin peaks from each polarization. This characteristic is also evident in Fig. 6.3a), where even though the strain distribution for $\Delta\epsilon_{xx}$ is non-zero, it is much lower in magnitude to that found in $\Delta\epsilon_{yy}$ for Fig. 6.3b).

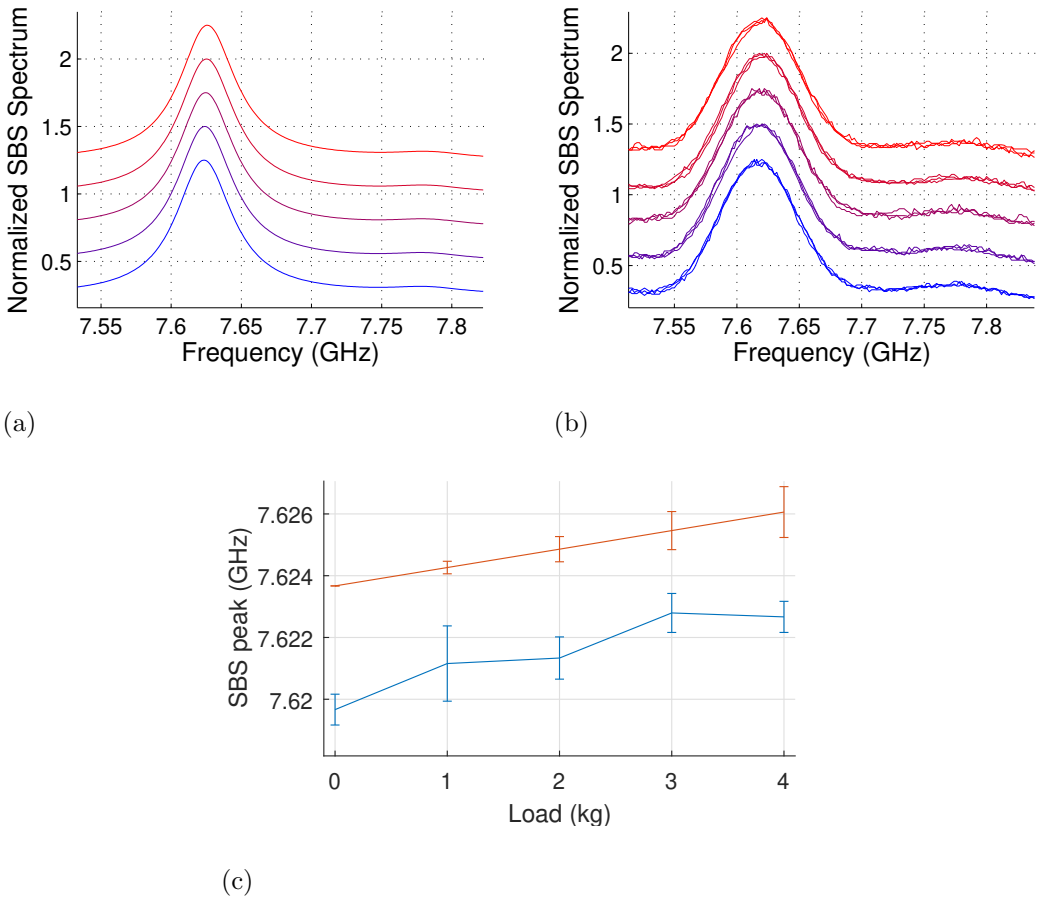

Figure 6.4: Comparison between a) numerical and b) experimental Brillouin frequency spectrum shift from 0 kg load (blue) to 4 kg load (red) at 1 kg increment. c) Numerical (red) and experimental (blue) values for Brillouin peak shift vs load.

The numerical results in Fig. 6.4a) represent the calculations for Eq. (6.11) as a function of Brillouin frequency detuning under the influence of transverse load ranging from 0 to 4 kg at 1 kg increments. The effects of the large dielectric tensor $\delta\epsilon_{ij}$ near the chalcogenide core result in significant changes in the propagation constant which then lead to observable shifts in the Brillouin peak as also shown in Fig. 6.4c). Uncertainties in the refractive index error on the numerical calculation in Fig. 6.4c) represent the fluctuation in the effective Brillouin peak due to the superposition of the individual Brillouin spectra contributed by each polarization [87]. This occurs due to: 1) lack of control of the light polarization inside a single-mode fiber [87]; 2) inability to rotate the optical field from the SMF28 to the fast axis of the chalcogenide core using a fixed angled coupling between the two. Thus, the Brillouin peak in the

presence of a given tranverse load for a single BOTDA reading can be represented as [87]

$$\nu_{Total} = \frac{1}{2}\left[(\nu_y + \nu_x) \pm (\nu_y - \nu_x)\right]. \tag{6.12}$$

A linear fit for the data presented in Fig. 6.4c) shows that the slope of the Brillouin frequency shift under load is around 0.06 ± 0.01 MHz/Nmm^{-1}.

The curves in Fig. 6.4b) are the measurements of the Brillouin spectrum from the Stokes response of the BOTDA measurement under the presence of transverse load of 0 to 4 kg at every 1 kg increment. Despite the broad line-width due to the convolution effect of the pulsed pump wave as well as the damping acoustic effect of the PMMA cladding [27], the linear shift in the Brillouin peak frequency w.r.t. transverse load is still apparent. These shifts are further analyzed in Fig. 6.4c), showing a slope of 0.08 ± 0.02 MHz/Nmm^{-1}, which is within the range of what is expected numerically. Lack of asymmetry in the Brillouin spectrum for both experimental and numerical results suggest that electrostriction is only dominant within the chalogenide core, and is in complete isolation from the strain and the change in dielectric that is induced around the PMMA. This highlights the benefit of having ultra-confined electric and acoustic fields due to the drastic mismatch between refractive indices and the acoustic impedance ($Z = \sqrt{E(1-\nu)\rho/[(1+\nu)(1+2\nu)]}$) between the two materials. As such, the Brillouin frequency shift as a function of the transverse load can vary linearly until plasticity effects in the PMMA or fracture thresholds are reached. In the case of experimental results, the symmetry in the Brillouin peak also indicates that the deformation induced on the fiber from the glass slab is planar in nature, and axial strains from microbending are negligible.

In conclusion, I demonstrated high birefringent Brillouin frequency shifts exhibited by the single-mode hybrid As_2Se_3-PMMA hybrid microtaper in the presence of tranverse load on a glass slab loading fixture, surpassing the responses attained by standard silica fibers by about factor of 27.

Chapter 7

Electrostriction in Dual-Core As_2Se_3-PMMA Microtapers

In this chapter, I present the results of studies on the Brillouin profile and birefringent properties of the dual-core Chalcogenide-PMMA microtapers. Finite element analysis for such a dual-core microtaper demonstrates that under intrinsic variations in the effective refractive indices imposed by the four dominant optical supermodes, the Brillouin peak from an even or odd optical mode differ by 14 MHz . In experiment, excitation of both the Brillouin profiles is achieved by angle-coupling of an SMF28 with only one of the cores of the dual-core microtaper. BOTDA measurements conducted on this coupled microtaper demonstrate the asymmetry in the SBS profile due to the overlap of intrinsic SBS spectra originating from the electrostriction through individual even and odd optical modes. In addition to this, through simulations, I demonstrate a novel transverse stress sensor that determines the magnitude as well as the orientation of a transverse load (applied as described in chapter 6). This system exhibits a linear relation between the net load applied to the fiber and the average Brillouin peak frequency shifts of the even and odd eigenmodes that is sufficient to retrieve the magnitude and orientation of the load.

7.1 Fabrication and Coupling of Dual-Core Chalcogenide-PMMA Microtaper

The fabrication and coupling methods for dual-core microtapers are similar to what is mentioned in chapter 3, as demonstrated in Fig. 3.2 and 3.5. However, inclusion of a second chalcogenide core imposes modifications in fusing and coupling of these microtapers, which I describe below.

Figure 7.1: Cross-sectional view of the chalcogenide dual-core (21.25 μm diameter each) surrounded by PMMA cladding (1100 μm diameter) after polishing the surface.

7.1.1 Fusing for Dual-Core Fibers

Fusing of the dual core As_2Se_3 preform with the PMMA preform and the PMMA microtube is done in the same manner as for the single core As_2Se_3 preforms as shown in Fig. 3.2. However, in this case, we place two As_2Se_3 fibers into the microtube instead of just one. Also, the duration of time the fibers are kept in the lathe determines how close the two As_2Se_3 cores are fused to each other. In my case, in order to have the two 2 μm diameter cores separated by 1.98 μm, the dual-core sample was kept in the lathe for 10 hours.

7.1.2 Coupling of the SMF28 to the Chalcogenide Dual-Core Fiber

As mentioned in 3.6, the most effective method of coupling between the SMF28 and the chalcogenide core is through custom angled coupling that maximizes the transmission coefficient while preventing Fresnel reflections. Moreover, the coupling is secured by a UV cured epoxy for easier portability of the sample to the tapering or measurement setups. Coupling for a dual-core sample, on the other hand, requires that the light is maximally coupled to only one of the cores of the microtaper, while the second core is left uncoupled, as shown in Fig. 7.2.

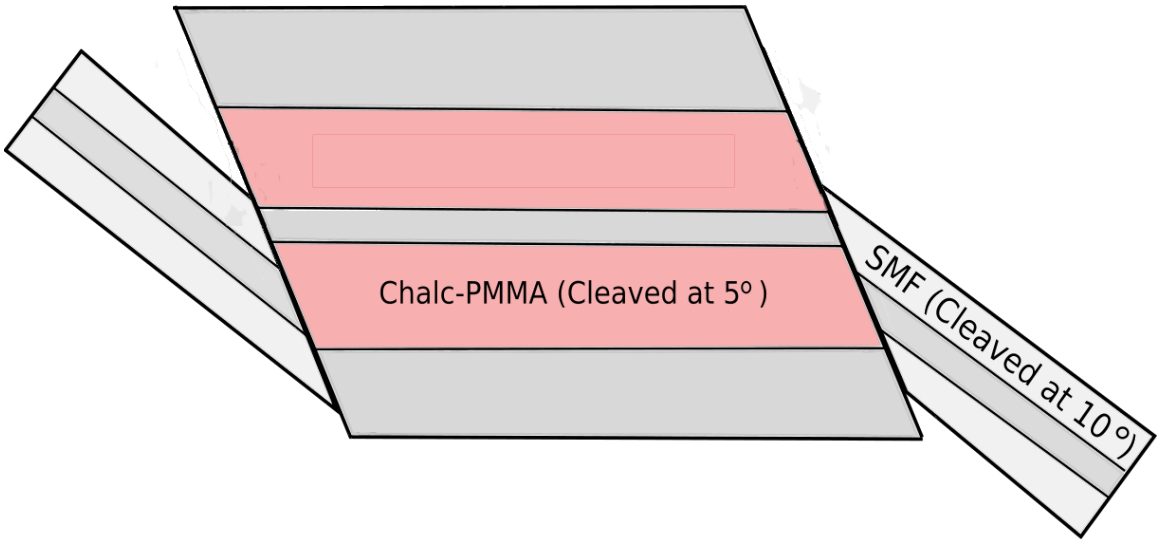

Figure 7.2: Schematic for coupling a standard silica fiber (SMF28) with the hybrid dual-core microtaper.

Such technique allows for excitation of all the even and odd modes of the microtaper, enabling me to excite asymmetric SBS profiles. They are formed through the overlap of intrinsic SBS spectra originating from the electrostriction through individual even and odd optical modes.

Following these modified procedures, the dual-core sample is further tapered down to an individual core radius of 2 μm using the heat-brush tapering method, as described in section 3.7, followed by SBS measurements using BOTDA as shown in section 4.3.

7.2 Numerical Simulations for the Electromagnetic Field of a Dual Core Microtaper

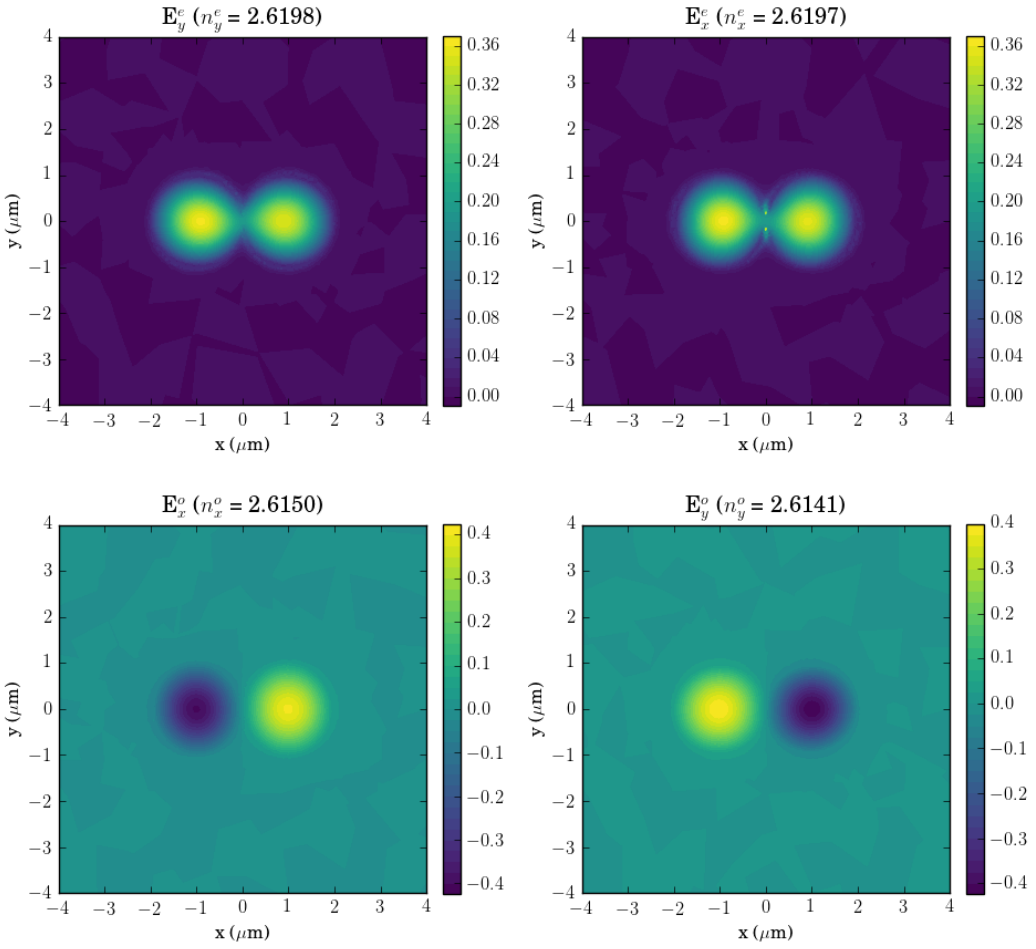

Figure 7.3: Dominant electric field amplitudes and the effective refractive indices of the four orthogonal states derived for a dual core Chalcogenide-PMMA microtaper with an individual core diameter of 2.00 μm and separation of 1.98 μm

Finite-element simulations for a dual-core chalcogenide-PMMA microtaper with a core diameter of 2 μm and separation of 1.98 μm are demonstrated in Fig. 7.3. As predicted, the first four eigenmodes of the waveguide do exhibit even and odd mode profiles for each of the individual x and y polarizations. Large variations in the propagation constant between the odd and the even eigenmodes arise due to the large refractive index difference between the core and the cladding material, and how much the field interacts with each of the materials. The even modes E_x^e E_y^e exhibit an effective refractive index of 2.6198 and 2.6197 respectively, while the the odd modes

E_x^o E_y^o exhibit an effective refractive index of 2.6150 and 2.6141 respectively, which is quite close to the effective refractive index of 2.6155 for a single-core chalcogenide-PMMA microtaper. This suggests that most of the electric field stays confined within the chalcogenide region which has an intrinsic refractive index of 2.674, and doesn't penetrate much into the PMMA cladding and the coupling region between the two cores. The refractive index difference between the even and the odd modes arises due to the intrinsic node along the y axis of the waveguide for the odd modes. This forces the fields on either side of the node to penetrate further towards the cladding of the microtaper, resulting in a drop in the effective refractive index for these odd modes as the PMMA has an intrinsic refractive index of 1.481.

As mentioned in Section 1.5, relative difference in the effective refractive index between the even and odd modes for the dual-core fiber results in a mismatch of the phase velocities, resulting in a sinusoidally varying intensity profile between the two cores with a period of $\Lambda = \lambda / \mid n_{eff}^e - n_{eff}^o \mid$. This allows the field to couple between the two cores. For the dual-core chalcogenide cores, the spatial period for light at around 1550 nm is $\sim$250 μm. Thus, two orthogonal supermodes, characterized by different phase velocities, lead to a periodic switching of power between the two cores along the fiber. The strength of the coupling between the cores depends on the spatial overlap of the two excited supermodes. In our case, the effective overlap between the two modes is quite strong, as most of the light is contained within the chalcogenide-cores for either of the supermodes.

7.3 Modelling of Electrostriction inside a Dual-Core Microtaper

Here, I present the numerically obtained SBS spectra for a cross-section of a dual core chalcogenide microtaper as shown in Fig. 7.4. These spectra have been obtained by evaluating the kinetic energy of the acoustic beam as shown in Fig. 7.5 (i.e. $\omega^2 \int_S \rho \mid u_i \mid^2$) as a function of the detuning frequency between the two optical

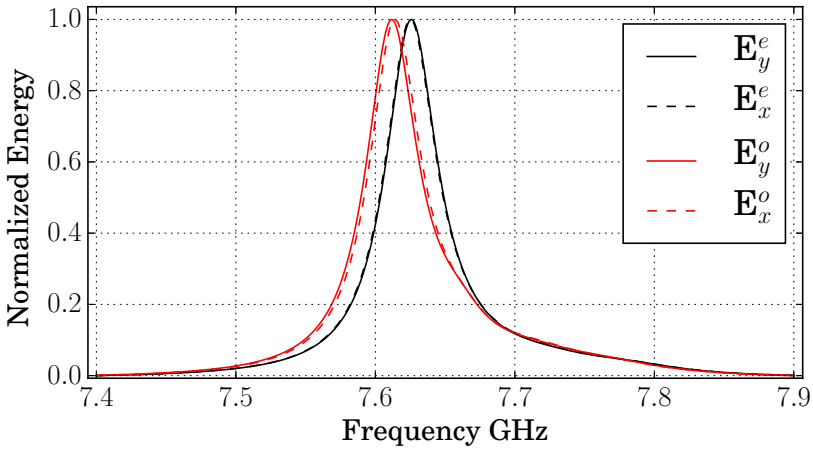

Figure 7.4: Numerical results of the energy spectra for a 2 micron diameter dual-core Chalcogenide-PMMA microtaper. Large differences in n_{eff} between the supermodes result in a peak shift of 14 MHz in the Brillouin spectrum for the even mode (black) and the odd mode (red).

fields. The results indicate that the Brillouin shift between two given supermodes is predominantly based on the difference in the effective refractive index. For example, the largest variation in the Brillouin peaks is obtained between the E_y^e and E_y^o, which is about 14 MHz. Taking into account the effective refractive indices $\mathrm{n}_y^e = 2.6198$ and $\mathrm{n}_y^o = 2.6141$, the classical Brillouin shift $\Delta\nu_B = 2(n_y^e - n_y^o)\nu_a/\lambda \approx 16.54$ MHz, which is close in order to the numerical value obtained through the elastodynamics equation. What is also intriguing is that the Brillouin spectrum obtained for each supermode is not symmetric in nature. This indicates the rich acoustic dynamics that are present due to the complex shear modes that are generated alongside the dominant longitudinal mode in such hybrid microtapers. Also, similar to the single-core tapers, there are traces of the secondary Brillouin frequency peak near the 7.8 GHz region, further contributing to the asymmetry of the Brillouin spectra for the supermodes.

The distribution for the acoustic energy for E_y^e and E_y^o is demonstrated in Fig. 7.5a)-b). In either case, the energy distribution is almost identical, as the elastodynamic model mainly relies on the magnitude of the field due to the nonlinear electrostrictive force $T_{ij} = \chi_{ijkl}E_kE_l \approx \chi^{(3)} \mid E \mid^2$. This means that the electrostriction

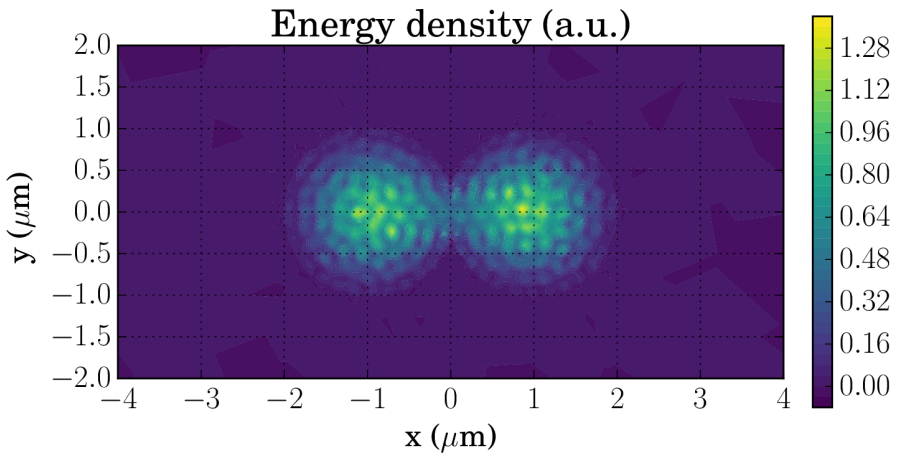

(a)

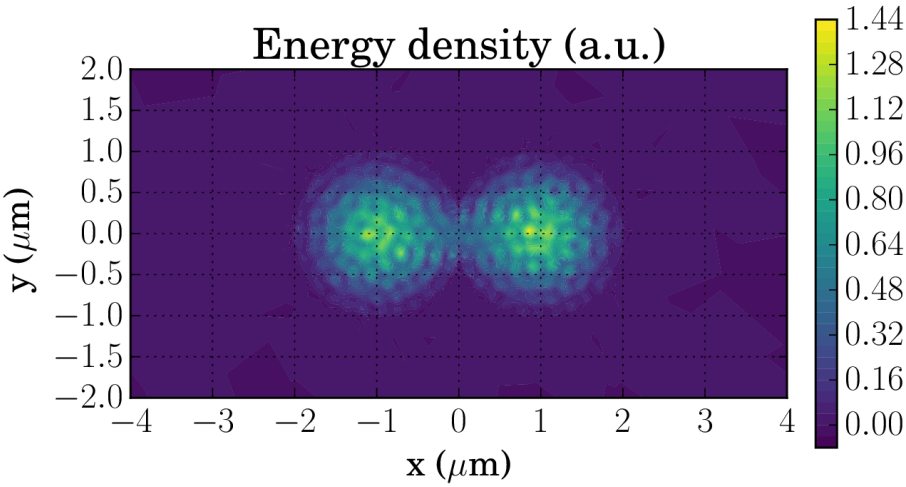

(b)

Figure 7.5: Energy distribution for the acoustic wave in the presence of an a) even and b) odd supermode.

process between either supermode is relatively quite similar, even if one of the modes is intrinsically asymmetric along the y-axis.

Similarly as for the single core microtapers, the combination of the acoustic impedance between core and cladding and the optical forces produces a rippling behaviour in the acoustics energy density. It is due to interference between the transverse and the longitudinal acoustic modes that are both generated in this microtaper, unlike the purely longitudinal mode that is dominant in SMF28. The generation for both longitudinal and transverse acoustic modes is a consequence of the acoustic impedance mismatch between the two materials and the ultra-confinement of the electric field inside the core.

7.4 Experimental Results for Electrostriction inside a Dual-Core Microtaper

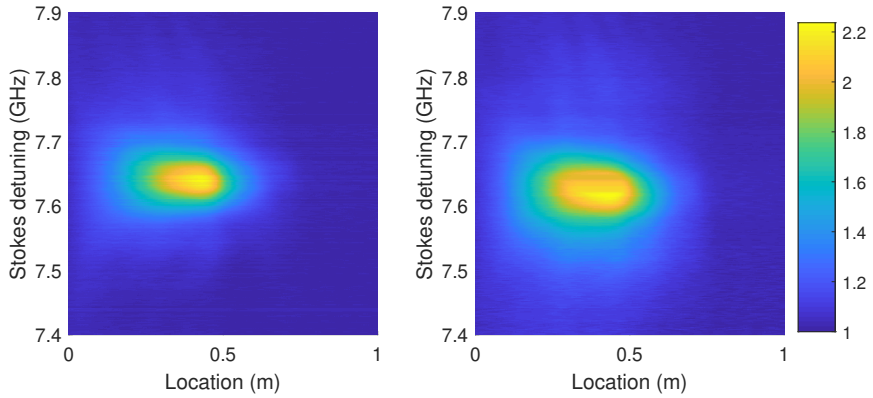

Figure 7.6: BOTDA traces for the dual-core chalcogenide fiber aligned to excite electrostriction from an even (left) optical supermode and an odd (right) optical supermode.

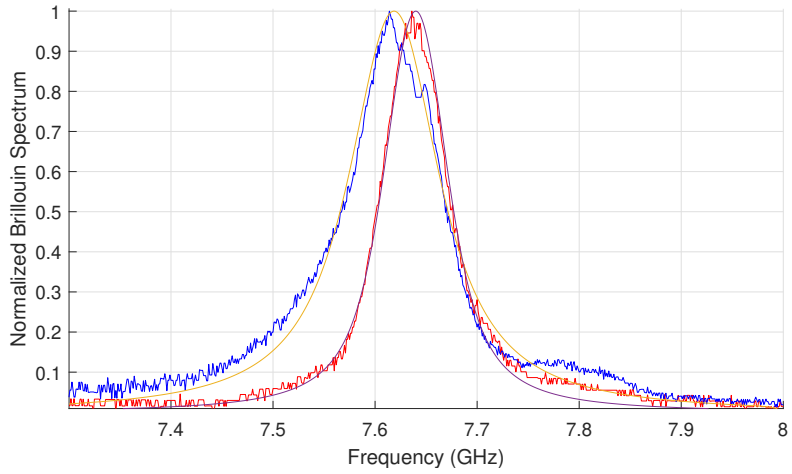

Figure 7.7: Experimental results of the peak BOTDA spectrum for a 2 micron diameter dual-core Chalcogenide-PMMA microtaper. Voigt fitting over the experimental results for the even mode (red) and odd mode (blue) are conducted to demonstrate a shift of 19 $\pm$ 3 MHz between the two Brillouin peaks.

Figures 7.6 and 7.7 show the BOTDA traces as well as the BOTDA frequency sweeps that are taken for the same dual-core chalcogenide-PMMA microtaper under two different polarization alignments of the pump and Stokes wave. It is to be noted that although the even and odd modes are almost independent of polarization axis

(Fig. 7.4), in our case, a realignment has allowed for the pump and Stokes to interact through different eigenmodes of the microtaper. The angled coupling interface between the chalcogenide and SMF, for this particular case, has the ability to alter the relative phase difference between the pump and Stokes field when the polarization is changed. Hence, variation of the SBS profile under the presence of different configurations of pump and Stokes field input demonstrates the ability of the fiber to induce electrostriction individually for an even or odd mode.

As mentioned in section 7.2, the beat period due to the supermode phase velocity mismatch is $\Lambda = 249$ μm. Such a period would be only detectable if the pulse width of the optical pump wave is less than $T = n\Lambda/c \sim 2.33$ ps. However, since the pulse width for the pump wave in the BOTDA experiment is 20 ns, the Stokes response obtained in the BOTDA experiment is an accumulated response of the electrostriction occurring at individual points along the fiber. This averaging process filters any oscillatory trends in the BOTDA traces in Fig. 7.6 that arise due to the large Brillouin peak differences between the even and odd supermodes.

Voigt fitting for each of the SBS measurements in Fig. 7.7 allows us to determine an SBS peak at 7.639 $\pm$ 0.002 GHz for the even mode and 7.620 $\pm$ 0.002 GHz for the odd mode, resulting in a SBS peak difference of 19 $\pm$ 3 MHz. Discrepancies in the theoretical and experimental Brillouin peak differences can be interpreted as: 1) the uncertainty in the microtaper diameter during the tapering procedure, as well as the separation between the two cores during the fusing process, which is estimated to about 10%; 2) Inability of maintaining a dominant supermode during measurements in the dual-core fiber, leading to asymmetries and multiple peak profiles in the BOTDA traces as seen in the trace for an odd supermode in Fig. 7.7; 3) Inability to explicitly manipulate the polarization, the mode profile and the relative phase of the optical field inserted into the microtaper from the SMF28 due to the fixed angled coupling between one core of the microtaper and SMF28. Nevertheless, it is evident that under different configurations, the dual-core chalcogenide-PMMA microtaper is able to produce two distinct SBS profiles that are a result of the electrostriction arising

from one of the two dominant supermodes (even or odd) of the electric field.

7.5 Numerical Prediction for Dual-Core Chalcogenide Microtapers under the Presence of Transverse Stress

In this section, I demonstrate high Brillouin frequency shifts in a 2 μm As_2Se_3 core diameter dual-core and 100 μm PMMA cladding diameters under transverse load. Similar to the finite element calculations conducted in chapter 6, I demonstrate that strain induced from the edge is still traceable towards the centre. It is so due to the elastic nature of the PMMA, followed by the enhancement of the dielectric tensor fluctuations in the chalcogenide core arising from its high refractive index properties. However, unlike in chapter 6, radial asymmetry in the dual-core fiber allows one to measure the angle at which the transverse load is applied. Finite-element measurements indicate that the fiber provides a linear relation between the load applied onto the fiber and the average of the Brillouin shifts for (E^e_y,E^e_x) and (E^o_y,E^o_x) modes respectively.

Similar to results presented in chapter 6, these calculations were done assuming the sample was loaded using a glass fixture as shown in Fig. 6.1. In chapter 6, simulations along the y-axis were sufficient as the fiber was radially symmetric. For the dual core, however, the response of the Brillouin shift varies depending on the alignment of the load from the glass fixture with the fiber rotation. Figure 7.8 shows each strain distribution S_{xx}, S_{xy} and S_{yy} for a load of 2 kg applied on a 66 mm sample by the glass fixture along the x-axis, at an angle of 45°, and from the y-axis respectively. Although all three strain tensor components are comparable in magnitude, the tensor components S_{xx} for the load in the x-axis, S_{xy} for the 45° angle, and S_{yy} for the y-axis exhibit the largest deformation within the core. Although some configurations effectively only provide a rather constant deformation to the chalcogenide core, the uniformity is diminished when one derives the fluctuation in the dielectric tensor

$\delta\epsilon_{ij}$ for each of the configurations shown in Fig. 7.9. The effect is visible as the spatially varying deformations from the other components of S_{ij} begin to interfere with the more uniform deformations in the core. As seen in all configurations, $\delta\epsilon_{xx}$ is perturbed the most, followed by $\delta\epsilon_{yy}$, and $\delta\epsilon_{xy}$ being the least contributing factor. The intercalating of the elastic PMMA material between the two stiff chalcogenide cores placed in the line of stress from the cladding effectively enhances the sensitivity of the material near the centre of the dual-core, leading to large perturbations in the dielectric tensor near this region. Moreover, large refractive indices of the chalcogenide core further enhance the perturbations in the core even further by a factor of ~ 51.12 as mentioned in section 6.3.

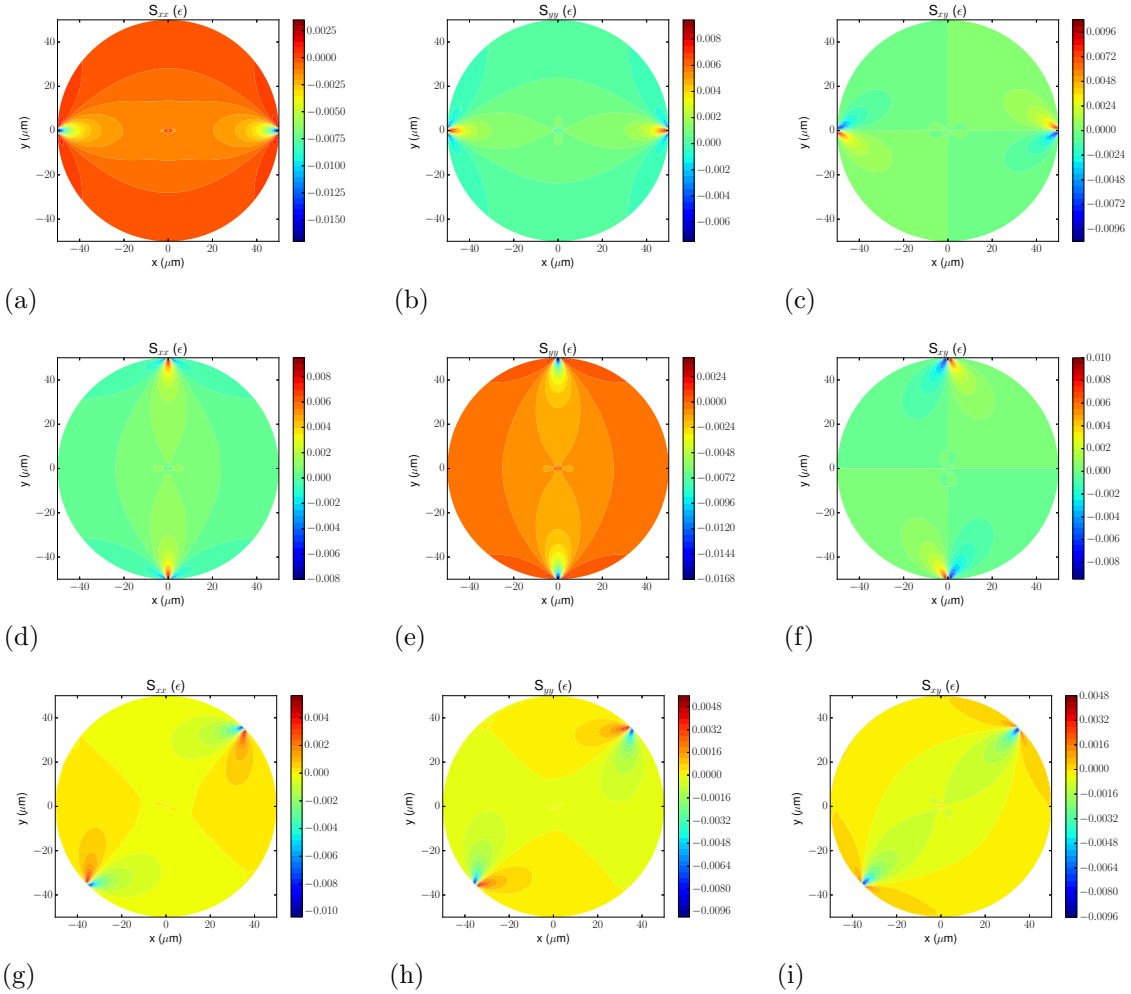

Figure 7.8: Distribution for a) S_{xx}, b) S_{yy}, c) S_{xy} for a transverse load of 2 kg on 66 mm sample in the x-axis; d) S_{xx}, e) S_{yy}, f) S_{xy} for a load in the y-axis; g) S_{xx}, h) S_{yy}, i) S_{xy} for a load at 45°.

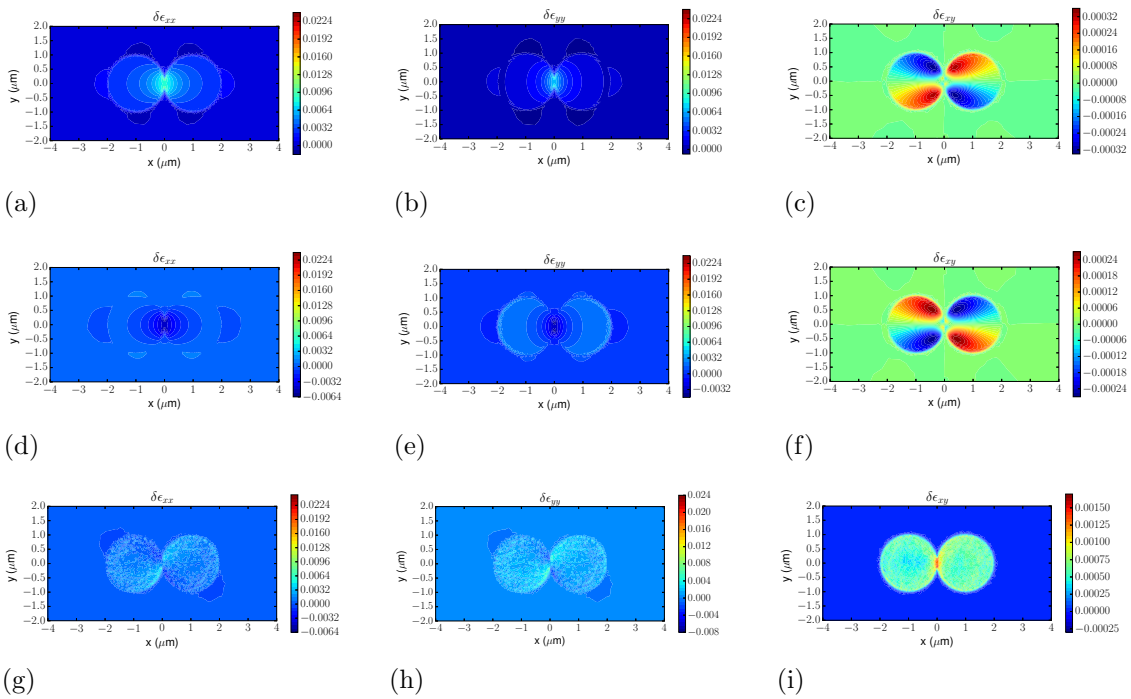

Figure 7.9: Distribution for a) $\delta\epsilon_{xx}$, b) $\delta\epsilon_{yy}$, c) $\delta\epsilon_{xy}$ for a transverse load of 2 kg on a 66mm sample in the x-axis; d) $\delta\epsilon_{xx}$, e) $\delta\epsilon_{yy}$, f) $\delta\epsilon_{xy}$ for a load in the in the y-axis; g) $\delta\epsilon_{xx}$, h) $\delta\epsilon_{yy}$, i) $\delta\epsilon_{xy}$ for a load at 45°.

We now calculate the shifts in the Brillouin peak frequency for each of the eigenmodes of the dual-core microtaper in presence of transverse load in the x and y axis respectively. I will also show how they can be manipulated to derive linear relations that determine the orientation of the stress. We introduce new variables ν_{Bc}^{ab} which represents the Brillouin peak frequency due to stress along the axis $b = x, y$ for the individual modes E_c^a where $a = e, o$ represents an even or odd mode with polarization $c = x, y$. Although, individually, each of the variables generally exhibit a nonlinear relation with respect to the applied load, by defining new average variables

$$\begin{aligned}
\nu_{x(av)}^{e} &= \left(\nu_{Bx}^{ex} + \nu_{By}^{ex}\right)/2 \\
\nu_{x(av)}^{o} &= \left(\nu_{Bx}^{ox} + \nu_{By}^{ox}\right)/2 \\
\nu_{y(av)}^{e} &= \left(\nu_{Bx}^{ey} + \nu_{By}^{ey}\right)/2 \\
\nu_{y(av)}^{o} &= \left(\nu_{Bx}^{oy} + \nu_{By}^{oy}\right)/2
\end{aligned} \tag{7.1}$$

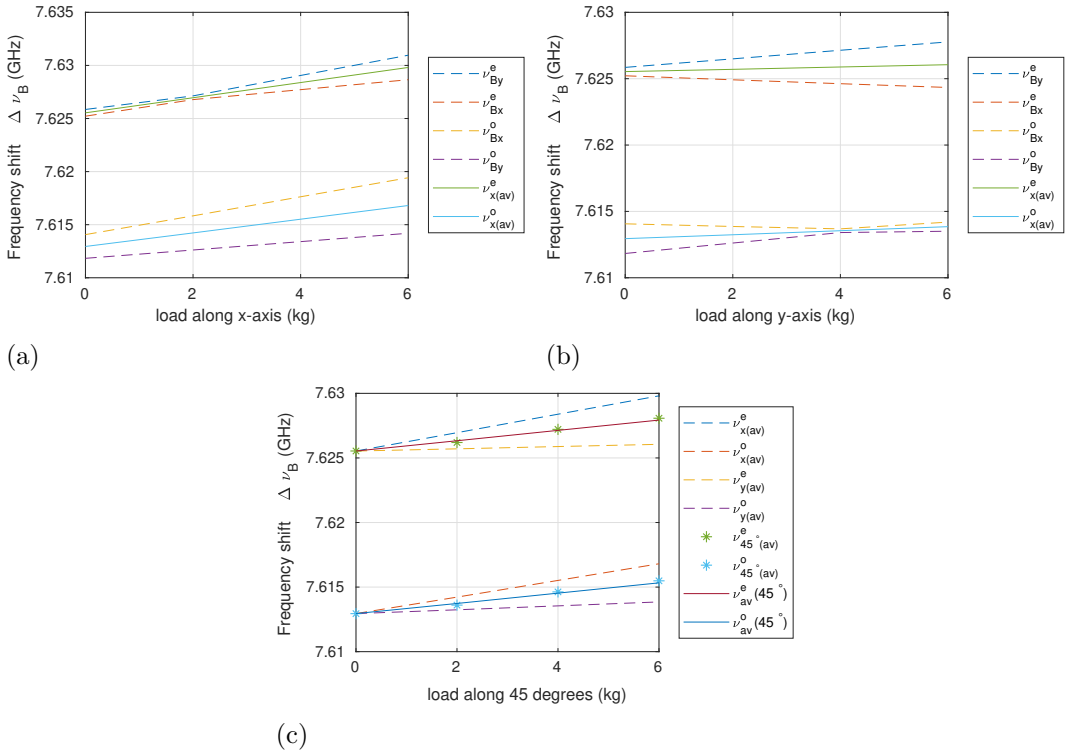

Figure 7.10: Evolution of the Brillouin peak shifts for even and odd modes for the dual-core microtaper in the presence of transverse load at a) x-axis and b) y-axis. c) Overlay of the numerically simulated Brillouin peak shift due to transverse load at 45° from the x-axis with the weighted average of the individual Brillouin shifts.

we can retrieve the linear dependence. Variables shown in Eq. 7.1 represent the average of the Brillouin peak shifts for each even and odd mode under stress in the x-axis and y-axis respectively. A linear relation between the average Brillouin shifts and the tranverse load is obtained as shown in figures 7.10a) and 7.10b). To be more specific, for a load in the individual x or y axis:

$$\begin{bmatrix} \nu^e_{x(av)} \\ \nu^o_{x(av)} \end{bmatrix} = L_x \begin{bmatrix} K^e_x \\ K^o_x \end{bmatrix} + \begin{bmatrix} \nu^e_0 \\ \nu^o_0 \end{bmatrix} \tag{7.2}$$

$$\begin{bmatrix} \nu^e_{y(av)} \\ \nu^o_{y(av)} \end{bmatrix} = L_y \begin{bmatrix} K^e_y \\ K^o_y \end{bmatrix} + \begin{bmatrix} \nu^e_0 \\ \nu^o_0 \end{bmatrix}. \tag{7.3}$$

The values derived from the simulations for the constants in Eq. 7.2 and 7.3 are given in Table 7.1.

Similarly, a generalized representation for the Brillouin peak shifts for a net transverse load L applied at an arbitrary angle θ from the x-axis can be expressed as follows:

$$\begin{bmatrix} \nu^e_{x(av)} \\ \nu^o_{x(av)} \end{bmatrix} = L \left(\begin{bmatrix} K^e_x \\ K^o_x \end{bmatrix} \cos^2\theta + \begin{bmatrix} K^e_x \\ K^o_x \end{bmatrix} \sin^2\theta \right) + \begin{bmatrix} \nu^e_0 \\ \nu^o_0 \end{bmatrix} \tag{7.4}$$

Table 7.1: Calculated values for variables introduced in Eqs. 7.2 and 7.3

K^e_x (MHz/Nmm^{-1})	0.071
K^o_x (MHz/Nmm^{-1})	0.064
K^e_y (MHz/Nmm^{-1})	0.009
K^e_y (MHz/Nmm^{-1})	0.015
ν^e_0 (GHz)	7.6255
ν^o_0 (GHz)	7.6168

Comparison between the equation above and the actual simulation done at $\theta = \pi/4$ is shown in Fig. 7.10c). The linear curves $\nu^e_{av}(45°)$ and $\nu^o_{av}(45°)$ are derived using the weighted sum of the individual curves in Eqs. 7.2 and 7.3 with weights $\cos^2\theta = \sin^2\theta = 1/2$, while the dotted lines $\nu^e_{45°(av)}$ $\nu^o_{45°(av)}$ are the simulated results for a load applied at angle $\theta = \pi/4$. Both the results are in agreement, suggesting that the dual core fiber is successfully able to determine the magnitude as well as the orientation of the net transverse load using a simple linear combination of the Brillouin peak frequency shifts for the individual eigenmodes of the waveguide. Moreover, significantly large values for the constants K in Table 7.1 show that such Brillouin shift should be easily detectable using a standard BOTDA setup. Therefore, provided that one is able to couple each of the eigenmodes into the dual-core fiber individually and conduct a thorough BOTDA measurement for each mode, one should be able to determine the orientation of a load that is applied onto the fiber.

With these results, it is evident that these microtapers can be considered as new candidates for high resolution measurement devices that can retrieve complex characteristics within the fiber under transverse load using simple BOTDA measurements of the individual eigenmodes of the waveguide. By implementing similar simulations

with dual-core tapers of different diameters and separations between chalcogenide cores, we can determine what range of core diameters and separation distances are necessary to maintain such linearities, and whether the effect can be enhanced before the PMMA cladding suffers from plastic deformations [43, 44]

Chapter 8

Conclusion

The primary goal of this thesis was to narrow the gap between the experimental results and numerical simulations for SBS spectra in As_2-$SeAs_3$-PMMA hybrid microtapers that were fabricated using the techniques demonstrated by Baker *et. al.* [29, 30]. Upon successfully deriving the SBS spectra numerically using finite element analysis of the elastodynamics equation as demonstrated by Beugnot [27], and measuring the SBS in our optical fiber using a BOTDA scheme, the SBS gain profile in both the experimental and numerical regime were in accordance. This was evident by the characteristic peak in the SBS profile at 7.64 GHz followed by a secondary peak at 7.8 GHz that were attained in both regimes. Previous work conducted by [27, 28] showed discrepancies in both regimes since the simulations assumed coherent pump-Stokes configuration, while experiments relied on spontaneous Brillouin scattering generated solely from a pump. Morover, in my case coherent detection of SBS in these microtapers was only possible because of the novel angled-coupling between the SMF28 and chalcogenide core that allowed for ∼40 dB backreflection loss with atmost 2 dB transmission loss at each interface.

Beyond the characterization of the Chalcogenide-PMMA fibers, I also presented results that reveal new complexity of the Brillouin phenomena in these microtapers. I demonstrated simultaneous generation of GAWBS with SBS and high Brillouin shifts due to stress-induced birefringence in a 2 μm core and 60 cm long single-core microtaper. The GAWBS in the microtaper couples with SBS through a complex

energy transfer between weak Stokes and Anti-Stokes (AS) continuous waves in the presence of a high power pulsed pump wave. This results in an amplification of Stokes wave at 7.4 GHz due to modulation of the optical fiber by GAWBS at 211 MHz generated by the pump in addition to a strong SBS Stokes peaks at 7.62 GHz and 7.8 GHz. This is also the first time that GAWBS was generated experimentally, which shows excitation of a high spectral density of transverse waves near the 200 MHz range that are responsible for the distortion of the SBS spectrum. The experimental results are in accordance with the simulations that have been conducted using the elastodynamics model assuming two detuned copropagating optical waves.

I then presented a comprehensive study of the microtaper for high-birefringent Brillouin shifts in the presence of transverse stress from a glass slab loading fixture. It involved developping a novel theoretical approach, combining the linear elastic model and the elastodynamic equations, used to numerically solve for the shift in Brillouin peak frequency under the influence of contact stress from the loading fixture. The common link that combines these two equations is the dielectric tensor that is perturbed under stress. This tensor provides perturbations to the propagation constant of the electric field which makes solving Maxwell's equations quite non-trivial. This also provides a perturbation to the electrostrictive stress tensor when solving for the elastodynamics equations. These studies advanced our knowledge of the strain behaviour in these microtapers. I demonstrate that strain induced from the edge is still traceable towards the centre due to the elastic nature of the PMMA. The chalcogenide core enhances the dielectric tensor fluctuations arising from this strain due to its high refractive index, resulting in high shifts in the Brillouin frequency that for the first time are traceable on a standard BOTDA measurement setup. Such shifts of 0.08 ± 0.02 MHz/Nmm^{-1} are in accordance with the measured value. Differences in the effective refractive index for the fast and slow axis from the perturbations in the dielectric tensor under stress further demonstrate the high birefringence exhibited by these tapers in the presence of load.

I think what you mean is that perturbations to the propagation constants , and

lead to complicated wave solutions

Lastly, I characterized the Brillouin profile of a Dual-Core Chalcogenide-PMMA microtaper. Finite element analysis demonstrates large complexity of the Brillouin response of these microtapers. I showed that under intrinsic variations in the effective refractive indices imposed by the four dominant electric supermodes, the chalcogenide-PMMA dual-core microtaper produces a Brillouin peak difference of 14 MHz when subjected to electrostriction from an even or odd optical mode. BOTDA measurements conducted on this coupled microtaper demonstrate asymmetry in the SBS profile due to the overlap of intrinsic SBS spectra corresponding to even and odd optical modes. With these experimental results on the electrostrictive processes in the dual-core fiber I was able to model a novel transverse stress sensor that determines the magnitude as well as the orientation of a transverse load that is applied to the fiber using a glass fixture as demonstrated for the high birefringent single-core material. Such a system exhibits a linear relation between the net load applied to the fiber and the average Brillouin peak frequency shifts of the even and odd eigenmodes, which proves sufficient at retrieving the magnitude and orientation of the load. Moreover, strong Brillouin shifts for the eigenmodes, especially due to the stress in the x-axis of the fiber, play a vital role at designing novel sensor setups capable of retrieving complex characteristics within the fiber under transverse load, and do so using simple BOTDA measurements of the individual eigenmodes of the waveguide.

Despite the novelty that has been demonstrated in this thesis, there are several practical fundamental research problems open for further investigation. Firstly, and most importantly, there is still a considerable need for optimization of the coupling interface between the SMF28 and chalcogenide core. Although the technique is sufficient for achieving high transmission coefficients with minimal back-reflection, there is still more work required to understand exactly how the wavefront is perturbed as it travels from the SMF28 to the chalcogenide core. Proper finite element analysis of an electric field interacting with an infinite plane of two different materials can possibly give us a better understanding of the wavefront that couples into the chalcogenide

core. Eventually, one would like to eliminate the problem completely by designing the entire experiment using opto-electronic devices that are built using only chalcogenide fibers. Secondly, such a coupling scheme should also be modified to properly allow coupling between SMF28 and dual-core chalcogenide fibers without any significant loss in transmission. In other words, we require explicit control of the supermode that is inserted into the microwire. At present, the coupling technique only allows for coupling of one SMF28, and makes it impossible to attach two SMF28 cores to each of the cores of the dual-core microtaper. With such an advent, we would then be able to insert phase locked wavefronts in either core that are either in phase, or out of phase from each other, resembling an even or odd mode within the microtaper.

Thirdly, highly birefringent eccentric-core microwires could be used to maintain the input polarization of the electric field, and also apply intrinsic birefringence in the material for better sensing applications. This would be possible if As_2Se_3 core is placed at the edge of the PMMA cladding layer, making the microwire more sensitive to the surrounding environment. The supporting polymer layer makes the overall structure robust enough for placement in a fluid to measure refractive-index changes [40].

Fourth, with the enhanced Brillouin properties relative to silica demonstrated in this thesis, chalcogenide tapers could be used to make ultra-short Brillouin lasers. Before this can be acheived, one should eliminate or reduce the deterioration of the microtaper due to TPA and optimizes the coupling mechanism between SMF28 and the chalcogenide glass. Such lasers would enable us to reduce the damping of the bandwidth due to the PMMA cladding, and also make the Brillouin peak more sensitive to external perturbations if using in sensing applications.

Lastly, although the numerical model is quite accurate at describing the nonlinear phenomena for a cross-section of a microtaper, it completely neglects the effect of these nonlinear processes due to perturbations in the axial component of the material. A model that can predict the evolution of the gain profile along the longitudinal axis of the microtaper would make a huge impact at understanding how to achieve lasing condition in tapered fibers with large transition regions. Such models will also clarify

the evolution of the supermodes along the axis of a dual-core fiber, and also aid in investigating the effect of Brillouin processes under the presence of axial and shear stress, which are currently neglected in current work.

Appendix A

Python (FEniCS) Code.

A.1 Mesh generation.

```
# mesh_builder.py

from dolfin import *
from mshr import *
import mshr
from numpy import sqrt,cos,sin,double
from mpi4py import MPI

def Fiber_Waveguide_Mesh(r_core,
             r_clad,
             single     = True,
             d_core     = 0.99,
             ratio_core = 0.02,
             ratio_clad = 0.01):
  '''

  This is a function to create a circular mesh with a cladding
   radius of
  r_clad, and one of the two core configurations (toggled by s_or_d)
   :

  1) Single Core of radius r_core. The core is declared as a
   subdomain
  of the cladding to make sure there are enough cells that take care
    of the
  discontinuity at the boundary.

  2) Two cores of radius r_core each, separated by a distance d_core
   .
  Variable y represents the height at which the secondary circles
   are made
  above the dual core for smoothening the interaction region.

  '''
```

```
29
30    if single:
31
32      #Creating Single core
33      core = Circle(Point(0.0, 0.0), r_core, int(r_core*100))
34
35    else:
36      #Generating Dual core region
37      core = Circle(Point(d_core, 0.0), r_core, int(r_core*100)) \
38          + Circle(Point(-d_core, 0.0), r_core, int(r_core*100))
39
40    # Creating cladding region
41    clad = Circle(Point(0.0, 0.0), r_clad, int(r_clad*50))
42    #Labelling the core as a subdomain of cladding
43    clad.set_subdomain(1,core)
44
45    #Generating Mesh
46    mesh = generate_mesh(clad,1)
47    #Generating markers for the core and cladding
48    markers = MeshFunction('size_t', mesh, 2, mesh.domains())
49
50    #~ # Refine Core
51    mesh, markers = Proper_Refine(mesh, markers, 1, ratio_core*r_core)
52    #~ #mesh, markers = Proper_Refine(mesh, markers, 2, ratio_core*
       r_core)
53
54    #~ # Refine Cladding
55    mesh, markers = Proper_Refine(mesh, markers, 0, ratio_clad*r_clad)
56
57    #Returning the refined mesh and markers
58    return mesh, markers
59
60  def Proper_Refine(mesh, markers, index, limit_radius):
61
62    '''
63    This function finds all the cells in subdomain labelled 'index',
       finds the
64    cells within the subdomain with inradius() greater than the
       limiting radius,
65    and keeps refining those cells until the limit is achieved.
66    '''
67    n_unrefined = 2 # Tag to count the number of unrefined cells
68
69    while (n_unrefined > 0): # loop breaks till all cells are refined
70
71      n_unrefined  = 0 # set to zero
72      cell_markers = MeshFunction("bool", mesh, 2, mesh.domains())
73      cell_markers.set_all(False)
74
75      for cell in cells(mesh):
76
77        if (markers[cell] == index) and (cell.inradius() >=
       limit_radius):
78
79          cell_markers[cell] = True
80          n_unrefined += 1 # increment n_unrefined if unrefined cell
       is found
81
```

```
    mesh    = refine(mesh,cell_markers)
    markers = adapt(markers, mesh)

  return mesh, markers


def refine_maxvalue(cf, mesh, expr, threshold):

  W = FunctionSpace(mesh, dolfin.FiniteElement("DG", mesh.ufl_cell()
   , 0))
  u = project(expr.magnitude, W)

  uv = u.vector()
  dofmap = W.dofmap()
  for cell in dolfin.cells(mesh):
    cell_index = cell.index()
    cell_dofs = dofmap.cell_dofs(cell_index)
    val = np.amax(np.abs(uv[cell_dofs]))
    if (val >= threshold):
      cf[cell] = True

  return cf
```

A.2 Solving Maxwell's equations on Mesh Waveguide.

```
#eigen_builder.py

from dolfin import *
from petsc4py import PETSc
from parameters import *
from tensor_funcs import *

def EM_Function_Generator(mesh):

    # Define function space using FEnICS
    nedelec_order = 1
    lagrange_order = 1
    V_N = FiniteElement("Nedelec 1st kind H(curl)", mesh.ufl_cell(),
    nedelec_order)
    V_L = FiniteElement("Lagrange", mesh.ufl_cell(), lagrange_order)
    combined_space = FunctionSpace(mesh,V_N*V_L)

    # Define basis and bilinear form
    (N_i,L_i) = TestFunctions(combined_space)
    (N_j,L_j) = TrialFunctions(combined_space)

    return combined_space, N_i, L_i, N_j, L_j

def curl_t(w):
    return Dx(w[1],0) - Dx(w[0],1)

def eps_ij_EiEj(N_v, N_u, disp, P, e_r):
```

```
    D_DIM = 2
    S = 0
    for i in range(D_DIM):
        for j in range(D_DIM):
            S = S + e_r**2*eps_ij(disp,i,j,P)*N_v[i]*N_u[j]
    return S

def delta(i,j):
    if i == j:
        return 1
    else:
        return 0

def EM_Variational_Matrices(mesh, marker, N_i, L_i, N_j, L_j,
    material, lamb=1.55, disp = 0):

    '''
    Setting up the variational formulation for Maxwell's equation on
    a 2D
    cross-section for an arbitrary waveguide
    '''

    e_r, _,  _,  P,  _ = get_params(marker, material)

    # Define Wavevector for light of lambda = 1.55 microns
    k_o_squared = Constant((2*pi/lamb)**2)

    # Relative permiability of Chalc_PMMA (=1)
    one_over_u_r = Constant(1.0)

    s_tt = one_over_u_r*dot(curl_t(N_i), curl_t(N_j))
    if disp != 0 :
        t_tt = e_r*dot(N_i, N_j) + eps_ij_EiEj(N_i, N_j, disp, P,
    e_r)
    else:
        t_tt = e_r*dot(N_i, N_j)
    s_zz = one_over_u_r*dot(grad(L_i), grad(L_j))
    t_zz = e_r*L_i*L_j

    b_tt = one_over_u_r*dot(N_i, N_j)
    b_tz = one_over_u_r*dot(N_i, grad(L_j))
    b_zt = one_over_u_r*dot(grad(L_i), N_j)
    b_zz = ( s_zz - k_o_squared * t_zz)

    a = ( s_tt - k_o_squared * t_tt )
    b = ( b_tt + b_tz + b_zt + b_zz )

    return a,b, e_r

class Zero_Boundary(SubDomain):
    def inside(self, x, on_boundary):
        return on_boundary

def Eigenvalue_Solver(combined_space, a, b, e_r, n_eigen, dirichlet
    = True):

    '''
    Solving the eigenvalue problem A*u = lambda B using PETSc
```

```
    Save the eigenvector into a .pvd file
    '''

    # Test for PETSc and SLEPc
    if not has_linear_algebra_backend("PETSc"):
        print("DOLFIN has not been configured with PETSc. Exiting.")
        exit()

    if not has_slepc():
        print("DOLFIN has not been configured with SLEPc. Exiting.")
        exit()

    # Assembling the equations as Matrices
    A = PETScMatrix()
    B = PETScMatrix()
    assemble(a, tensor=A)
    assemble(b, tensor=B)

    # Setting up dirichlet Boundary
    if dirichlet:
        zero = Constant( (0.0, 0.0, 0.0) )
        dirichlet_bc = DirichletBC(combined_space, zero,
Zero_Boundary())
        dirichlet_bc.apply(A)
        dirichlet_bc.apply(B)

    # Create eigensolver with generalized Hermitian condition
    # Documentation of Eigensolver : pydoc dolfin.SLEPcEigenSolver
    eigensolver = SLEPcEigenSolver(A,B)
    eigensolver.parameters["spectrum"] = "smallest real"
    #eigensolver.parameters["solver"] = "lanczos"

    # Compute all eigenvalues of A = \lambda B_RHS x
    print("Computing eigenvalues. This can take a minute.")
    eigensolver.solve(4)

    fields = []
    n_eff = []
    for i in range(n_eigen):
        try:
            (lr, lc) = eigensolver.get_eigenvalue(i)
        except RuntimeError:
            print(' Aborting Mission ')
            exit()
        print("Cutoff frequency:", lr, "n_eff:", sqrt(-lr)*1.55/2/pi
)
        ## Extract eigenvector for cutoff frequency
        (_, _, rx, _) = eigensolver.get_eigenpair(i)

        #~ ur = Function(combined_space,rx)

        ## Convert from e_t to E_t by diving each term by 1/sqrt(-lr
)
        ## Also neglecting axial component
        #~ U = ur.vector()
        dofs_is = [combined_space.sub(i).dofmap().dofs() for i in
range(2)]
        rx[dofs_is[0][:]] *= 1/sqrt(-lr)
```

```
        rx[dofs_is[1][:]] *= 1

        ## Initialize function and assign eigenvector
        ur = Function(combined_space, rx)

        ## normalize field to unit Power
        factor = assemble(sqrt(e_r)*(ur[0]**2 + ur[1]**2 + ur[2]**2)*dx)
        ur     = Function(combined_space, rx/sqrt(factor))
        fields.append(ur)
        n_eff.append(sqrt(-lr)*1.55/2/pi)

    return fields, n_eff
```

A.3 Solving Elastodynamics equations.

```
#acoustic_builder.py
from dolfin import *
import numpy as np
from parameters import *


def SBS_Variational_Matrices(mesh, markers, EM, material, n_prop, Omega, path='', lamb=1.55, s = False, disp = 0):
    # Creating the Function Space for the Acoustic Vibrations
    lagrange_order = 1
    V  = VectorElement("Lagrange", mesh.ufl_cell(),lagrange_order, dim=3)
    ME = FunctionSpace(mesh,MixedElement([V,V]))
    v  = TestFunctions(ME)
    u  = TrialFunctions(ME)

    # Defining Parameters
    e_r, rho, C, P, Qf = get_params(markers, material)

    # Permittivity in Free Space
    e_0 = Constant(8.85E-12/1E-6)

    # Momentum vector K for wavelength of 1.55 microns
    K   = Constant(4*n_prop*pi/lamb)

    A     = -rho * v_u(v,u)*dx
    B     = v_c_ijkl_u(v,u,C,0,K)*dx
    C     = v_c_ijkl_u(v,u,0,C,K)/Qf*dx
    L     = e_0 * v_T(v,P,EM,disp,K,e_r)*dx

    N_iter = len(Omega)
    Energy = np.zeros(N_iter)

    # Dirichlet condition
    zero         = Constant( (0.0, 0.0, 0.0, 0.0, 0.0, 0.0) )
    dirichlet_bc = DirichletBC(ME, zero, Zero_Boundary())

    U = Function(ME)

```

```
38      # Solve for each energy E
39      for i in range(N_iter):
40          if i%10 == 0:
41              print(path + '_' + str(100.0*i/N_iter)+'%: '+str(Omega[i
    ])+'GHz')
42          F = Constant(2*pi*Omega[i])
43          M = F**2*A + B + F*C
44          solve(M == L, U, dirichlet_bc)
45
46          Ac = rho*(U[0]**2+U[1]**2+U[2]**2+U[3]**2+U[4]**2+U[5]**2)
47          #~ I  = sqrt(e_r)*(EM[0]**2 + EM[1]**2 + EM[2]**2)
48          #~ U_n_I = assemble(sqrt(Ac)*I*dx)
49          #~ U_norm = assemble(Ac*dx)
50          #~ I_norm = assemble(I**2*dx)
51          #~ OVERLAP = U_n_I**2 / U_norm / I_norm
52
53          E = assemble(F**2*Ac*dx)
54
55          Energy[i] = E#*OVERLAP
56
57          if s:
58              File(path + '/Acoustic/'+str(Omega[i])+'_GHz.xml') << U
59
60      return Energy
61
62  ## Define Zero Boundary class
63  class Zero_Boundary(SubDomain):
64      def inside(self, x, on_boundary):
65          return on_boundary
66
67  # Calculus on tensors :S
68  def tensor_coeff(i,j,k,l,param):
69
70      if param == 0:
71          return 0.0
72
73      if (i==j) and (k==l):
74          if (i==k):
75              return param[0]
76          else:
77              return param[1]
78      elif (i!=j) and (((i==k) and (j==l)) or ((i==l) and (j==k))):
79          return param[2]
80      else:
81          return 0.0
82
83  def c_prod(c_r,c_i,v_r,v_i,u_r,u_i):
84
85      p_r  = v_r*u_r - v_i*u_i
86      p_i  = v_r*u_i + v_i*u_r
87      pr_r = c_r*p_r - c_i*p_i
88      pr_i = c_r*p_i + c_i*p_r
89
90      return pr_r + pr_i
91
92  def Dr(v,K,i,j):
93
94      if j == 2:
```

```
95          return K*v[1][i]
96      else:
97          return Dx(v[0][i],j)
98
99  def Di(v,K,i,j):
100
101     if j == 2:
102         return -K*v[0][i]
103     else:
104         return Dx(v[1][i],j)
105
106 def EE_r(E,i,j):
107
108     return E[i]*E[j]
109
110
111 def v_u(v,u):
112     VEC_DIM = 3
113     S = 0.0
114     for i in range(VEC_DIM):
115         S = S + c_prod(1,0,v[0][i],-v[1][i],u[0][i],u[1][i])
116
117     return S
118
119 def v_c_ijkl_u(v,u,pr,pi,K):
120     VEC_DIM = 3
121     S = 0.0
122     for i in range(VEC_DIM):
123         for j in range(VEC_DIM):
124             for k in range(VEC_DIM):
125                 for l in range(VEC_DIM):
126                     S = S + c_prod(tensor_coeff(i,j,k,l,pr),\
127                                    tensor_coeff(i,j,k,l,pi),\
128                                    Dr(v,K,i,j),-Di(v,K,i,j),\
129                                    Dr(u,K,k,l), Di(u,K,k,l))
130     return S
131
132 def v_T(v,P,E,D,K,e_r):
133     VEC_DIM = 3
134     S = 0.0
135     for i in range(VEC_DIM):
136         for j in range(VEC_DIM):
137             for k in range(VEC_DIM):
138                 for l in range(VEC_DIM):
139                     S = S + e_r**2*c_prod(tensor_coeff(k,l,i,j,P)
    ,0,\
140                                    Dr(v,K,i,j),-Di(v,K,i,j),\
141                                    EE_r(E,k,l),0)
142                     if D != 0:
143                         D_DIM = 2
144                         for m in range(D_DIM):
145                             for n in range(D_DIM):
146                                 S = S + e_r**4*eps_ij(D,i,m,P)*
    eps_ij(D,j,n,P)\
147                                     *c_prod(tensor_coeff(k,l,m,n,P)
    ,0,\
148                                             Dr(v,K,i,j),-Di(v,K,i,j)
    ,\
```

```
                                                EE_r(E,k,l),0)
                        for m in range(D_DIM):
                            S = S + e_r**3*eps_ij(D,i,m,P)\
                                *c_prod(tensor_coeff(k,l,m,j,P),0,\
                                        Dr(v,K,i,j),-Di(v,K,i,j),\
                                        EE_r(E,k,l),0)
                        for n in range(D_DIM):
                            S = S + e_r**3*eps_ij(D,j,n,P)\
                                *c_prod(tensor_coeff(k,l,i,n,P),0,\
                                        Dr(v,K,i,j),-Di(v,K,i,j),\
                                        EE_r(E,k,l),0)
    return S

# Change in Dielectric eps_ij due to strain
def eps_ij(u,i,j,P):
    VEC_DIM = 2
    S = 0.0

    for k in range(VEC_DIM):
        for l in range(VEC_DIM):
            Skl = 0.5*(Dx(u[k],l) + Dx(u[l],k))
            S = S + tensor_coeff(i,j,k,l,P)*Skl
    return -S
```

A.4 Calculating Strain Distribution due to transverse load.

```
#calc_strain.py
from dolfin import *
from mesh_builder import *
from parameters import *
from matplotlib import pyplot as plt

def calc_strain(load, mesh, markers, fiber='chalco'):

    load = load

    N = 2

    # Creating the Function Space for the Strain
    ME = VectorFunctionSpace(mesh, 'Lagrange', 2)
    v  = TestFunctions(ME)
    u  = TrialFunctions(ME)

    # Defining Parameters
    e_r, rho, C, P, Qf = get_params(markers, fiber)
    if fiber=='chalco':
        print(fiber)
        E1 = 70e9 # Pa, glass
        E2 = 6.08e9 # Pa, PMMA
        v1 = 0.22 #[/]
        v2 = 0.327 #[/]
        g  = 10 #m/s^2
```

```
    else:
        print(fiber)
        E1 = 70e9 # Pa, glass
        E2 = 72.55e9 # Pa SMF clad
        v1 = 0.22 #[/]
        v2 = 0.17 # [/]
        g  = 10 #m/s^2

    r = 50e-6 # m
    L = 0.05 # m

    b = (4*load*g*r/pi/L/N * ((1 - v1**2)/E1 + (1 - v2**2)/E2))**0.5

    if b == 0:
        Pressure = 0.0
    else:
        Pressure = (2 * load *g/pi/b/L/N)/1e9

    print(b)
    print(Pressure)

    b = b/1e-6

    class Load1(UserExpression):
        def eval(self, value, x):
            if x[0]**2<b**2 - DOLFIN_EPS and x[1] < 0:
                value[0] = 0.0
                value[1] = Pressure*(1 - x[0]**2/b**2)**0.5
            else:
                value[0] = 0.0
                value[1] = 0.0
        def value_shape(self):
            return (2,)

    class Load2(UserExpression):
        def eval(self, value, x):
            if x[0]**2<b**2 - DOLFIN_EPS and x[1] > 0:
                value[0] = 0.0
                value[1] = -Pressure*(1 - x[0]**2/b**2)**0.5
            else:
                value[0] = 0.0
                value[1] = 0.0
        def value_shape(self):
            return (2,)

    # APPLY LOAD
    T1 = Load1(degree = 2)
    T2 = Load2(degree = 2)

    # LINEAR ELASTICITY
    a = v_j_sig_ji(v,u,C)*dx
    l = (T1[1]*v[1] + T2[1]*v[1])* ds # ds OVER BOUNDARY

    U = Function(ME)

    solve(a == l, U)

    return U
```

```
85
86 # LHS of linear elasticity equation
87 def v_j_sig_ji(v,u,C):
88     VEC_DIM = 2
89     S = 0.0
90     for i in range(VEC_DIM):
91         for j in range(VEC_DIM):
92             for k in range(VEC_DIM):
93                 for l in range(VEC_DIM):
94                     Sij = 0.5*(Dx(v[i],j) + Dx(v[j],i))
95                     Skl = 0.5*(Dx(u[k],l) + Dx(u[l],k))
96                     S = S + Sij*tensor_coeff(i,j,k,l,C)*Skl
97     return S
```

A.5 Assign Core and Cladding Parameters on each Subregion of Mesh.

```
1 #parameters.py
2 # Copyright 2019 Eduard C. Dumitrescu, all rights reserved
3 from dolfin import *
4 import sys
5
6 version = sys.version_info
7
8 if version.major == 3:
9
10     class CellFunctionCases(UserExpression):
11         def __init__(self, user_shape, user_mapping, user_marker_map
    , **kwargs):
12             self.user_shape = user_shape
13             self.user_mapping = user_mapping
14             self.user_marker_map = user_marker_map
15             super().__init__(**kwargs)
16         def eval_cell(self, values, x, ufc_cell):
17             mapping = self.user_mapping
18             k = self.user_marker_map[ufc_cell.index]
19             vals = mapping[k].values()
20             for i in range(len(vals)):
21                 values[i] = vals[i]
22         def value_shape(self):
23             return self.user_shape
24
25     def Create_CellFunctionCases(markers, mapping, **kwargs):
26
27         shape = next(iter(mapping.values())).ufl_shape
28         return CellFunctionCases(
29                 user_shape=shape,
30                 user_mapping=mapping,
31                 user_marker_map=markers,
32                 degree=1, **kwargs)
33
34     def get_param_func(markers, constants):
35         # wrapper around CellFunctionCases
```

```
36          mapping = {k: Constant(v) for k,v in constants.items()}
37          return Create_CellFunctionCases(markers, mapping)
38  else:
39      def Create_CellFunctionCases(markers, mapping, **kwargs):
40          shape = next(iter(mapping.values())).ufl_shape
41          class CellFunctionCases(Expression):
42              '''Given `cell_function` and `mapping`, this object is a
        dolfin Expression
43              which takes the value mapping[cell_function[current_cell
       ]] at every point. It
44              effectively plays the same role as \\cases does in
       mathematics.'''
45              def __init__(self, **kwargs):
46                  self.cell_function = markers
47                  self.mapping = mapping
48                  # we're on purpose not calling superclass __init__.
49                  # dolfin's expression.py says so, because it's doing
        some black magic
50
51              def eval_cell(self, values, x, cell):
52                  mapping = self.mapping
53                  k = self.cell_function[cell.index]
54                  if k not in mapping:
55                      k = None
56                  mapping[k].eval_cell(values, x, cell)
57
58              def value_shape(self):
59                  return shape
60
61          return CellFunctionCases(degree=1,**kwargs)
62
63      def get_param_func(markers, constants):
64          # wrapper around CellFunctionCases
65          mapping = {k: Constant(v) for k,v in constants.items()}
66          return Create_CellFunctionCases(markers, mapping)
67
68  def get_params(markers, material):
69
70      if material == 'silica':
71          Dielectric    = get_param_func(markers, {1: (1.4492**2), 0:
       (1.444**2)})
72          Density       = get_param_func(markers, {1: (2.254), 0:
       (2.203)})
73          Stress_Tensor = get_param_func(markers, {1: (76, 16.15,
       29.9),
74                                                   0: (78, 16, 31)})
75          Photo_Tensor  = get_param_func(markers, {1: (0.20, 0.27,
       -0.073),
76                                                   0: (0.20, 0.27,
       -0.073)})
77          Qf_product    = get_param_func(markers, {1: (2*pi*6e3), 0:
       (2*pi*1e0)})
78
79      if material == 'chalco':
80          Dielectric    = get_param_func(markers, {1: (2.674**2), 0:
       (1.481**2)})
81          Density       = get_param_func(markers, {1: (4.640), 0:
       (1.187)})
```

```
82          Stress_Tensor = get_param_func(markers, {1: (23.5, 9.5,
    6.99),
83                                                   0: (6.63, 4.34,
    1.145)})
84          Photo_Tensor  = get_param_func(markers, {1: (0.314, 0.266,
    0.024),
85                                                   0: (0.30, 0.297,
    0.0015)})
86          Qf_product    = get_param_func(markers, {1: (2*pi*2e3), 0:
    (2*pi*7e1)})
87
88      return Dielectric, Density, Stress_Tensor, Photo_Tensor,
    Qf_product
```

Publications

1. B. Saxena, C. Baker, X. Bao and L. Chen, "Simultaneous generation of guided-acoustic-wave Brillouin scattering and stimulated-Brillouin-scattering in hybrid As2Se3-PMMA microtapers", *Opt. Express*, vol 27(10), pp. 13734-13743, May 2019.

2. B. Saxena, C. Baker, X. Bao and L. Chen, "High birefringent Brillouin frequency shifts in single mode As2Se3-PMMA microtaper induced by transverse load", *Opt. Lett.*, vol 44(19), pp. 4789-4792, Oct 2019.

3. L. Zhang, Y. Xu, S. Gao, B. Saxena, L. Chen, and X. Bao, Multiwavelength Coherent Brillouin Random Fiber Laser With Ultrahigh Optical Signal-to-Noise Ratio, *IEEE Journal of Selected Topics in Quantum Electronics*, vol. 24(3), pp. 18, May 2018.

4. L. Zhang, C. Wang, Z. Li, Y. Xu, B. Saxena, S. Gao, L. Chen, and X. Bao, High-efficiency Brillouin random fiber laser using all-polarization maintaining ring cavity, *Opt. Express*, vol. 25, no. 10, p. 11306, May 2017.

5. L. Zhang, Y. Xu, S. Gao, B. Saxena, L. Chen, and X. Bao, Linearly polarized low-noise Brillouin random fiber laser, *Opt. Lett.*, vol. 42(4), pp. 739742, Feb. 2017.

Chapter 9

References

[1] G. Agrawal, *Nonlinear Fiber Optics (Fifth Edition)*. Optics and Photonics, Boston: Academic Press, 5th ed., 2013.

[2] R. Boyd, *Nonlinear Optics*. Nonlinear Optics Series, Elsevier Science, Amsterdam, 2008.

[3] J.-C. Beugnot and V. Laude, "Electrostriction and guidance of acoustic phonons in optical fibers," *Physical Review B*, vol. 86, Dec. 2012.

[4] P. T. Rakich, P. Davids, and Z. Wang, "Tailoring optical forces in waveguides through radiation pressure and electrostrictive forces," *Optics Express*, vol. 18, p. 14439, July 2010.

[5] A. Ruffin, "Stimulated Brillouin scattering: an overview of measurements, system impairments, and applications," in *Technical Digest: Symposium on Optical Fiber Measurements, 2004*, (Boulder, CO, USA), pp. 23–28, IEEE, 2004.

[6] A. Kobyakov, M. Sauer, and D. Chowdhury, "Stimulated Brillouin scattering in optical fibers," *Advances in Optics and Photonics*, vol. 2, p. 1, Mar. 2010.

[7] X. Bao, J. Dhliwayo, N. Heron, D. J. Webb, and D. A. Jackson, "Experimental and theoretical studies on a distributed temperature sensor based on Brillouin scattering," *Journal of Lightwave Technology*, vol. 13, pp. 1340–1348, July 1995.

[8] X. Bao and L. Chen, "Recent progress in distributed fiber optic sensors," *Sensors*, vol. 12, no. 7, pp. 8601–8639, 2012.

[9] X. Bao and L. Chen, "Recent progress in Brillouin scattering based fiber sensors," *Sensors*, vol. 11, no. 4, pp. 4152–4187, 2011.

[10] X. Yao, "Phase-to-amplitude modulation conversion using Brillouin selective sideband amplification," *IEEE Photonics Technology Letters*, vol. 10, pp. 264–266, Feb. 1998.

[11] J. Lee, D. Sun, and Z. J. Cendes, "Full-wave analysis of dielectric waveguides using tangential vector finite elements," *IEEE Transactions on Microwave Theory and Techniques*, vol. 39, pp. 1262–1271, Aug 1991.

[12] W. Loh, S. Yegnanarayanan, F. ODonnell, and P. W. Juodawlkis, "Ultra-narrow linewidth Brillouin laser with nanokelvin temperature self-referencing," *Optica*, vol. 6, p. 152, Feb. 2019.

[13] R. M. Shelby, M. D. Levenson, and P. W. Bayer, "Guided acoustic-wave Brillouin scattering," *Phys. Rev. B*, vol. 31, pp. 5244–5252, Apr 1985.

[14] A. J. Poustie, "Bandwidth and mode intensities of guided acoustic-wave Brillouin scattering in optical fibers," *J. Opt. Soc. Am. B*, vol. 10, pp. 691–696, Apr 1993.

[15] N. Hayashi, Y. Mizuno, K. Nakamura, S. Y. Set, and S. Yamashita, "Experimental study on depolarized GAWBS spectrum for optomechanical sensing of liquids outside standard fibers," *Opt. Express*, vol. 25, pp. 2239–2244, Feb 2017.

[16] R. Thurston, "Elastic waves in rods and optical fibers," *Journal of Sound and Vibration*, vol. 159, no. 3, pp. 441 – 467, 1992.

[17] H. E. Engan, B. Y. Kim, J. N. Blake, and H. J. Shaw, "Propagation and optical interaction of guided acoustic waves in two-mode optical fibers," *Journal of Lightwave Technology*, vol. 6, pp. 428–436, March 1988.

[18] B. A. Auld, *Acoustic fields and waves in solids*. Malabar, Fla: R.E. Krieger, 2nd ed., 1990.

[19] N. Hayashi, Y. Mizuno, K. Nakamura, S. Y. Set, and S. Yamashita, "Characterization of depolarized GAWBS for optomechanical sensing of liquids outside standard fibers," in *25th International Conference on Optical Fiber Sensors*, vol. 10323, p. 103230M, International Society for Optics and Photonics, Apr. 2017.

[20] Y. Tanaka and K. Ogusu, "Tensile-strain coefficient of resonance frequency of depolarized guided acoustic-wave Brillouin scattering," *IEEE Photonics Technology Letters*, vol. 11, pp. 865–867, July 1999.

[21] Y. Antman, A. Clain, Y. London, and A. Zadok, "Optomechanical sensing of liquids outside standard fibers using forward stimulated Brillouin scattering," *Optica*, vol. 3, pp. 510–516, May 2016.

[22] P. F. Jarschel, L. S. Magalhaes, I. Aldaya, O. Florez, and P. Dainese, "Fiber taper diameter characterization using forward Brillouin scattering," *Opt. Lett.*, vol. 43, pp. 995–998, Mar 2018.

[23] G. Bashan, H. H. Diamandi, Y. London, E. Preter, and A. Zadok, "Optomechanical time-domain reflectometry," *Nature Communications*, vol. 9, Dec. 2018.

[24] J.-C. Beugnot, T. Sylvestre, H. Maillotte, G. Mélin, and V. Laude, "Guided acoustic wave Brillouin scattering in photonic crystal fibers," *Opt. Lett.*, vol. 32, pp. 17–19, Jan 2007.

[25] A. Zarifi, B. Stiller, M. Merklein, and B. Eggleton, "High resolution Brillouin sensing of sicro-scale structures," *Applied Sciences*, vol. 8, p. 2572, Dec. 2018.

[26] S. Dai, Y. Wang, X. Peng, P. Zhang, X. Wang, and Y. Xu, "A review of mid-infrared supercontinuum generation in chalcogenide glass fibers," *Applied Sciences*, vol. 8, p. 707, May 2018.

[27] J.-C. Beugnot, R. Ahmad, M. Rochette, V. Laude, H. Maillotte, and T. Sylvestre, "Reduction and control of stimulated Brillouin scattering in polymer-coated chalcogenide optical microwires," *Opt. Lett.*, vol. 39, pp. 482–485, Feb 2014.

[28] J.-C. Beugnot, R. Ahmad, M. Rochette, V. Laude, H. Maillotte, and T. Sylvestre, "Tunable stimulated Brillouin scattering in hybrid polymer-chalcogenide tapered fibers," *Proc. SPIE*, vol. 9136, p. 91360O, 2014.

[29] C. Baker and M. Rochette, "A generalized heat-brush approach for precise control of the waist profile in fiber tapers," *Opt. Mater. Express*, vol. 1, pp. 1065–1076, Oct 2011.

[30] C. Baker and M. Rochette, "Highly nonlinear hybrid As_2Se_3-PMMA microtapers," *Opt. Express*, vol. 18, pp. 12391–12398, Jun 2010.

[31] D.-I. Yeom, E. C. Mägi, M. R. E. Lamont, M. A. F. Roelens, L. Fu, and B. J. Eggleton, "Low-threshold supercontinuum generation in highly nonlinear chalcogenide nanowires," *Opt. Lett.*, vol. 33, pp. 660–662, Apr 2008.

[32] A. Al-kadry, C. Baker, M. El Amraoui, Y. Messaddeq, and M. Rochette, "Broadband supercontinuum generation in as_2se_3 chalcogenide wires by avoiding the two-photon absorption effects," *Optics Letters*, vol. 38, p. 1185, Apr 2013.

[33] J. S. Sanghera, L. Brandon Shaw, and I. D. Aggarwal, "Chalcogenide glass-fiber-based mid-ir sources and applications," *IEEE Journal of Selected Topics in Quantum Electronics*, vol. 15, pp. 114–119, Jan 2009.

[34] M. Asobe, T. Kanamori, and K. Kubodera, "Applications of highly nonlinear chalcogenide glass fibers in ultrafast all-optical switches," *IEEE Journal of Quantum Electronics*, vol. 29, pp. 2325–2333, Aug 1993.

[35] L. B. Fu, M. Rochette, V. G. Ta'eed, D. J. Moss, and B. J. Eggleton, "Investigation of self-phase modulation based optical regeneration in single mode As_2Se_3 chalcogenide glass fiber," *Opt. Express*, vol. 13, pp. 7637–7644, Sep 2005.

[36] F. Smektala, C. Quemard, L. Leneindre, J. Lucas, A. Barthlmy, and C. De Angelis, "Chalcogenide glasses with large non-linear refractive indices," *Journal of Non-Crystalline Solids*, vol. 239, pp. 139–142, Oct 1998.

[37] F. Smektala, C. Quemard, V. Couderc, and A. Barthlmy, "Non-linear optical properties of chalcogenide glasses measured by Z-scan," *Journal of Non-Crystalline Solids*, vol. 274, pp. 232–237, Sept. 2000.

[38] R. E. Slusher, G. Lenz, J. Hodelin, J. Sanghera, L. B. Shaw, and I. D. Aggarwal, "Large raman gain and nonlinear phase shifts in high-purity As_2Se_3 chalcogenide fibers," *J. Opt. Soc. Am. B*, vol. 21, pp. 1146–1155, Jun 2004.

[39] K. S. Abedin, "Observation of strong stimulated Brillouin scattering in single-mode As_2Se_3 chalcogenide fiber," *Opt. Express*, vol. 13, pp. 10266–10271, Dec 2005.

[40] K. Y. Song, K. S. Abedin, K. Hotate, M. G. Herráez, and L. Thévenaz, "Highly efficient Brillouin slow and fast light using As_2Se_3 chalcogenide fiber," *Opt. Express*, vol. 14, pp. 5860–5865, Jun 2006.

[41] G. Lenz, J. Zimmermann, T. Katsufuji, M. E. Lines, H. Y. Hwang, S. Spälter, R. E. Slusher, S.-W. Cheong, J. S. Sanghera, and I. D. Aggarwal, "Large Kerr effect in bulk se-based chalcogenide glasses," *Opt. Lett.*, vol. 25, pp. 254–256, Feb 2000.

[42] R. Mossadegh, J. S. Sanghera, D. Schaafsma, B. J. Cole, V. Q. Nguyen, R. E. Miklos, and I. D. Aggarwal, "Fabrication of single-mode chalcogenide optical fiber," *Journal of Lightwave Technology*, vol. 16, pp. 214–217, Feb 1998.

[43] M. Ezrin, *Plastics failure guide: causes and prevention*. Munich: Hanser, 1996.

[44] Z. H. Stachurski, "Strength and deformation of rigid polymers: the stressstrain curve in amorphous PMMA," *Polymer*, vol. 44, pp. 6067–6076, Sept. 2003.

[45] G. Beadie, M. Brindza, R. A. Flynn, A. Rosenberg, and J. S. Shirk, "Refractive index measurements of poly(methyl methacrylate) (pmma) from 0.4-1.6 μm," *Appl. Opt.*, vol. 54, pp. F139–F143, Nov 2015.

[46] E. C. Mägi, L. B. Fu, H. C. Nguyen, M. R. E. Lamont, D. I. Yeom, and B. J. Eggleton, "Enhanced Kerr nonlinearity in sub-wavelength diameter As_2Se_3 chalcogenide fiber tapers," *Opt. Express*, vol. 15, pp. 10324–10329, Aug 2007.

[47] Y. Sun, S. Dai, P. Zhang, X. Wang, Y. Xu, Z. Liu, F. Chen, Y. Wu, Y. Zhang, R. Wang, and G. Tao, "Fabrication and characterization of multimaterial chalcogenide glass fiber tapers with high numerical apertures," *Opt. Express*, vol. 23, pp. 23472–23483, Sep 2015.

[48] L. Tong, R. R. Gattass, J. B. Ashcom, S. He, J. Lou, M. Shen, I. Maxwell, and E. Mazur, "Subwavelength-diameter silica wires for low-loss optical wave guiding," *Nature*, vol. 426, p. 816819, Dec 2003.

[49] H.-J. Xu, X. Wang, Q.-H. Nie, M.-M. Zhu, C. Jiang, F.-X. Liao, P.-Q. Zhang, S.-X. Dai, T.-F. Xu, and G. Tao, "Fabrication and properties of chalcogenide optical fiber based on a novel extrusion method," *Guangdianzi Jiguang/Journal of Optoelectronics Laser*, vol. 25, pp. 1109–1114, 06 2014.

[50] R. Ahmad and M. Rochette, "Chalcogenide optical parametric oscillator," *Opt. Express*, vol. 20, pp. 10095–10099, Apr 2012.

[51] R. Ahmad and M. Rochette, "Raman lasing in a chalcogenide microwire-based Fabry-Perot cavity," *Opt. Lett.*, vol. 37, pp. 4549–4551, Nov 2012.

[52] R. Ahmad and M. Rochette, "High efficiency and ultra broadband optical parametric four-wave mixing in chalcogenide-pmma hybrid microwires," *Opt. Express*, vol. 20, pp. 9572–9580, Apr 2012.

[53] R. Ahmad and M. Rochette, "Photosensitivity at 1550 nm and Bragg grating inscription in As_2Se_3 chalcogenide microwires," *Applied Physics Letters*, vol. 99, no. 6, p. 061109, 2011.

[54] A. Al-Kadry, M. E. Amraoui, Y. Messaddeq, and M. Rochette, "Mode-locked fiber laser based on chalcogenide microwires," *Opt. Lett.*, vol. 40, pp. 4309–4312, Sep 2015.

[55] T. Godin, Y. Combes, R. Ahmad, M. Rochette, T. Sylvestre, and J. M. Dudley, "Far-detuned mid-infrared frequency conversion via normal dispersion modulation instability in chalcogenide microwires," *Opt. Lett.*, vol. 39, pp. 1885–1888, Apr 2014.

[56] M. Liao, C. Chaudhari, G. Qin, X. Yan, C. Kito, T. Suzuki, Y. Ohishi, M. Matsumoto, and T. Misumi, "Fabrication and characterization of a chalcogenide-tellurite composite microstructure fiber with high nonlinearity," *Opt. Express*, vol. 17, pp. 21608–21614, Nov 2009.

[57] N. Granzow, S. P. Stark, M. A. Schmidt, A. S. Tverjanovich, L. Wondraczek, and P. S. Russell, "Supercontinuum generation in chalcogenide-silica step-index fibers," *Opt. Express*, vol. 19, pp. 21003–21010, Oct 2011.

[58] N. G. R. Broderick, T. M. Monro, P. J. Bennett, and D. J. Richardson, "Nonlinearity in holey optical fibers: measurement and future opportunities," *Opt. Lett.*, vol. 24, pp. 1395–1397, Oct 1999.

[59] J. Broeng, D. Mogilevstev, S. E. Barkou, and A. Bjarklev, "Photonic crystal fibers: A new class of optical waveguides," *Optical Fiber Technology*, vol. 5, no. 3, pp. 305 – 330, 1999.

[60] W. D. Drotning and E. P. Roth, "Effects of moisture on the thermal expansion of poly(methylmethacrylate)," *Journal of Materials Science*, vol. 24, pp. 3137–3140, Sep 1989.

[61] G. Ozen, B. Demirata, M. Ovecoglu, and A. Genc, "Thermal and optical properties of tm^{3+} doped tellurite glasses," *Spectrochimica Acta Part A: Molecular and Biomolecular Spectroscopy*, vol. 57, no. 2, pp. 273 – 280, 2001.

[62] F. DAmore, M. Lanata, S. Pietralunga, M. C. Gallazzi, and G. Zerbi, "Enhancement of pmma nonlinear optical properties by means of a quinoid molecule," *Optical Materials*, vol. 24, pp. 661–665, 01 2004.

[63] V. Finazzi, T. M. Monro, and D. J. Richardson, "Small-core silica holey fibers: nonlinearity and confinement loss trade-offs," *J. Opt. Soc. Am. B*, vol. 20, pp. 1427–1436, Jul 2003.

[64] D. Mogilevtsev, T. A. Birks, and P. S. J. Russell, "Group-velocity dispersion in photonic crystal fibers," *Opt. Lett.*, vol. 23, pp. 1662–1664, Nov 1998.

[65] K. Ogusu, H. Li, and M. Kitao, "Brillouin-gain coefficients of chalcogenide glasses," *J. Opt. Soc. Am. B*, vol. 21, pp. 1302–1304, Jul 2004.

[66] K. S. Abedin, "Brillouin amplification and lasing in a single-mode As_2Se_3 chalcogenide fiber," *Opt. Lett.*, vol. 31, pp. 1615–1617, Jun 2006.

[67] K. S. Abedin, "Single-frequency Brillouin lasing using single-mode As_2Se_3 chalcogenide fiber," *Opt. Express*, vol. 14, pp. 4037–4042, May 2006.

[68] K. Hu, I. V. Kabakova, T. F. S. Büttner, S. Lefrancois, D. D. Hudson, S. He, and B. J. Eggleton, "Low-threshold Brillouin laser at 2 μm based on suspended-core chalcogenide fiber," *Opt. Lett.*, vol. 39, pp. 4651–4654, Aug 2014.

[69] K. H. Tow, Y. Leguillon, S. Fresnel, P. Besnard, L. Brilland, D. Mechin, P. Toupin, and J. Troles, "Toward more coherent sources using a microstructured chalcogenide Brillouin fiber laser," *IEEE Photonics Technology Letters*, vol. 25, pp. 238–241, Feb 2013.

[70] I. V. Kabakova, R. Pant, D.-Y. Choi, S. Debbarma, B. Luther-Davies, S. J. Madden, and B. J. Eggleton, "Narrow linewidth Brillouin laser based on chalcogenide photonic chip," *Opt. Lett.*, vol. 38, pp. 3208–3211, Sep 2013.

[71] B. Morrison, D. Marpaung, R. Pant, E. Li, D.-Y. Choi, S. Madden, B. Luther-Davies, and B. J. Eggleton, "Tunable microwave photonic notch filter using on-

chip stimulated Brillouin scattering," *Optics Communications*, vol. 313, pp. 85 – 89, 2014.

[72] R. Pant, A. Byrnes, C. G. Poulton, E. Li, D.-Y. Choi, S. Madden, B. Luther-Davies, and B. J. Eggleton, "Photonic-chip-based tunable slow and fast light via stimulated Brillouin scattering," *Opt. Lett.*, vol. 37, pp. 969–971, Mar 2012.

[73] Y. Mizuno and K. Nakamura, "Experimental study of Brillouin scattering in perfluorinated polymer optical fiber at telecommunication wavelength," *Applied Physics Letters*, vol. 97, no. 2, p. 021103, 2010.

[74] V. Laude and J.-C. Beugnot, "Generation of phonons from electrostriction in small-core optical waveguides," *AIP Advances*, vol. 3, no. 4, p. 042109, 2013.

[75] Y. Dong, L. Teng, P. Tong, T. Jiang, H. Zhang, T. Zhu, L. Chen, X. Bao, and Z. Lu, "High-sensitivity distributed transverse load sensor with an elliptical-core fiber based on Brillouin dynamic gratings," *Optics Letters*, vol. 40, pp. 5003–5006, Nov. 2015.

[76] C. M. Lawrence, D. V. Nelson, E. Udd, and T. Bennett, "A fiber optic sensor for transverse strain measurement," *Experimental Mechanics*, vol. 39, pp. 202–209, Sept. 1999.

[77] R. B. Wagreich, W. A. Atia, H. Singh, and J. S. Sirkis, "Effects of diametric load on fibre Bragg gratings fabricated in low birefringent fibre," *Electronics Letters*, vol. 32, pp. 1223–1224, June 1996.

[78] L.-Y. Shao, Q. Jiang, and J. Albert, "Fiber optic pressure sensing with conforming elastomers," *Appl. Opt.*, vol. 49, pp. 6784–6788, Dec 2010.

[79] J. T. Kringlebotn, W. H. Loh, and R. I. Laming, "Polarimetric er^{3+}-doped fiber distributed-feedback laser sensor for differential pressure and force measurements," *Opt. Lett.*, vol. 21, pp. 1869–1871, Nov 1996.

[80] E. Chehura, C.-C. Ye, S. E. Staines, S. W. James, and R. P. Tatam, "Characterization of the response of fibre Bragg gratings fabricated in stress and geometrically induced high birefringence fibres to temperature and transverse load," *Smart Materials and Structures*, vol. 13, pp. 888–895, jun 2004.

[81] C. Jewart, K. P. Chen, B. McMillen, M. M. Bails, S. P. Levitan, J. Canning, and I. V. Avdeev, "Sensitivity enhancement of fiber Bragg gratings to transverse stress by using microstructural fibers," *Optics Letters*, vol. 31, p. 2260, Aug. 2006.

[82] M. Silva-Lpez, W. N. MacPherson, C. Li, A. J. Moore, J. S. Barton, J. D. C. Jones, D. Zhao, L. Zhang, and I. Bennion, "Transverse load and orientation measurement with multicore fiber Bragg gratings," *Applied Optics*, vol. 44, p. 6890, Nov. 2005.

[83] P. Zu, C. C. Chan, W. S. Lew, Y. Jin, Y. Zhang, H. F. Liew, L. H. Chen, W. C. Wong, and X. Dong, "Magneto-optical fiber sensor based on magnetic fluid," *Opt. Lett.*, vol. 37, pp. 398–400, Feb 2012.

[84] C. Fan, C. Chiang, and C. Yu, "Birefringent photonic crystal fiber coils and their application to transverse displacement sensing," *Opt. Express*, vol. 19, pp. 19948–19954, Oct 2011.

[85] Y. Yang, H. Li, L. Lu, F. Yang, and W. Jin, "Radiation-induced birefringence variations in polarization-maintaining fibers," *Opt. Lett.*, vol. 42, pp. 5214–5217, Dec 2017.

[86] R. R. J. Maier, W. N. MacPherson, J. S. Barton, S. McCulloch, and B. J. S. Jones, "Distributed sensing using Rayleigh scatter in polarization-maintaining fibres for transverse load sensing," *Measurement Science and Technology*, vol. 21, p. 094019, July 2010.

[87] S. Xie, M. Pang, X. Bao, and L. Chen, "Polarization dependence of Brillouin linewidth and peak frequency due to fiber inhomogeneity in single mode fiber

and its impact on distributed fiber brillouin sensing," *Optics Express*, vol. 20, p. 6385, Mar. 2012.

[88] W. Zou, Z. He, and K. Hotate, "Complete discrimination of strain and temperature using Brillouin frequency shift and birefringence in a polarization-maintaining fiber," *Opt. Express*, vol. 17, pp. 1248–1255, Feb 2009.

[89] M. LeBlanc, S. T. Vohra, T. E. Tsai, and E. J. Friebele, "Transverse load sensing by use of pi-phase-shifted fiber Bragg gratings," *Optics Letters*, vol. 24, p. 1091, Aug. 1999.

[90] K. Y. Song, S. Chin, N. Primerov, and L. Thévenaz, "Time-domain distributed fiber sensor with 1 cm spatial resolution based on Brillouin dynamic grating," *J. Lightwave Technol.*, vol. 28, pp. 2062–2067, Jul 2010.

[91] Y. Dong, X. Bao, and L. Chen, "Distributed temperature sensing based on birefringence effect on transient Brillouin grating in a polarization-maintaining photonic crystal fiber," *Opt. Lett.*, vol. 34, pp. 2590–2592, Sep 2009.

[92] N. Mothe and P. D. Bin, "Numerical analysis of directional coupling in dual-core microstructured optical fibers," *Opt. Express*, vol. 17, pp. 15778–15789, Aug 2009.

[93] *Novel optical fibers for distributed sensor applications*, vol. 10323, April 2017.

[94] M. Zaghloul, M. Wang, G. Milione, M.-J. Li, S. Li, Y.-K. Huang, T. Wang, and K. P. Chen, "Discrimination of temperature and strain in Brillouin optical time domain analysis using a multicore optical fiber," *Sensors*, vol. 18, p. 1176, 04 2018.

[95] S. Gao, C. Baker, L. Chen, and X. Bao, "Approach for temperature-sensitivity enhancement in a tapered dual-core As_2Se_3-pmma fiber with an antisymmetric long-period grating," *J. Lightwave Technol.*, vol. 37, pp. 2734–2738, Jun 2019.

[96] S. Gao, C. Baker, L. Chen, and X. Bao, "High-sensitivity temperature and strain measurement in dual-core hybrid tapers," *IEEE Photonics Technology Letters*, vol. 30, pp. 1155–1158, June 2018.

[97] S. Gao, C. Baker, L. Chen, and X. Bao, "Simultaneous measurement of temperature and strain in a dual-core As_2Se_3-pmma taper," *IEEE Photonics Technology Letters*, vol. 30, pp. 79–82, Jan 2018.

[98] C. Baker, *Hybrid As_2S_3-PMMA microtapers and applications.* Ph. D., McGill University, 2013.

[99] F. Gonthier, S. Lacroix, and J. Bures, "Numerical calculations of modes of optical waveguides with two-dimensional refractive index profiles by a field correction method," *Optical and Quantum Electronics*, vol. 26, pp. S135–S149, Mar 1994.

[100] N. Kishi and T. Okoshi, "Proposal for a boundary-integral method without using green's function," *IEEE Transactions on Microwave Theory and Techniques*, vol. 35, pp. 887–892, Oct 1987.

[101] T. Angkaew, M. Matsuhara, and N. Kumagai, "Finite-element analysis of waveguide modes: A novel approach that eliminates spurious modes," *IEEE Transactions on Microwave Theory and Techniques*, vol. 35, pp. 117–123, Feb 1987.

[102] J. Lee, D. Sun, and Z. J. Cendes, "Full-wave analysis of dielectric waveguides using tangential vector finite elements," *IEEE Transactions on Microwave Theory and Techniques*, vol. 39, pp. 1262–1271, Aug 1991.

[103] J. Jin, *The Finite Element Method in Electromagnetics.* Wiley-IEEE, New York, 3rd ed., 2014.

[104] M. Alnaes, J. Blechta, J. Hake, A. Johansson, B. Kehlet, A. Logg, C. Richardson, J. Ring, M. Rognes, and G. Wells, "The FEniCS Project Version 1.5," *Archive of Numerical Software*, vol. 3, no. 100, 2015.

[105] W. M. Isbell, D. R. Christman, S. G. Babcock, T. E. Michaels, and S. J. Green, "Measurements of Dynamic Properties of Materials. Volume 1. Summary of Results," Tech. Rep. MSL-70-23-Vol-1, General Motors Technical Center, Warren Mich Materials Structures Lab, July 1970.

[106] J.-C. Beugnot and V. Laude, "Electrostriction and guidance of acoustic phonons in optical fibers," *Phys. Rev. B*, vol. 86, pp. 224304–224310, Dec 2012.

[107] A. Tuniz, G. Brawley, D. J. Moss, and B. J. Eggleton, "Two-photon absorption effects on Raman gain in single mode As_2Se_3 chalcogenide glass fiber," *Opt. Express*, vol. 16, pp. 18524–18534, Oct 2008.

[108] A. Logg, K.-A. Mardal, and G. Wells, eds., *Automated Solution of Differential Equations by the Finite Element Method: The FEniCS Book*. No. 84 in Lecture Notes in Computational Science and Engineering, Springer, Berlin, 2012.